STRUCTURAL STUDIES OF BORO-SILICATE AND PHOSPHATE GLASSES BY X-RAY AND NEUTRON DIFFRACTION

A THESIS SUBMITTED FOR THE AWARD OF THE DEGREE OF

DOCTOR OF PHILOSOPHY

IN THE FACULTY OF NATURAL SCIENCES

OF GOA UNIVERSITY

By

Alka P.G. Shikerkar

Department of Physics

Goa University

Goa

January 1999

Certified that this thesis is as accepted and passed by the Viva-Voce board of examiners

S.K. Mendiratta 27.9.1999
[S.K. Mendiratta]
External Examiner

Erwin Desa 27.9.1999
[J.A.E. Desa]
Coordinator, Guide

To

My Parents

DECLARATION

I declare that this thesis represents work which has been carried out by me and that it has not been submitted to any other University or Institution for the award of any Degree, Diploma, Associateship, Fellowship or any other such title.

Place: Taleigão Plateau,

Panaji, Goa

Ms. Alka P.G. Shikerkar

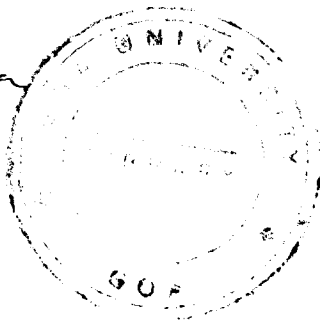Date : 21st January, 1999

CERTIFICATE

I hereby certify that the above Declaration of the candidate Alka P. G. Shikerkar is true and that this thesis represents her independent work.

Dr. J.A.E. Desa

(Research Guide)

Reader

Department of Physics,

Goa University, Goa

Measurements in the UV and visible range from 200 Å to 1000 Å found the lanthanum, cerium, europium and terbium-containing glasses to be excellent UV absorbers with no absorption in the visible range. Others had sharp absorption bands in the visible region together with strong absorption the UV region, indicating good potential for applications as filters and optical fibres.

Magnetic susceptibility measurements on these glasses in the range 82 K to 300 K showed that there is a decrease in the value of χ with an increase in temperature.

ACKNOWLEDGEMENTS

to my husband's family and my siblings. I am pleased to express my special gratitude to my husband Sunil for his generous support, encouraging words and patience.

Finally, I express my sincere thanks to all those persons who have helped me in whatever form, in the course of this work and who I may have inadvertently forgotten to mention in this acknowledgement.

January 1999   Alka Shikerkar

Contents

List of Figures

List of Tables

List of symbols

A_{jk} Peak area constant for k type atoms around j type

$A_i(Q)$ Absorption factor for neutrons which have undergone i scattering events

A_w Molecular weight per composition unit

$\overline{b_j}$ Isotopically averaged coherent neutron scattering length for atom type j

c.u.   Chemical composition unit

C_R Ratio in composition units of sample to vanadium

$d_{jk}(\mathrm{r})$ Component differential correlation function involving atom types j and k

$D(r)$ Total differential correlation function

$e(Q)$ Multiplicative error in the interference function

$E(Q)$ Additive error in the interference function

E_0 Incident neutron energy

E Final neutron energy

$f(Q)$ X-ray atomic form factor function

$f_e(Q)$ X-ray average atomic form factor per electron

$g(r)$ Radial Distribution function abbreviated to RDF

$G(r,t)$ Van Hove space-time correlation function

$i(Q)$ Distinct scattered intensity as defined by $\mathrm{I(Q)}\text{-}I^s(Q) - I^0(Q)$

$i_{jk}(Q)$ Distinct scattered intensity for atom types j and k

$I(Q)$ Normalized total scattered intensity

$I^0(Q)$	Contribition of I(Q) from components of average density
k_B	Boltzmann constant
$\underline{k_0}$	incident wave vector
$\underline{k}$	Outgoing wave vector
m_n	Mass of neutron ($= 1.0086654$ amu)
$M(Q)$	Lorch modification function
$n_j(k)$	Coordination number of k type atoms about j type
$P_{jk}(r)$	Peak shape function
$\underline{Q_0}$	Momentum transfer vector for elastic scattering
r	Distance parameter
r_{jk}	Distance between j and k atoms
ρ	Density
ρ_0	Number density
$S(Q,\omega)$	Scattering law
T	Temperature in Kelvin
$T^0(r)$	Component of D(r) due to average density
$T(r)$	Total correlation function [D(r) + $T^0(r)$]
Z	Atomic number
α	Renormalization constant for measured scattered intensities
β	Renormalization constant for measured scattered intensities
$\epsilon(k)$	Detector efficiency for neutrons with magnitude of momentum vector $\underline{k}$
2θ	Scattering angle
θ_M	Take-off angle at monochromator of High-Q neutron diffractometer

λ	Incident wavelength
σ^a	Absorption cross-section
σ^s	Scattering cross-section
σ^S	Neutron self-scattering cross-section
σ^D	Neutron distinct scattering cross-section
σ^T	Neutron total cross-section $(= \sigma^a + \sigma^s)$
XRD	X-ray Diffraction
ND	Neutron Diffraction
UV	Ultra-Violet
IR	Infra-red
χ	Susceptibility
EXAFS	Extended X-ray Absorption Fine Structure
ESCA	Electron Spectroscopy for Chemical Analysis
NBO	Non Bridging Oxygen
TO	Terminal Oxygen

Chapter 1

INTRODUCTION

1.1   Preliminary Remarks

Inorganic glasses have been of interest for many hundreds of years due to their special mechanical and optical properties. Ancient man fashioned obsidian, a naturally occurring glassy silicate, into arrow and spear heads for hunting and other uses. Later, when glasses were made, their compositions were varied from time to time in search of new types of glasses which could be used for ornamental purposes. These investigations led to a systematic study of the relation of the composition, strength, glass forming ability and chemical durability. In the last two centuries extensive research has been made into the development of new glassy systems to meet the changing requirements of the present age. This has resulted in glasses with improved chemical durability, strength and other physical properties. In the present century, rapid industrialization and advanced technology have opened new frontiers for glasses applied to Electronics and Medicine. In such uses, glass often does not have the properties ascribed to it by the layman for whom it is a transparent material made from silica and used for windows, lenses, prisms and optical instruments. In reality, glasses can be formed from many different inorganic and organic materials under a host of different conditions. It is thus useful to define the term *glass.*

1.2 Glass structure and formation

Any solid chemical substance may broadly be categorized as either *crystalline* or *amorphous*. Glass is a subset of the amorphous category. In the conventional method of glass preparation, the melt is quenched rapidly enough so that it bypasses the crystallization temperature and enter the supercooled liquid phase. Figure 1.1 [Jones (1956)] shows the variation of specific volume with temperature of a glass. Continuous cooling below the supercooled phase leads to formation of a glass whose volume depends on the speed of cooling. Thus in Fig. 1.1, glass A results from a faster rate of cooling than glass B.

The growing demand for glassy materials for various applications had led to an interest in the relationship between physical properties such as ionic conductivity, hardness, chemical durability, glass transition temperature and the atomic scale structure of glasses. Since these properties ultimately depend on the structure, a knowledge of the latter is useful in optimizing any particular property. Thus, the optical and diffraction spectra of rare-earth doped glasses, for example, depend on the type of host matrix and the immediate environment of the rare-earth ion. This is also true of the nuclear-waste glasses studied here viz. several heavy metal oxides in a boro-silicate host network.

1.3 Structural theories

Various theories were established to understand the process of glass formation related to kinetics and structure. Structural theory deals with various types of structural models that were proposed to explain the formation of glass. These can widely be categorized as models based on randomness and models based on crystallographic order. Properties of glass vary slightly from those of crystals and can be seen from the density and the internal energy.
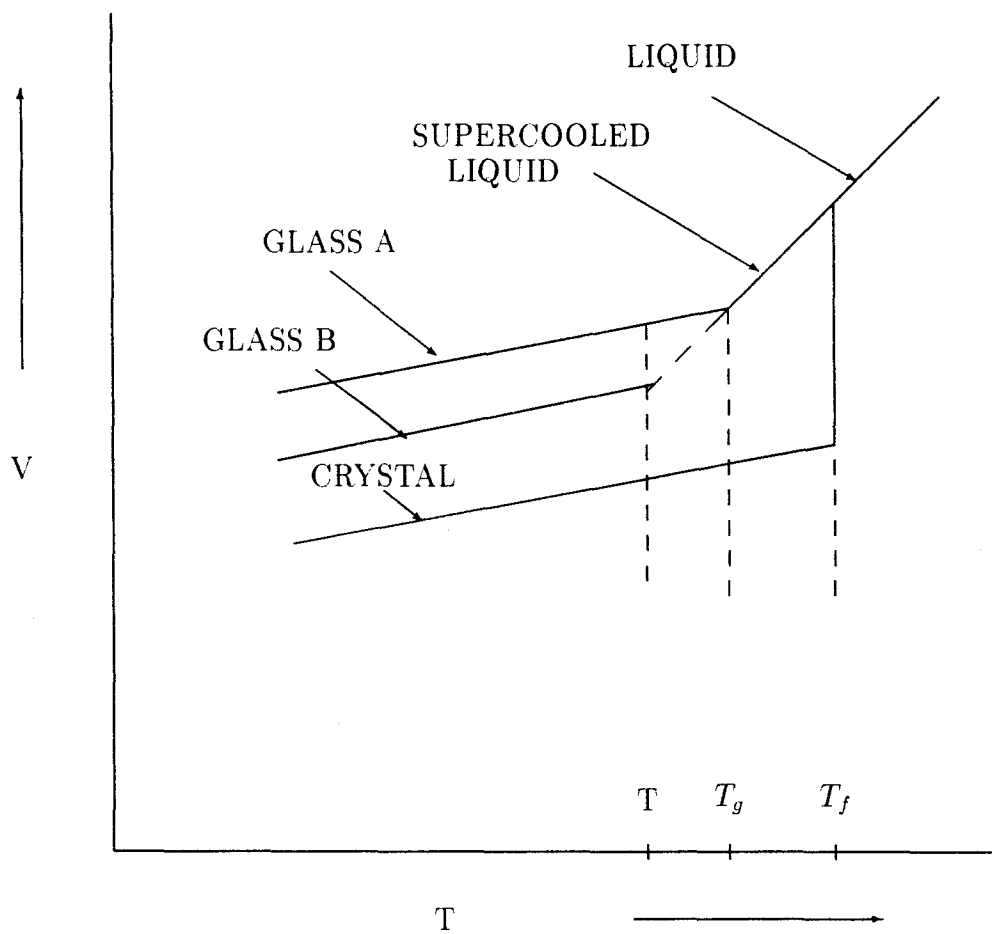
Figure 1.1: Formation of Glass (after Jones [1956])

1.3.1 Random Close Packing (RCP)

This model derives from a random packing of classical hard spheres. It was proposed for monatomic liquids and modified later for binary liquids. Non-crystalline models could be produced by constraining the outer surface to be irregular. Interatomic arrangement can then be explained in terms of irregular polyhedra. Computer modelling of such liquids [Finney and Wallace (1981)] minimized the number of large polyhedra with most of the structure arising from tetrahedra and octahedra. Usefulness of this model was tested for a binary system. Although such models can be constructed for polyatomic species of any shape and size, few attempts have been made to construct such a network.

1.3.2 Continuous Random Network (CRN)

A model, which is closely similar to RCP was proposed by Zachariasen for covalent glasses where the structural unit can be defined e.g. SiO_4 for silicon dioxide glass, BO_3 triangles for boron trioxide glass etc.. The random network can be constructed by connecting such polyhedra, with their relative orientations unconstrained. The restrictions such as choice of ring statistics and minimum strain energy can be added at a later stage after the construction of such a network. This model is very useful for construction of structures in that the random connection of these units provides a realistic non-crystalline model. Most of the successful models are from this category. This model [proposed by Zachariasen (1932)] which says that the atomic arrangement in a glass is characterized by a continuous network which lacks symmetry and periodicity, was further supported by the work on silica [Warren et al. (1936)] using X-ray diffraction. Incorporation of species such as alkali or alkaline earth atoms can be made by addition of these to the network. The latter approach was subsequently challenged by several researchers and will be discussed later.

1.3.3 Models derived from crystallographic order

Similarity between structures through comparisons of pair correlation functions for glasses and compositionally equivalent crystals provides the idea that the glasses may be formed from microcrystals. Strain induced from lattice mismatch at grain boundaries, defects such as dislocations and the presence of disordered interfacial regions may all give rise to regions of disorder smaller than the grain size.

Simple microcrystalline model

This model [Cargill (1970)] originated from a possible model for amorphous $Ni-P$ alloys which predicted that Ni atoms are hexagonally close packed in the region of 20 Å. Similarly, RDF's obtained from amorphous Ge and crystalline Ge were not found to be in agreement beyond second neighbours.

Quasi-crystalline model

This model is based on crystalline polymorphs with variable correlation length [Leadbetter and Wright (1972)]. According to this, glass is made of quasi-crystals in which the crystallinity gradually decreases as the length approaches a correlation length which is of the order of 10 Å to 20 Å . These quasi-crystals are embedded in an homogeneous disordered matrix. Although this model gives close agreement with experiment for the structure of the local environment, large differences at higher values of r are observed.

Paracrystalline model

Hosemann et al. [1986] and Phillips [1982] have used the term 'paracrystalline' while describing models for amorphous solids. This is based on disordered regions over interplanar distances. From cation/anion ratios of some glass forming oxides in the range 0.2 to 0.4, and the presence of tetrahedral bonding in crystals having the same radius ratios, Goldschmidt [1926] considered that tetrahedral bonding was necessary for the formation of

glasses. Several authors have considered the process of glass formation based on the nature of interatomic bonds rather than the structure. Stanworth's electronegativity criterion led to the rediscovery of Tellurite glasses [Stanworth (1946), (1948a, b), (1952)].

1.4   Zachariasen's model of glass

For oxide glass formation, Zachariasen proposed that the structure of glass may be considered to be made up of oxygen polyhedra which connect together in a 3-D arrangement to form a glass. For the internal energy of a glass to be only slightly higher than that of a crystal, it must contain polyhedra of the same type as the crystal and must be joined together in a similar way. Thus, since the crystalline forms of silica are made up of SiO_4 tetrahedra, its vitreous form must also be constituted of these units. However unlike a crystal, a glass would have a variation in relative orientation of adjacent tetrahedra. Zachariasen formulated the following rules for oxides to be glass formers: They are :

1. No oxygen atom may be linked to more than two cation atoms A.

2. The number of oxygen atoms surrounding each cation must be small.

3. The oxygen polyhedra share corners with each other, not edges or faces.

Oxides of the type AO and A_2O cannot satisfy these conditions and therefore should not form glasses and indeed the oxides of Groups I and II do not form glasses with the exception of water.

Rules 1, 2, and 3 are satisfied by

1. the oxide type A_2O_3 if the oxygens form a triangle around A

2. the oxides AO_2 or A_2O_5 if the oxygens form tetrahedra and

3. by oxides AO_3, A_2O_7 and AO_4 if the oxygens form octahedra.

The nonoxide BeF_2 also satisfies the above rules when 'oxygen' is replaced by 'fluorine'. Thus BeF_2 glass is made up of BeF_4 tetrahedra.

For more complex oxide glasses, Zachariasen proposed that glass formation occurred;

1. if the sample contains a high percentage of cations which are surrounded by oxygen tetrahedra or oxygen triangles

2. if the tetrahedra or triangles share corners with each other and

3. if the oxygen is linked with only two cations and does not make further bonds.

These rules imply that the sample must contain a high percentage of glass forming cations or any other cations which are able to replace them isomorphically. The cation Al^{3+} for example can replace Si^{4+} since it resembles many silicate structures. Such cations form the network of the glass and are therefore termed as 'network-forming-oxides'. The oxides which do not take part in the formation of a network are called 'network-modifiers'. After the publication of the theory by Zachariasen, Warren (1941) studied simple binary glasses and the results were interpreted using the CRN model explaining the way in which alkali and alkaline earth cations are incorporated in the network. The conclusions drawn from this study were that each Si is surrounded by four oxygens as per Zachariasen's formulation. The structure of silicate glass containing Na_2O was considered to be made up of Si tetrahedra with Na atoms partially bonded to a tetrahedral oxygen thereby modifying the network. The oxygens connected to two Si atoms were termed 'bridging' oxygens while those connected to the Na atom were 'non-bridging' oxygens.

1.4.1 Limitations of Zachariasen's model

According to Zachariasen's model for glasses, network-modifying elements which adjust the connectivity and dimensionality of the network have weak, ionic and non-directional bonds [Gaskell (1985)]. Their coordination environments are considered to be more distorted and variable than in crystals, and their spatial distributions are regarded as random or

homogeneous [Rawson (1967)]. This view of the structure of glass developed by Zachariasen and Warren of 'CRN' has been questioned by several researchers in recent years by new experimental findings from elemental specific EXAFS [Brown et al. (1986), Greaves (1990)] as well as neutron and X-ray scattering measurements [Wright et al. (1982), Milberg and Peters (1969), Yasui et al. (1983)]. Both techniques supply environmental information around a particular element, be it glass former or modifier.

1.5 Kinetic theory

Kinetic theory basically deals with the processes of crystal nucleation and growth, and the limiting values of these processes. Their values, when exceeded, affect glass formation. Turnbull and Cohen [1958, 1960, 1961] proposed the theory of vitrification based on the formation of crystal nuclei. One of the important results of this theory is the determination of minimum activation energy for glass formation and is stated as [Turnbull and Cohen (1958)];

$$\frac{\Delta T'}{T_m} = \left(\frac{2\pi}{3} \frac{RT_m}{80RT' - \Delta G'} \right)^{1/2} \tag{1.1}$$

where T_m is the melting temperature. $\Delta G'$ is the free energy of crystallization and T' is the temperature at which the value of the rate of nucleation is 1 cm^{-3} sec^{-1}. A glass will be formed if the rate of crystal growth at T' is less than 10^{-5} atom spacings per second. A value of T' satisfying the above equation can be found if $\Delta G'$ is less than $40RT_m$. The condition for rate of nucleation is satisfied when $\Delta G' \geq 40RT_m$. The velocity of crystal growth however, will be less than 10^{-5} atomic spacings per second if $\Delta G'$ is greater than $30RT_m$. Thus for glass formation in this description, the activation energy must exceed $30RT_m$. From this theory which leads to the relation $T_m = \Delta v_m / \Delta S_m$ (where Δv_m is the energy and ΔS_m is the entropy of crystallization), it follows that "the greater the glass forming ability, the lower are the values of energy required to produce a given amount of disorder".

Sun [1947] postulated that the process of melting and crystallization depends upon the

strength of the bonds. If the bonds are stronger, the material is likely to be more viscous thereby increasing the probability of forming a glass. Using this criterion, bond strength was calculated for many oxides and was found to be higher for silica, boron trioxide etc.

Rawson [1967] after pointing out that the ratio of bond strength to melting temperature should be taken into account, explained glass formation in multicomponent systems. In such systems, he observed that glass formation is seen where the liquidus temperature of the system is low.

Kinetic theory in general explains the dependence of glass formation on the strength of bonds which have to be broken during crystallization, and the thermal energy available for this.

1.6 Techniques for probing structures

Structures may be probed by the following experimental techniques;

1. Diffraction : X-ray, Neutron and Electron

2. Scattering : Small Angle X-ray and Small Angle Neutron Scattering

3. Spectroscopy : IR, Raman, UV/visible, EXAFS, ESCA

4. Macroscopic measurements : Density, Molar volume etc.

The diffraction technique yields an overall Radial Distribution Function (RDF) that can be interpreted upto a few angstrom units for simple systems. The RDF is a superposition of various constituent pair distribution functions. X-rays, neutrons and electrons are scattered respectively by core electrons, nuclei and the atomic electron clouds. With all three probes, the relative positions of atoms are obtained through real space correlation functions to yield one dimensional average projections. The overall structure may then be deduced from a comparison of data from such experiments and the construction of models through computer simulation methods such as Reverse Monte Carlo (RMC) and Molecular Dynamics (MD).

9

Since these techniques produce one-dimensional RDF, knowledge of the chemical bonding in the structure is necessary to identify the features in the component correlation functions. Crystal structures of analogous compounds provide this information. Computer modelling studies such as MD can probe short range order of the glasses when a good interaction potential function is available. This is generally obtained by trial and error or ab-initio methods until a good fit between the experimental and theoretically simulated values for some physical properties is obtained.

The Reverse Monte Carlo (RMC) technique [McGreevy and Pusztai (1988)] is based on the Monte Carlo algorithm, in which instead of minimizing the energy, the squared difference between the experimental and calculated structure factor from an initial configuration is minimized. The structure is modified by moving the atoms until the calculated structure factor agrees with the experimental one within some acceptable limit of error.

Several researchers [Momiuchi (1986), Hosokawa et al. (1991)] have demonstrated Energy Dispersive X-ray Diffraction (EDXD) in studying disordered systems. Here the energy dependence of scattered intensity is detected by utilizing white radiation at a fixed diffraction angle. Subsequent to correction for Compton scattering, the scattered signal as a function of momentum transfer is calculated. This method has many advantages such as measurement of the intensity function $i(s)$ upto a relatively high value of momentum transfer e.g. 25 Å^{-1}. Mechanical movement is not necessary minimizing the errors due to optical misalignment. However, the availability of a detector having good energy resolution may sometimes be difficult.

Small angle X-ray and neutron scattering yield information on longer range order, formation of clusters in glasses or microstructure due to phase separation in a glass. Many spectroscopic measurements such as IR, UV/visible, EXAFS, ESCA can be used for structure determination. EXAFS is an atom specific technique and can be used to study the structural environment of any particular atom giving accurate information of interatomic distances in the first shell. Techniques such as IR, Raman mainly deal with molecular vibra-

tions and can be sensitive in probing the structure of glasses. In these methods, structural information can be obtained by comparing calculated vibrational characteristics of an assumed structure with those obtained from the measurements. ESCA provides information about the number of non-bridging oxygen atoms in oxide glasses and the valence state of an atom. Macroscopic measurements such as density, molar volume yield information about the compactness of glass. In the present work, X-ray and neutron diffraction, IR and UV/visible techniques have been used.

1.7 Nuclear-Waste glasses

The residual solutions produced by the reprocessing of spent nuclear reactor fuel have a high level of radioactivity and constitute high-level waste. The radioactivity may be of the order of a thousand Curies per litre. Storage of this waste presents a serious current problem of nuclear power. The half lives of many radionuclides in high-level waste are of the order of hundreds, thousands and hundreds of thousands of years. Thus, any scheme for the storage of such waste requires long-term mechanical integrity and chemical inertness with the objective of minimizing the interaction of radioactive waste with the environment. In recent times, a widely accepted technique for such storage has been the vitrification of the nuclear waste from reprocessing. Glass is a suitable candidate for it has a number of advantages:

a) It is capable of bonding with all of the chemically different fission product elements at high temperatures and can be used with considerable flexibility.

b) It is a homogeneous, isotropic material which is also impermeable and thus presents only a limited exchange surface area.

c) It is highly resistant to heat and radiation.

d) It is easy to manufacture with a minimum of intermediate process steps liable to generate secondary wastes.

1.8 Phosphate glasses

Phosphate glasses are used presently in a number of applications. P_2O_5 has attracted glass researchers due to its comparatively low melting temperature and ease of glass formation. The disadvantage in using phosphate glasses is that they are hygroscopic. Addition of Al_2O_3 or B_2O_3 increases the degree of cross-linked bonds in the glass and reduces the hygroscopic nature of the phosphate. Some borophosphates and aluminophosphates with a chemical durability similar to that of silicate glasses can be prepared. The hygroscopic nature of P_2O_5 has been used in the treatment of crops and animals suffering from trace element deficiencies [Knott (1989)]. These glasses dissolve at a controlled rate releasing transition metal additives. Glasses doped with halides have high ionic conductivities and are under study for battery applications [Ravaine (1985)]. The discovery of laser action in glass [Snitzer (1961)] initiated a new chapter in the world of glass research. Subsequent to this discovery, glass lasers use trivalent lanthanides as active ions whose wavelengths vary with the host matrix. Among all glasses, phosphates were found to offer the best overall combination of properties for many laser applications [Weber (1990)].

1.9 Objectives of the present work

The major hazard in the long term storage of nuclear waste arises from the action of water on the stored waste and possible subsequent contamination of the environment. Thus it becomes essential to know the chemical stability of the glass. Several studies have been performed to understand the leaching behaviour [Bault et al.(1978), Mcvay and Buckwalter (1980)] of glass subjected to boiling water for extended periods of time. In these measurements. the loss in weight is measured. This determines the 'leaching rate' of a particular composition. Thermal stability also plays a major role in the selection of a suitable candidate for the waste storage. Knowledge of the structure of such a system becomes essential in understanding some of its chemical and physical properties. Diffraction is a powerful technique

12

to study the structure of a glass in the short and medium range. In order to study the effects of added nuclear waste on the host boro-silicate network, glasses having high concentrations of simulated (non-radioactive) nuclear waste were studied using X-ray and neutron diffraction. A system having n components gives rise to $n(n+1)/2$ different correlations. Thus, for the complete elucidation of the structure, $n(n+1)/2$ independent diffraction experiments are necessary with a variation in the parameters such as the scattering factor, wavelength etc. Thus, only major changes in the boro-silicate host network caused by waste inclusion can be followed in the relatively low resolution diffraction experiments reported here.

In order to gain a better understanding of the effect that the elements constituting nuclear waste have on the host network, a phosphate glass former was incorporated with oxides of the lanthanides. It was intended to study the effect of these inclusions on the P_2O_5 network by X-ray and neutron diffraction. Topologically, vitreous silica and P_2O_5 have similar structures where the basic unit is a tetrahedron. As stable glasses doped with high concentrations of rare-earths find many applications, an additional incentive in studying these phosphates was to have insight into some of their basic physical properties. In the present work, such glasses were prepared and structurally characterized using diffraction, spectroscopic and other techniques.

Chapter 2

THEORY

2.1 Introduction

X-rays and neutrons having wavelengths of the order of interatomic spacings can be used to study matter through the phenomenon of diffraction. Diffraction studies on crystalline substances involves the measurement of interference patterns formed by waves which are elastically scattered from regular planes of atoms. The diffraction patterns of a single crystal and a poly-crystalline substance consist of respectively sharp spots and concentric circles due to constructive interference of scattered waves from different atomic planes. In the case of non-crystalline materials, however, diffuse haloes are observed due to the absence of long-range periodic structures and interference of waves scattered from a random arrangement of centres. From such a diffraction pattern it is possible to determine a one-dimensional average structure by X-ray and neutron scattering techniques and use of a Radial Distribution Function (RDF). The RDF yields information about the average local environment around a given atom such as bond lengths and bond angles. Additional details of the structure can be obtained from a combination of several experimental techniques as well as theoretical modelling studies since each method only yields certain bulk averaged structural parameters.
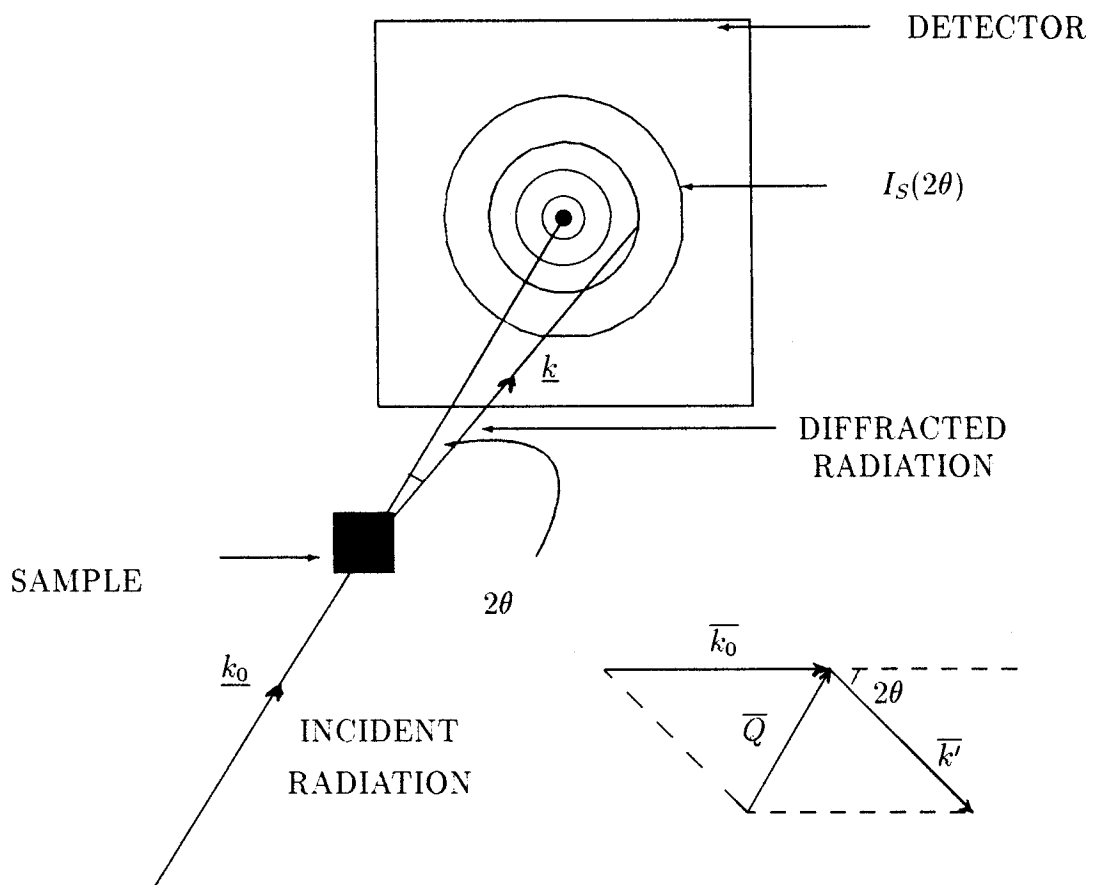
Figure 2.1: Experimental setup of a diffraction experiment

2.2 The Radial Distribution Function

For an FCC lattice made up of atoms with diameter D, as r is increased from 0, no nearest neighbours are observed until $r = D$. At $r = D$, the shell intersects 12 atoms which are the nearest neighbours. This is the first coordination shell and is characterized by two values n_1 and r_1 where n_1 is the number of atoms in the first coordination shell having radius r_1. Increasing r further in an FCC lattice leads to the second nearest neighbour at a distance r_2 with the coordination n_2. Continuing in this manner, a plot of n verses r shows discrete shells having non-zero coordination numbers. This plot is referred to as the Radial Distribution Function. Hence, for a given atom at the origin, the average number of atom centres lying between r and $r + dr$ is given by $4\pi r^2 \rho(r)dr$. The function $\rho(r)$ is the pair correlation function or the density function which has a large value at those distances where there are a large number of atoms. For a crystal, where the atoms are fixed at regular distances, the RDF is the sum of delta functions representing discrete coordination shells. Thus, the RDF is a spatially averaged one dimensional representation of the structure which carries a limited amount of quantitative information describing the atomic scale structure of a non-crystalline solid. At increasing values or r, the density function $\rho(r)$ approaches the average number density $\rho^0(r)$ of particles and the maxima in the RDF oscillate about the average value $4\pi r^2 \rho^0(r)$ while decreasing in amplitude. This reflects the increasing loss of long-range correlations between the origin and distant atoms.

In the theoretical foundations of the RDF method [Zernicke and Prins (1927)], the fourier integral theorem is applied to diffraction data. The description of the structure of a liquid or glass both lacking long-range order requires a space-time correlation function to describe the position of atoms. Such a correlation function is the fourier transform of the scattered intensity function $i(Q)$ and can only be measured with limited resolution for practical reasons which will be discussed later.

The typical geometry of a scattering experiment is shown in Fig 2.1. The incident beam consists of monoenergetic X-rays, electrons or neutrons having energy E such that $\lambda = hc/E$

(for X-ray photons) and $\lambda = h/\sqrt{2mE}$ (de Broglie wavelength) for neutrons and electrons. It is of the order of the interatomic spacing. In principle, the method is straightforward, but involves various corrections and assumptions and some technical difficulties.

2.3 Theory

2.3.1 Neutron scattering

The scattering cross-section for the system of interacting particles can be expressed in terms of a pair correlation function $G(\underline{r}, t)$ which represents the probability that given a particle at any arbitrary origin at $t=0$, there will also be a particle at a vector distance $\underline{r}$ from this origin at time t. $G(\underline{r}, t)$ may be expressed as a sum of a 'self' and a 'distinct' part;

$$G(\underline{r}, t) = G^S(\underline{r}, t) + G^D(\underline{r}, t) \qquad (2.1)$$

where the $G^S(\underline{r}, t)$ represents the correlation of a particle with itself and $G^D(\underline{r}, t)$ is the correlation with any other particle. These functions can be obtained from a scattering experiment where the number of scattered neutrons of a monochromatic incident beam is measured as a function of the scattering angle 2θ or momentum transfer $\underline{Q}$. The magnitude of Q in elastic scattering is given by

$$|Q| = \underline{k_0} - \underline{k} = \frac{4\pi \sin \theta}{\lambda} \qquad (2.2)$$

where $\underline{k_0}$ and $\underline{k}$ are the incident and scattered wavevectors (Fig 2.1). The magnitude of $\underline{k_0}$ is $2\pi/\lambda$ where λ is the neutron wavelength.

A detailed derivation of the double differential neutron scattering cross-section per unit solid angle (Ω) and energy interval $(\hbar\omega)$ in terms of the correlation functions $G^S(\underline{r}, t)$ and $G^D(\underline{r}, t)$ was given by Van Hove [1954]. The total double differential cross section may also be expressed as a sum of self and distinct scattering cross sections [Placzek (1952)];

$$\frac{d^2\sigma}{d\Omega d\omega} = \frac{d^2\sigma^S}{d\Omega d\omega} + \frac{d^2\sigma^D}{d\Omega d\omega} \qquad (2.3)$$

17

where, for several atomic species,

$$\frac{d^2\sigma^S}{d\Omega d\omega} = \frac{N_u}{2\pi} \frac{k}{k_0} \sum_j \overline{b_j^2} \int_0^\infty \int_{-\infty}^\infty G_j^S(\underline{r},t)e^{i(\underline{Q}\cdot\underline{r}-\omega t)} d\underline{r}\,dt \qquad (2.4)$$

and

$$\frac{d^2\sigma^D}{d\Omega d\omega} = \frac{N_u}{2\pi} \frac{k}{k_0} \sum_j \sum_k \overline{b_j}\,\overline{b_k} \int_0^\infty \int_{-\infty}^\infty G_j^D(\underline{r},t)e^{i(\underline{Q}\cdot\underline{r}-\omega t)} d\underline{r}\,dt \qquad (2.5)$$

The j summation is taken over the individual atoms in a composition unit and k over the atom types; N_u is the number of composition units in the irradiated sample and $\overline{b}$ and $\overline{b^2}$ are the isotopically averaged bound atom neutron scattering lengths. For an isolated nucleus, $\frac{d\sigma}{d\Omega}$ is isotropic so that the total scattering cross-section is given by;

$$\sigma_{tot}^s = \int \frac{d\sigma}{d\Omega} d\Omega = 4\pi\overline{b^2} \qquad (2.6)$$

The total scattering cross-section can either be the free-atom σ_f^s or bound atom σ_b^s cross-section. These quantities are related to each other by μ, the mass ratio of nucleus to neutron. Thus,

$$\sigma_b^s = \sigma_f^s \left(\frac{\mu+1}{\mu}\right)^2 \qquad (2.7)$$

The total scattering cross-section is a sum of two terms, the phase dependent term, σ_{coh}^s, the coherent scattering cross-section per atom and the phase independent term, σ_{incoh}^s, the incoherent scattering cross-section such that

$$\sigma_{tot}^s = \sigma_{coh}^s + \sigma_{incoh}^s \qquad (2.8)$$

$$\sigma_{coh}^s = 4\pi\overline{b}^2 \qquad (2.9)$$

$$\sigma_{incoh}^s = 4\pi(\overline{b^2} - \overline{b}^2) \qquad (2.10)$$

Scattering laws for self and distinct terms are defined by;

$$S_j^S(\underline{Q},\omega) = \frac{1}{2\pi} \int_0^\infty \int_{-\infty}^\infty G_j^s(\underline{r},t)e^{i(\underline{Q}\cdot\underline{r}-\omega t)} d\underline{r}\,dt \qquad (2.11)$$

18

$$S_{jk}^D(\underline{Q}, \omega) = \frac{1}{2\pi} \int_0^\infty \int_{-\infty}^\infty G_{jk}^D(\underline{r}, t) e^{i(\underline{Q}\cdot\underline{r} - \omega t)} d\underline{r}\, dt \tag{2.12}$$

Thus,

$$\frac{d^2\sigma^S}{d\Omega d\omega} = N_u \frac{k}{k_0} \sum_j \overline{b_j^2} S_j^S(\underline{Q}, \omega) \tag{2.13}$$

$$\frac{d^2\sigma^D}{d\Omega d\omega} = N_u \frac{k}{k_0} \sum_j \sum_k \overline{b_j}\ \overline{b_k} S_{jk}^S(\underline{Q}, \omega) \tag{2.14}$$

The correlation function can then be obtained from the scattering law by fourier transformation:

$$G(\underline{r}, t) = \frac{1}{(2\pi^3)} \int_0^\infty \int_{-\infty}^\infty S(\underline{Q}, \omega) e^{i(\underline{Q}\cdot\underline{r} - \omega t)} d\underline{Q}\, d\omega \tag{2.15}$$

A diffraction experiment involves the measurement of all neutrons scattered at a particular angle, namely the differential scattering cross-section;

$$\frac{d\sigma}{d\Omega} = \int_{-\infty}^\infty \frac{\epsilon(E)}{\epsilon(E_0)} \frac{d^2\sigma}{d\Omega d\omega} d\omega \tag{2.16}$$

where $\epsilon(E)$ is the detector efficiency which in this study is assumed to be an exponential function of Q. $\epsilon(k) = 1 - e^{ak/k_0}$ and a is a constant dependent on detector constant. $\epsilon(E)/\epsilon(E_0)$ generally has the form k/k_0. Thus integrating equation (2.3) with respect to ω leads to:

$$\frac{d\sigma}{d\Omega} = \frac{d\sigma^S}{d\Omega} + \frac{d\sigma^D}{d\Omega} \tag{2.17}$$

$$\frac{d\sigma^S}{d\Omega} = N_u \sum_j \overline{b_j^2} \int_0^\infty G_j^D(\underline{r}, 0) e^{i(\underline{Q_0}\cdot\underline{r})} d\underline{r} \tag{2.18}$$

$$\frac{d\sigma^D}{d\Omega} = N_u \sum_j \sum_k \overline{b_j}\ \overline{b_k} \int_0^\infty G_{jk}^D(\underline{r}, 0) e^{i(\underline{Q_0}\cdot\underline{r})} d\underline{r} \tag{2.19}$$

The quantities $G_j^S(\underline{r}, 0)$ and $G_{jk}^D(\underline{r}, 0)$ are the instantaneous pair correlation functions which are respectively equal to $\delta(r)$ and $\rho_{jk}(r)$. The latter, $\rho_{jk}(r)$, is the number density of k atoms at a distance r from the atom j.

For isotropic materials, the differential scattering cross-section may be averaged over all relative orientations of the vector $\underline{Q_0}$ and $\underline{r}$ to give

$$\frac{1}{N_u} \frac{d\sigma}{d\Omega} = I_N(Q_0) = \sum_j \overline{b_j^2} + \sum_j \sum_k \overline{b_j}\ \overline{b_k} \int_0^\infty 4\pi r^2 \rho_{jk}(r) \frac{\sin Q_0 r}{Q_0 r} dr \tag{2.20}$$

A correlation function may now be defined such that;

$$d_{jk}(r) = 4\pi r(\rho_{jk}(r) - \rho_k^0(r)) \qquad \text{and} \qquad d_k^0(r) = 4\pi r\rho_k^0 \qquad (2.21)$$

where ρ_k is the average number density of k atoms. This density when transformed into Q-space is a delta function at $Q = 0$ which is normally not measured in the experiments as transmitted neutrons also contribute to the intensity at this value of Q. Denoting this function as $I_N^0(Q_0)$;

$$i_N(Q_0) = I_N(Q_0) - \sum_j \overline{b_j^2} - I_N^0(Q_0) \qquad (2.22)$$

Thus,

$$Q_0 i_N(Q_0) = \sum_j \sum_k \overline{b_j}\, \overline{b_k} \int_0^\infty d_{jk}^N(r) \sin Q_0 r\, dr = \sum_j \sum_k Q_0 i_{jk}^N(Q_0) \qquad (2.23)$$

$d_{jk}(r)$ may be obtained by fourier transformation of the above relation

$$d_{jk}^N(r) = \frac{2}{\pi \overline{b_j}\, \overline{b_k}} \int_0^\infty Q_0 i_{jk}^N(Q_0) \sin r Q_0\, dQ_0 \qquad (2.24)$$

A differential correlation function $D_N(r)$ may be defined as the fourier transform of $Q_0 i_N(Q_0)$

$$D_N(r) = \frac{2}{\pi} \int_0^\infty Q_0 i_N(Q_0) \sin r Q_0\, dQ_0 \qquad (2.25)$$

and

$$D_N(r) = \sum_j \sum_k \overline{b_j}\, \overline{b_k} d_{jk}^N(r) \qquad (2.26)$$

The RDF $g_N(r)$ is related to $D_N(r)$ by the expression

$$g_N(r) = r[D_N(r) + D_N^0(r)] \qquad (2.27)$$

$$g_N(r) = r[T_N(r)] \qquad (2.28)$$

where $T_N(r)$ is the total correlation function and

$$D_N^0(r) = (\sum_j \overline{b_j})^2 4\pi r\rho^0 \qquad (2.29)$$

ρ^0 being the number of composition units per unit volume.

2.3.2 X-ray scattering

The derivation of the formalism of X-ray scattering is similar to that of neutrons which is already discussed in detail in the previous section. In the case of X-rays, the neutron scattering length is replaced by the atomic scattering factor which is a function of Q.

Thus an expression similar to eq(2.22) can be written for the intensity function $i_x(Q_0)$ such that

$$Q_0 i_x(Q_0) = Q_0[I_x^{coh}(Q_0) - \sum_j f_j^2(Q_0) - I_x^0(Q_0)] = \sum_j \sum_k Q_0 i_{jk}^x(Q_0) \qquad (2.30)$$

where

$$Q_0 i_{jk}^x(Q_0) = f_j(Q_0) f_k(Q_0) \int_0^\infty d_{jk}(r) \sin Q_0 r \, dr \qquad (2.31)$$

and

$$D_x(r) = \frac{2}{\pi} \int_0^\infty Q_0 i_x(Q_0) \sin r Q_0 dQ_0 \qquad (2.32)$$

This function is directly related to the electronic distribution function. In order to improve the real space resolution, $Q_0 i_x(Q_0)$ is divided by a sharpening function $f_e^2(Q_0)$ where $f_e(Q_0)$ is the average form factor per electron.

$$f_e(Q_0) = \frac{\sum_j f_j(Q_0)}{\sum_j Z_j} \qquad (2.33)$$

Thus the differential correlation function $D_x(r)$ becomes;

$$D_x(r) = \frac{2}{\pi} \int_0^\infty \frac{Q_0 i_x(Q_0)}{f_e^2(Q_0)} \sin r Q_0 dQ_0 = \sum_j \sum_k d_{jk}^x(r) \qquad (2.34)$$

Similarly the fourier transform of the function $Q_0 I_x^0(Q)/f_e^2(Q_0)$ gives

$$D_x^0(r) = (\sum_j Z_j)^2 4\pi r \rho^0 \qquad (2.35)$$

and the radial distribution function

$$g_x(r) = r[D_x(r) + D_x^0(r)] = r T_x(r) \qquad (2.36)$$

2.3.3 Effect of Finite Q_{max}

The collection of reliable data in both X-ray and neutron diffraction is experimentally limited to some finite value while the expression for the scattered intensity (eq.(2.20)) assumes integration upto an infinite value of Q. Thus $I(Q)$ does not diminish to zero at the maximum measured value of Q. This leads to termination ripples which might be misinterpreted as real features in the fourier transformed function. Such features thus need to be suppressed by multiplying $Q_0 i(Q_0)$ by a modification function by which the measured $I(Q)$ smoothly decreases to zero at Q_{max}. The product of these two functions is then fourier transformed. The modification function due to Lorch [1969] was used here;

$$M(Q_0) = \frac{\sin(\pi Q_0/Q_{max})}{\pi Q_0/Q_{max}} \qquad Q_0 \leq Q_{max} \qquad (2.37)$$

$$= 0 \qquad Q_0 > Q_{max} \qquad (2.38)$$

in which $\pi/Q_{max} = \Delta r$ is the resolution length in real space. Such functions lead to a suppression of termination ripples but degrade the real space resolution.

2.4 Interpretation of Results

Multiplication of $Q_0 i(Q_0)$ by $M(Q)$ leads to the convolution of the true component correlation functions with the peak shape function $P_{ij}(r)$ which is the cosine transform of $M(Q)$ as the latter is an even function in Q. In low Q_{max} measurements, the widths of peaks at low r are mostly due to the peak shape function. For X-rays and neutrons these functions may be written as;

$$P_{jk}^N(r) = \frac{\overline{b_j}\,\overline{b_k}}{\pi} \int_0^{Q_{max}} \frac{\sin(\Delta r Q_0)}{\Delta r Q_0} \cos r Q_0 dQ_0 \qquad (2.39)$$

$$P_{jk}^x(r) = \frac{1}{\pi} \int_0^{Q_{max}} \frac{f_j(Q_0)f_k(Q_0)}{f_e^2(Q_0)} \frac{\sin(\Delta r Q_0)}{\Delta r Q_0} \cos r Q_0 dQ_0 \qquad (2.40)$$

The value of $P^N(0) = 0.18764 Q_{max}$. Similar functions may be found in the work of Mozzi and Warren [1969].

Use of $P_{ij}(r)$ results in the reduction in the height of peaks in the correlation function together with the symmetrical broadening of peaks in $D(r)$ and $T(r)$ but asymmetrical in $g(r)$ on account of the multiplication of $T(r)$ by r which leads to inaccurately large values of peak positions. It is therefore advisable to use the total correlation function in which peaks are symmetrical in $T(r)$. The area under the peak at distance r' is then given by $\sum_j \sum_k n_{jk} A_{jk}/r'$ where n_{jk} is the number of k atoms at a distance r' from the jth atom in a composition unit and

$$A_{jk} = \int_{-\infty}^{\infty} P_{jk}(r)dr \qquad (2.41)$$

where the integration includes satellite ripples.

2.5 The effect of errors

Errors in any experiment may be divided into additive $E(Q_0)$ and multiplicative $\epsilon(Q_0)$ parts [Wright(1974)].

$$Q_0 i''(Q_0) = [1 + \epsilon(Q_0)]Q_0 i'(Q_0) + Q_0 E(Q_0) \qquad (2.42)$$

where the prime indicates measured X-ray and neutron intensities.

$$D''(r) = \int_0^{\infty} D'(u) \; P''(r - u)du + R(r) \qquad (2.43)$$

The peak function $P''(r)$ is a cosine transform of $[1 + \epsilon(Q_0)]$ and $R(r)$ the sine transform of $Q_0 E(Q_0)$. Errors of this type arise from the inaccuracies in the experimental intensities at large Q_0 and due to insufficient smoothing of statistical deviation since one erroneous point at Q_0' gives rise to a noise waveform with a period equal to $2\pi/Q_0'$ in r-space. Conversely. high frequency noise in Q-space leads to a feature in real space which is often at much higher value of r than most intermediate order structural studies deal with.

Inaccuracies may also result from the tabulated values of the atomic scattering factors. Compton intensities and the anomalous dispersion corrections. These calculations are based

on either free atoms or ions. Errors in the values of neutron scattering lengths and total self scattering cross sections contribute to the errors in $D(r)$. These quantities may contain random and systematic errors of the order of 10%. Such inaccuracies lead to incorrect coordination numbers and can be minimized by the Krogh-Moe-Norman renormalization method (Chapter 3), but not eliminated as uncertainties in compositions, packing densities and peak positions each have their own contributions to the total error.

2.6   Limitations of the RDF method

The information obtained using the method of the radial distribution function does not produce a unique structural model. Given an RDF, several models can be constructed which are topologically disordered, yet produce the same correlation function. The width of the first peak which is related to the coordination number, directly depends on the value of Q_{max}. However, the use of RDF has reduced the speculation of possible structures and has led to models like the Random-Network model for metallic glasses and Continuous Random-Network model for covalent glasses.

In preparing a model, the separation of partial correlations is necessary. This can be achieved by performing separate experiments wherein the scattered intensity is varied by varying different parameters. It is known that the neutron scattering length varies from isotope to isotope of any atom. Isotopic substitution therefore can be used as an aid in separating out the partial correlation functions. Some atoms such as Sm, Dy display anomalous scattering for the reason that their scattering length changes with the incident neutron wavelength in the thermal energy range. This property can be used to obtain some partial correlation functions for a multicomponent system. Isotopic substitution cannot be applied for X-rays since they are scattered by the outer electrons of atoms. However, the atomic scattering factor which is a function of Q can be varied by the phenomenon called *resonance scattering*, by measuring the scattering intensity function near an absorption edge of the

constituent atom. Here the atomic scattering factor can be written as

$$f(Q,\omega) = f^0(Q) + f'(Q,\omega) + f''(Q,\omega) \tag{2.44}$$

The last two terms in the above expression are called the 'dispersion corrections' and have significant effect near the absorption edge. Thus a model can be constructed by comparing individual results of these experiments.

Chapter 3

EXPERIMENTAL TECHNIQUES

This chapter deals with the various experimental techniques that have been used in this work. X-ray and neutron diffraction measurements were the main methods used in studying the short and medium-range structure of the glass systems considered in this thesis. Sample preparation, density measurements and compositional analysis by neutron activation analysis and wet chemical method are also discussed. In addition, the chapter includes a brief outline of additional techniques such as IR, UV/Visible absorption spectroscopy and A.C. magnetic susceptibility.

3.1 Complementary nature of X-ray and Neutron diffraction

Detailed information on the spatial arrangement of atoms in a sample may be obtained if the incident radiation has a wavelength which is of the order of interatomic spacings. Both X-rays and neutrons meet this requirement and are thus used in structure determination. X-rays are scattered by the atomic electron clouds whereas neutrons are diffracted by the atomic nuclei and the component correlation functions relating to structure are thus differently weighted in the two techniques. Thus the data from these complementary methods may

be used together. Separation of component correlation functions from the RDF has always been a difficult task and techniques such as anomalous dispersion and isotopic substitution have been used on binary systems. Energy dependence of the form-factor of X-rays near the absorption edge of an atom has also been used [Matsubara et al. (1992)] in structural studies by the X-ray resonance scattering technique. The merits and demerits of X-rays and of neutrons are summarized in Table 3.1.

3.2 X-ray Diffraction

The use of X-rays for structure determination has been widespread on account of X-rays being produced from compact and inexpensive sources. The intensities from these are sufficiently high for relatively rapid measurements on small-sized samples. This has resulted in the extensive use of X-rays in many detailed crystal characterizations. However, as the energies of X-rays are much higher than vibrational modes of condensed matter, they have not been applied to dynamical studies. The application of X-rays to disordered structure measurements is less popular on account of a relatively small scattered intensities at higher scattering angles and low maximum momentum transfer Q_{max} (causing poor real space resolution). Also, a rapidly decreasing form factor results in poor statistics at high angles of scatter. In the measurements on these glasses, a rotating molybdenum anode was used to obtain high incident intensities as well as a higher Q_{max}.

3.2.1 Experimental setup of X-ray diffractometer

The main components of an X-ray diffractometer are an X-ray tube, a goniometer and a counter. X-rays photons are produced when high-energy electrons emitted by the filament get accelerated by a high potential (e.g. 30 KV) and fall on the target which is generally made of Cu, Fe, Ag or Mo. The emitted spectrum of X-rays has the characteristic X-ray line emission superimposed on a continuous background due to bremsstrahlung. The goniometer

Table 3.1: Merits and Demerits of X-rays and Neutrons

Advantages	Disadvantages
X-rays	**Neutrons**
• Convenient laboratory sources and equipment	• Reactor Source required
• Powdered or thick film samples can be used	• Large volume of material required
• Atomic form factor can be calculated	• Scattering length must be determined experimentally for each isotope
• Relatively high incident intensities	• Relatively low incident intensities
Neutrons	**X-rays**
• Partial correlation function easier to extract for multicomponent systems	• Partial correlation function difficult for multicomponent system
• Scattering length independent of Q	• Atomic form-factor strongly decreasing function of Q
• Isotopic substitution possible to determine partial correlation functions	• Isotopic substitution not possible
• High values of Q_{max} possible with pulsed sources	• Small Q_{max} for many laboratory X-ray sources

Tube shield

(1)

S₁

I

R

Focusing
circle

Centre of the
focusing circle

R

(2)

S₂

(3)

III

Counter arm
Counter

I	Focus
II	Rotation axis of the goniometer
III	Axis of the receiving slit
(I)	Divergence slit
(2)	Receiving slit
(3)	Scatter slit
S	Divergence soller slit
S	Receiving soller slit
R	Goniometer radius (185 mm)
$\propto$	Take—off angle
γ	Level divergence angle
Θ	Bragg angle
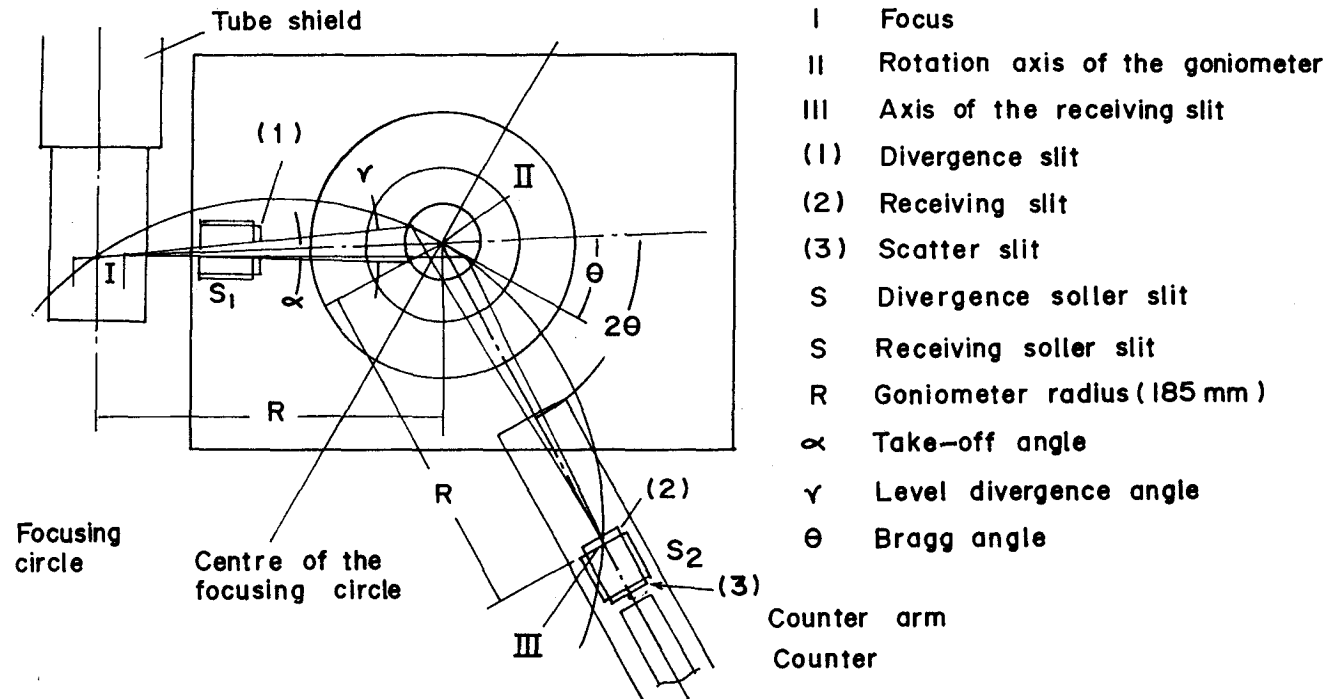
Figure 3.1: Geometric focussing conditions of an X-ray Diffractometer

is designed to satisfy the geometric focussing conditions shown in Fig 3.1. The focussing circle is centered at the sample, and is at right angles to the axis of rotation of the goniometer. The circle involves axis I of the focus of the target, the axis II of the goniometer and axis III of the receiving slit. The radius of the focussing circle is a function of the angle θ formed by the surface of the sample and the direction of the incident X-ray beam; while the angle formed by the straight line connecting axes II and III is 2θ. This angle is always accurately twice the angle θ.

The emergent X-ray beam from the target has an angular divergence α, which is dependent on the particular position of the soller slit S_1 with respect to the target window. This angle is varied by movement of the entire spectrometer with respect to the target window. The divergence, receiving and scattering slit are each held in a soller slit box. The divergence slit determines the horizontal divergence angle of the beam irradiating the sample. The receiving slit is for limiting the width of the diffracted beam. Its angular aperture determines the intensity and resolution of the diffracted beam. The scattering slit limits the diffracted beam incident on the counter. It forms a pair with the divergence slit.

Monochromatization of either the incident or the scattered beam is essential for the study of amorphous samples in order to suppress a large background due to flourescence effects. For this purpose a graphite monochromator was used in the diffracted beam. In mounting the monochromator, the soller slit box (near the detector in Fig. 3.1) is linearly translated towards the sample and in order to maintain the same convergence optics, the receiving and scattering slits are interchanged (Fig. 3.2). An additional slit is placed in front of the detector. The monochromator geometrically satisfies the condition of the focussing and its locus becomes the secondary focal circle. The secondary circle, which passes through the three points: the goniometer receiving slit, monochromator and receiving slit (RS_M) is in the same plane as the primary focal circle and its radius is equal to the curvature of the monochromator crystal (Fig 3.2). The monochromator, along with the scatter slit and receiving slit all sit on the counter arm.

30

Figure 3.2: Ray Diagram of an X-ray Diffractometer
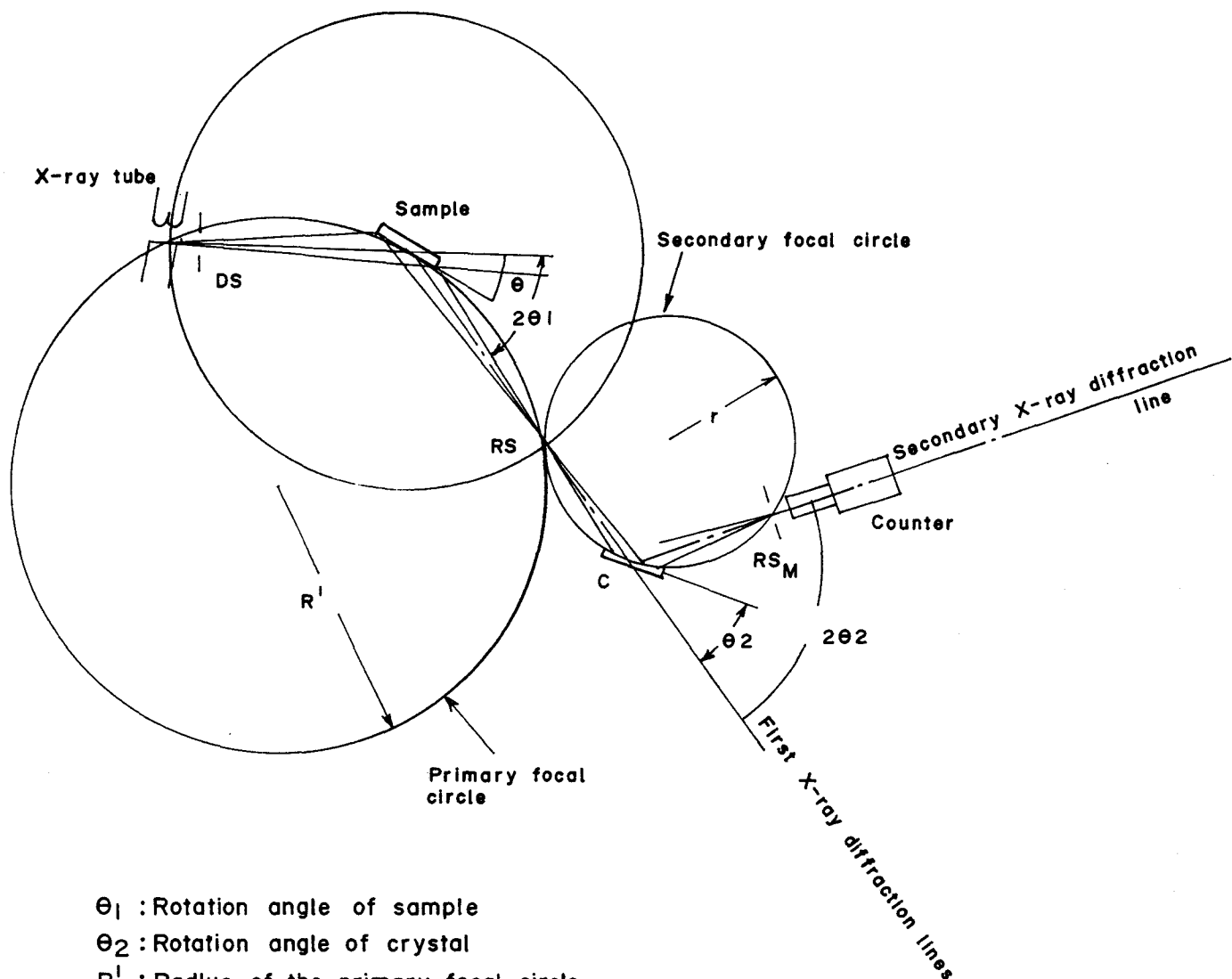
Θ_1 : Rotation angle of sample

Θ_2 : Rotation angle of crystal

R^1 : Radius of the primary focal circle
(Goniometer radius of 185 mm or 250 mm)

r : Radius of the secondary focal circle (Curvature of crystal x 1/2)

DS : Goniometer divergence slit

RS : Goniometer receiving slit

RS_M: Monochromator receiving slit

C : Curved single crystal

31

The diffraction pattern is recorded by measuring the detection rate of pulses in the counter which is either a scintillation counter (used here) or a gas-filled proportional counter. The pulse rate may be measured in different ways. One way is to measure the number of counts per second in which a succession of current pulses is converted into a steady current and measured on a counting-rate meter. In order to reduce the statistical spread in the data, the "step scan" method of counting is used in which the counting-time at each θ is fixed.

3.3   Neutron Diffraction

Neutron diffraction has made progress over the last couple of decades and is now widely used for the characterization of materials. In the early years, neutron diffraction was used in complementing and extending X-ray work. Later, when the intensity of neutron beams increased, neutron scattering experiments became possible. The scattering of neutrons can be elastic and inelastic. Inelastically scattered neutrons are used in probing vibrational properties through energy transfer measurements. As the present work is limited to structural studies, only elastic scattering has been carried out on the medium flux reactor Dhruva at the Bhabha Atomic Research Centre, Mumbai. The maximum flux at the centre is about 1.3×10^{14} neutrons/cm^2/sec. Fission neutrons are produced in the fuel core and escape into the D$_2$O moderator where they slow down to thermal energies. Neutrons for diffraction and other such measurements are taken out through neutron beam holes in the reflector and shielding (Fig.3.3). The typical flux in a beam hole is of the order 10^8 n/cm^2/sec. Monochromatization and collimation of this beam further reduces the flux to approximately 10^4 - 10^5 neutrons/cm^2/sec at the sample position. Since this is a relatively low flux, large specimen samples and longer acquisition times become necessary for improved quality of data.
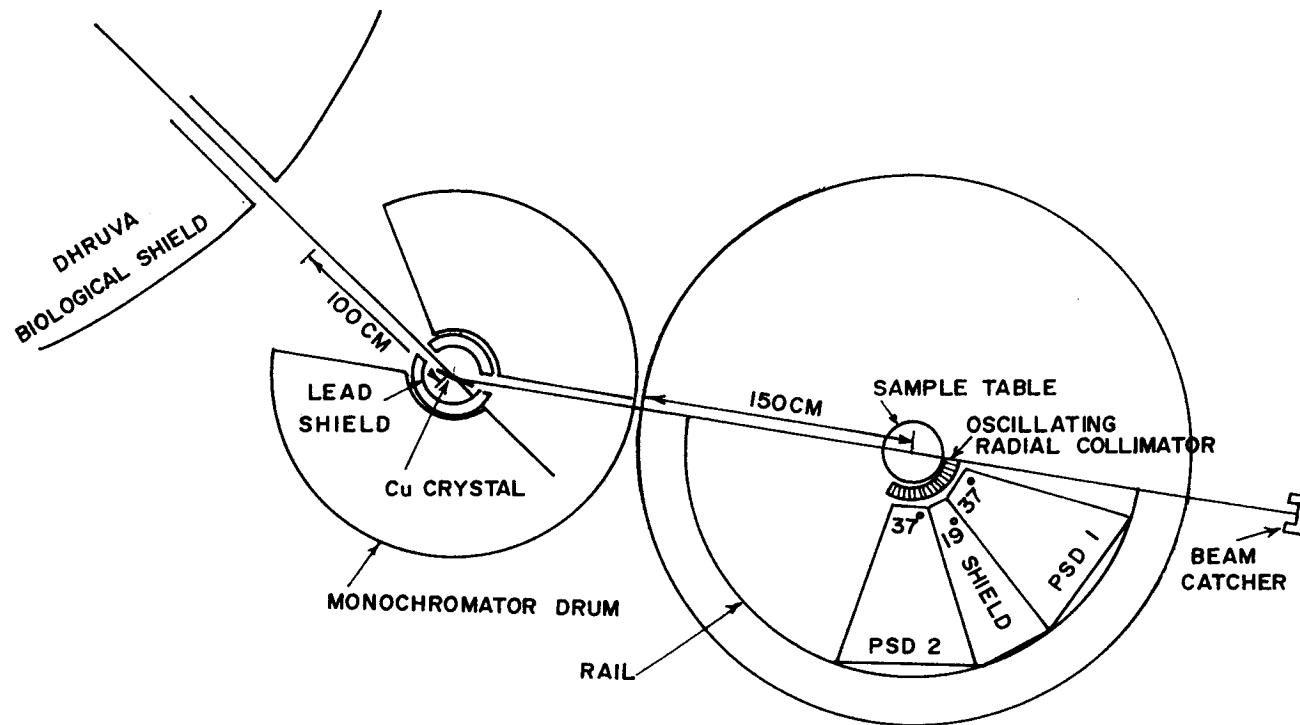
Figure 3.3: Schematic of the High-Q Diffractometer

3.3.1 The High-Q Diffractometer

For neutron elastic scattering measurements, a monochromatic beam is required. In the High-Q Diffractometer used in these measurements (Fig. 3.3), the neutron beam emerges from the reactor through a beam hole and gets monochromatized from a $Cu(220)$ surface. Wavelengths of 0.783 Å and 1.27 Å can be selected at a fixed outgoing angle by rotating a Cu monochromator. A low efficiency BF_3 counter placed in the incident beam acts as a monitor whose counting rate is proportional to the number of incoming neutrons. A sample table of 300 cm diameter accommodates the sample at its center as well as two wedge-shaped detector shields. Two He^3 Position Sensitive Detectors (PSD's) are used where each covers an angular range of 37°. The Q-range of 0.6 Å^{-1} to 15 Å^{-1} was accessed by positioning the detector assembly at a lower and a higher angle position such that an overlap region of about 6° between the two positions was obtained. An Oscillating Radial Collimator (ORC) placed before the detector assembly decreased the background and the contributions arising from the sample environment. Features of the diffractometer are as follows;

Q-range	: 0.3Å^{-1} to 15 Å^{-1}
Resolution $\Delta Q/Q$	: 4%
Incident wavelengths	: 0.783 Å or 1.278 Å
Monochromator	: Cu(220) or Cu(111)
Monochromator take off angle $2\theta_M$	: 34.66 °
Detectors	: 2 He^3 PSD's (each of 100 cm length)
Beam size at sample	: 1.5 cm × 4 cm
Flux value at sample	: 1.1 ×10^6 n/cm^2/sec at λ = 1.278 Å
	10^5 n/cm^2/sec at λ = 0.783 Å

3.4 Corrections involved in the Analysis of Neutron Data

Corrections applied to the neutron diffraction data depend on the experimental setup such as sample and diffractometer geometry which may vary from instrument to instrument. Also, the measured intensity on a chosen instrument depends on the resolution which has both an angular and a wavelength dependent part, it is important to normalize a given data set from an experiment using a standard such as vanadium. The particular geometry of a sample also determines the type of corrections that need to be applied.

3.4.1 Sample container and other background

The size of the sample container depends on two factors:

1. The maximum area of the incident neutron beam that can be utilized.

2. Optimum thickness of the sample so as to enhance the number of counts and reduce the absorption and multiple scattering.

These factors also determine the length of the experimental counting time. Usually, the selection of the sample container is such that at least 10 percent of the incident flux is scattered. Hence large, thin-walled sample containers are often used in these experiments. It is difficult to manufacture thin-walled containers having plate geometry. Dimensions need to be precisely known for the calculation of the number of scattering atoms in the container. Cylindrical containers are often more convenient to use. If the diameter of a container is small, the total sample scattering is relatively lower and the signal to background ratio may decrease. Containers can be made of vanadium or any other null-matrix material having isotropic incoherent scattering. Containers of glass are not usually preferred for measurements on glass samples. In the present study, rectangular cadmium cassettes wrapped in thin aluminium foil were used as sample containers for the nuclear-waste glass samples. The

rare-earth phosphate glasses required no containers as they were chemically inert and their cylindrical geometry was achieved by moulding them at the time of preparation. Container scattering is usually subtracted from the sample-in-container data after correcting for container transmission factors. In the absence of a container, air background is subtracted from the sample intensities. In the nuclear-waste glass measurements reported here, the signal-to-background was relatively low and the background due to epithermal neutrons was thus not negligible. It was measured with a cadmium foil in the incident beam. However, these data were not used as the 'cadmium background' was found to be higher than that due to other sources of background i.e. 'air background'. Subsequent improvements to the diffractometer resulted in the negligible epithermal contamination in the incident beam.

3.4.2 Absorption correction and multiple scattering

Both absorption and multiple scattering corrections depend on the sample geometry. For a plate geometry, the absorption correction is given by;

$$A(Q) = \frac{I}{I_0} = \frac{exp[-\mu t \sec \theta_{in}] - exp[-\mu t \sec \phi]}{\mu t (\sec \phi - \sec \theta_{in})} \tag{3.1}$$

where θ_{in} is the angle of incidence, $\phi = \theta_{in} - 2\theta$ where 2θ is the scattering angle, μ is the absorption coefficient of the sample and t the thickness of the sample. These quantities are illustrated in Fig.3.4.

Paalman and Pings [1962] have evaluated the expressions for cylindrical and annular geometries for X-rays. These can be applied to neutrons. The absorption coefficient is effectively modified because of scattering from the sample and container and has been considered by these authors. For a cylindrical sample without a container, the absorption correction is given by Wright [1974].

$$A(Q) = \frac{I}{I_0} = exp[-(1.7133 - 0.0368 \sin^2 \theta)\mu_a R + (0.0927 + 0.0375 \sin^2 \theta)(\mu_a R)^2] \tag{3.2}$$

where R is the radius of the sample and the absorption coefficient $\mu_a = \sum_k \rho_k \sigma_k^a$.

$$\phi = \theta_{in}\text{-}2\theta$$
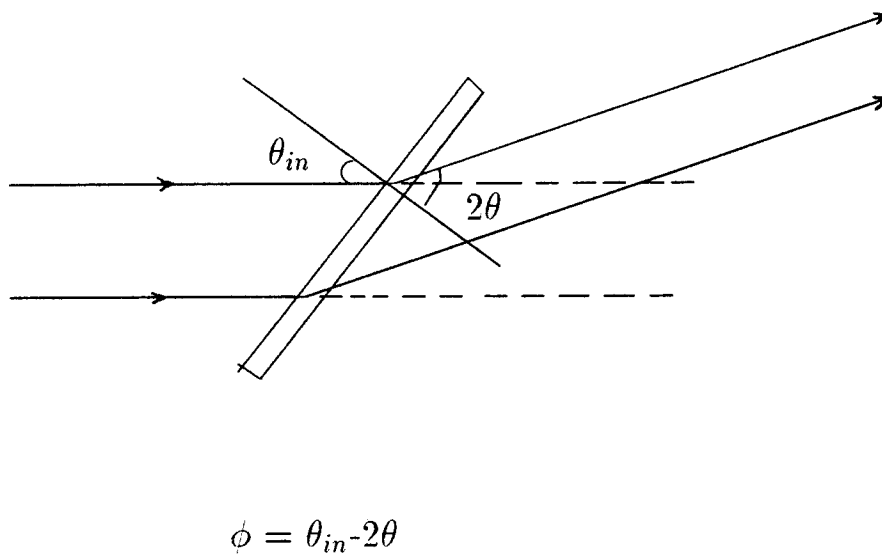
Figure 3.4: Ray diagram of the diffraction measurement of a plane sample in transmission geometry

Multiple scattering was considered to be very small in the case of nuclear-waste glasses since thin samples were used. Corrections for plane samples have been reported by Vineyard [1954], Cocking et al. [1965]. Neutrons undergoing multiple scattering are both removed from the diffraction pattern and returned to it isotropically [Enderby (1968)]. This correction can be evaluated by substituting σ_k^s for σ_k^a in eq.(3.2). For cylindrical samples having multiple scattering less than 10%, Wright [1974] has argued that this correction is equally made of self-shielding and multiple scattering. Multiple scattering corrections for cylindrical samples have also been discussed by Blech and Averbach [1965] and were further modified by Soper and Egelstaff [1980]. The analytical expression for a cylindrical sample is given by

$$I_m = I_1 \left(\frac{exp(2\delta)}{2\delta} - 1 \right) \tag{3.3}$$

where I_m and I_1 are respectively the multiply and singly scattered intensities and δ is the ratio of secondary to primary scattering I_2/I_1. Values of δ are listed by Blech and Averbach [1965]. The appropriate values from this list have been used for these samples.

3.4.3 Normalization

Corrected scattered intensities are placed on an absolute scale by comparing them to the data from a sample having a known cross-section. Vanadium is used for this purpose as it scatters almost incoherently ($\sigma_s = 5.13$ barns, $\sigma_{coh} < 0.03$ barns) and isotropically. Normalization to a standard sample also permits the removal of certain systematic errors of the instrument. The number of scattering atoms of both sample and the normalization standard must be known accurately. Scattering lengths must also be known correctly in order to reduce errors in the interpretation of correlation functions. Normalized intensity of the sample $I_n^s(Q)$ is then given by:

$$I_N(Q) = \frac{I_s^c(Q).C_R}{I_v^c(Q)/S_v(Q)} \tag{3.4}$$

where I_s^c, I_v^c are the intensities corrected for background, absorption and multiple scattering of sample and vanadium respectively; $S_v(Q)$ is the calculated self-scattering for vanadium;

38

and C_R is the ratio of composition units per unit volume of sample to vanadium.

3.4.4 Renormalization

Due to uncertainty in composition and errors in scattering lengths of the constituent atoms in the sample, the normalized intensities may not oscillate perfectly about the self-scattering level. For this reason, renormalization may be necessary. The Krogh-Moe [1956] and Norman [1957] integration method may be used in which both the self and the distinct parts are considered to be in error. Systematic errors due to background subtraction, sample density, neutron cross-sections all contribute to this uncertainty in the normalization. Thus if α and β are constants, $S(Q)$ is the Placzek-corrected self-scattering, and $I_R(Q)$ is the renormalized intensity function:

$$I_R(Q) = \alpha I(Q) - \beta S(Q) \tag{3.5}$$

One of the constant may be evaluated by assuming the other to be unity. It may be shown that when $\alpha = 1$;

$$\beta = \frac{\int_0^\infty Q^2 I(Q) dQ + 2\pi^2 \rho^\circ (\sum_j \bar{b}_j)^2}{\int_0^\infty Q^2 S(Q) dQ} \tag{3.6}$$

and when $\beta = 1$;

$$\alpha = \frac{\int_0^\infty Q^2 s(Q) dQ - 2\pi^2 \rho^\circ (\sum_j \bar{b}_j)^2}{\int_0^\infty Q^2 I(Q) dQ} \tag{3.7}$$

where ρ^0 is the average composition unit number density within the sample. Normally, the geometric mean of α and β is subsequently used to obtain $I_R(Q)$ from equation 3.5 and typically may have values of the order of a percent or less.

3.4.5 Placzek corrections

In the analysis of data, an assumption was made that the atoms do not move during the scattering process. This is referred to as the *static approximation*. This assumption has the effect of performing the integration of intensity at a constant value of Q in $\omega - Q$ space.

In first order, this approximation leads to distortions of the self-scattering level and may be removed by the method employed by Placzek [1952] who assumed $1/v$ detector law. This work was further extended to arbitrary detector efficiencies by Yarnel et al. [1973]. In the present work the latter formalism has been adopted since gas detectors follow an exponential law where the efficiency is assumed to have the form

$$\epsilon(k) = 1 - e^{-ak/k_0} \tag{3.8}$$

where a = a constant dependent on detector constant. Estimation of a for the High-Q diffractometer is detailed in Appendix A. The effective integrated cross-section measured with a detector having an energy-dependent efficiency is given by

$$\frac{d\sigma}{d\Omega}_{meas} = Nb^2 \int_{-\infty}^{\infty} \frac{|k|}{|k_0|} \epsilon(k) S(\underline{Q}, \omega) d\omega \tag{3.9}$$

where $\hbar\omega = E_i$ (incident energy).

For neutrons which have a non-negligible mass m compared to the mass M of the scattering atom, the departure of $|k/k_0|$ from unity and the variation of $\epsilon(k)$ all give rise to corrections of the order of m/M at large scattering angles [Yarnel et al. (1973)]. Considering only the first order terms in m/M, (since the mass of scattering atoms is much greater than the neutron mass) the effective differential cross sections can be written for first order recoil effects as

$$\frac{d\sigma^{coh}}{d\Omega} = b_{coh}^2 [S(Q) + P(Q)] \tag{3.10}$$

$$\frac{d\sigma^{incoh}}{d\Omega} = b_{incoh}^2 [1 + P(Q)] \tag{3.11}$$

with

$$P(Q) = \frac{m}{M} \left[\frac{k_B T}{2E_0} - \left(c_1 + c_3 \left(\frac{k_B T}{E_0} \right) \right) \frac{Q^2}{k_0^2} \right] \tag{3.12}$$

where E_0 and k_0 are the energy and wavevector of the incident neutron respectively. $k_B T$ is the mean kinetic energy of the atom. C_1 and C_3 are the detector constants depending on the detector law.

$$c_1 = 1 - \frac{ae^{-a}}{2(1 - e^{-a})} \tag{3.13}$$

40

$$c_3 = \frac{a(1+a)e^{-a}}{4(1-e^{-a})} \qquad (3.14)$$

3.5 X-ray data corrections

3.5.1 Background

The samples measured here all displayed good absorption of X-rays (1.54 Å , 0.71 Å). Data were obtained by reflection off the powdered glass samples placed in shallow depressions of glass slides. Contributions to the sample scattered intensities from these holders were negligible and a measurement of air scattering was thus considered to be the appropriate background. A direct subtraction of the latter from sample intensity was then made.

3.5.2 Absorption

For X-rays, it can be shown that, for plane samples in Bragg-Brentano reflection geometry the following expression is necessary [Milberg (1958)]:

$$A(Q) = \frac{I}{I_0} = \frac{\sin\theta}{2\mu t}[1 - e^{-2\mu t/\sin\theta}] \qquad (3.15)$$

normalized to unit volume where μ is the absorption coefficient of the sample. In this work, scattering of X-rays was considerably less than absorption and multiple scattering was thus negligible.

3.5.3 The polarization factor

The characteristic radiation from an X-ray tube is considered to be unpolarized. However such radiation, when scattered, gets polarized and is a function of scattering angle [Compton and Allison (1935)]. The polarization factor $P(\theta)$ is used to correct for the loss of intensity and is given by;

$$P(\theta) = \frac{1 + x\cos^2 2\theta}{1+y} \qquad (3.16)$$

41

where 2θ is the scattering angle, $x = cos^2 2\alpha$, α being the Bragg angle of the monochromator. In the above expression, $x = y$ when the monochromator is set in the incident beam and $y = 1$ when the monochromator is located in the diffracted beam. $x = y = 1$ when a filter is used in place of the monochromator.

3.5.4 Form factor calculation

The theoretical form factor can be calculated from the expression

$$f(\sin\theta/\lambda) = \sum_{i=1}^{4} a_i \, exp[-b_i \, \sin^2\theta/\lambda^2] + c \qquad (3.17)$$

Values of a, b and c have been tabulated [Cromer and Mann (1968)].

In the calculation of coherent scattering, the energy of the incident X-ray is assumed to be located far from the absorption edge of the constituents present in the specimen. In instances of this effect being taken into account, *anomalous dispersion* corrections are necessary. Form factor calculated considering this effect has the form

$$f_i(Q) = f_i^0(Q) + \Delta f_i'(Q) + i\Delta f_i''(Q) \qquad (3.18)$$

$$< f >^2 = (< f^0 + \Delta f' >)^2 + < \Delta f'' >^2 = [\sum_i C_i f_i(Q)]^2 \qquad (3.19)$$

$$< f^2 > = < (f^0 + \Delta f')^2 > + < (\Delta f'')^2 > = [\sum_i C_i f_i^2(Q)] \qquad (3.20)$$

where $\Delta f'$ and $\Delta f''$ are the real and imaginary additions of the anomalous dispersion term to the form factor [Cromer (1965)].

3.5.5 Correction to incoherent scattering

Some of the scattered radiation may originate from Compton scattering and has a longer wavelength. This change in the wavelength is known as the *Compton Shift* ($\Delta\lambda_c$) which increases at high angles. The incoherently scattered Compton intensity can be calculated and the analytical expressions have the form [Thijsse (1984)]

$$I_{inc}(Q) = \left(\frac{\lambda}{\lambda'}\right)^2 \sum_{j=1}^{n} \frac{C_j Z_j (b_j Q)^{a_j}}{1 + (b_j Q)^{a_j}} \qquad (3.21)$$

42

where $\lambda' = \lambda + \Delta\lambda_c$, Z_j is the atomic number of atom-type j and

$$a_j = 2.6917Z_j^{-1} + 1.245 \qquad (3.22)$$

$$b_j = 1.1870Z_j^{-1} + 0.1075 + 0.00436Z_j - (0.01543Z_j)^2 + (0.01422Z_j)^3 \qquad (3.23)$$

$I_{inc}(Q)$ is added to the calculated form factor.

3.5.6 Normalization

The intensity corrected for background, polarization and absorption $I^{cor}(Q)$ can be expressed as:

$$\alpha I^{cor}(Q) = I_{eu}^{coh} + I_{eu}^{inc}(Q) \qquad (3.24)$$

where $I_{eu}^{coh}(Q)$ and $I_{eu}^{inc}(Q)$ are the coherent and incoherent scattering intensities in electron units and α is the normalization constant given by;

$$\alpha = \frac{\int_{Q_{min}}^{Q_{max}}[< f^2 > + I_{eu}^{inc}(Q)]dQ}{\int_{Q_{min}}^{Q_{max}}[I^{cor}(Q)]dQ} \qquad (3.25)$$

A generally acceptable value of Q_{min} is $0.75Q_{max}$. This method of normalizing the intensity is referred to as the High Angle Method. The normalizing constant α depends on the chosen range $(Q_{max} - Q_{min})$ and the value of Q_{min} may in turn be chosen such that the following expression is satisfied [Wagner (1978)];

$$\int_{Q_{min}}^{Q_{max}} Q^2 I(Q)dQ = -2\pi\rho^0 \qquad (3.26)$$

3.6 FTIR and UV/Visible measurements

The energy of a molecule consists of rotational, translational, vibrational and electronic components. To a first approximation, the vibrational energy of a molecule covers the entire region of the IR spectrum. Electronic energy may be probed by the absorption or emission of ultraviolet and visible radiation. Thus it is possible to study the vibrational and electronic states of a solid with IR and UV/ Visible spectroscopy.
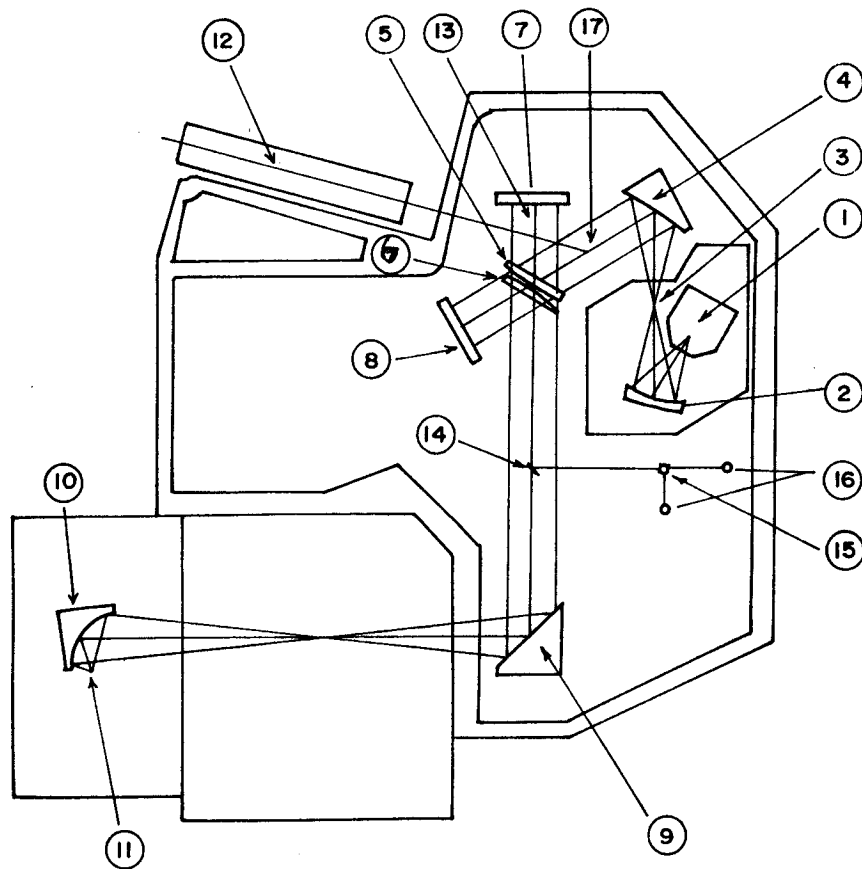
1. SOURCE
2. SPHERICAL MIRROR
3. APERTURE
4. COLLIMATOR MIRROR
5. BEAM SPLITTER
6. COMPENSATOR (Ge ON KBr)
7. FIXED MIRROR
8. MOVING MIRROR
9. PARABOLOIDAL MIRROR
10. COLLECTING MIRROR
    [OFF AXIS ELLIPSOIDAL MIRROR]
11. HIGH SENSITIVE PYROELECTRIC
    DETECTOR
12. He-Ne LASER
13. $\frac{1}{8}\lambda$ WAVELENGTH PLATE
14. He-Ne LASER HALF MIRROR
15. POLARISED BEAM SPLITTER
16. He-Ne LASER DETECTOR
17. He-Ne LASER BEAM INTRODUCING
    MIRROR

Figure 3.5: Schematic of the FTIR-8001 spectrophotometer

44
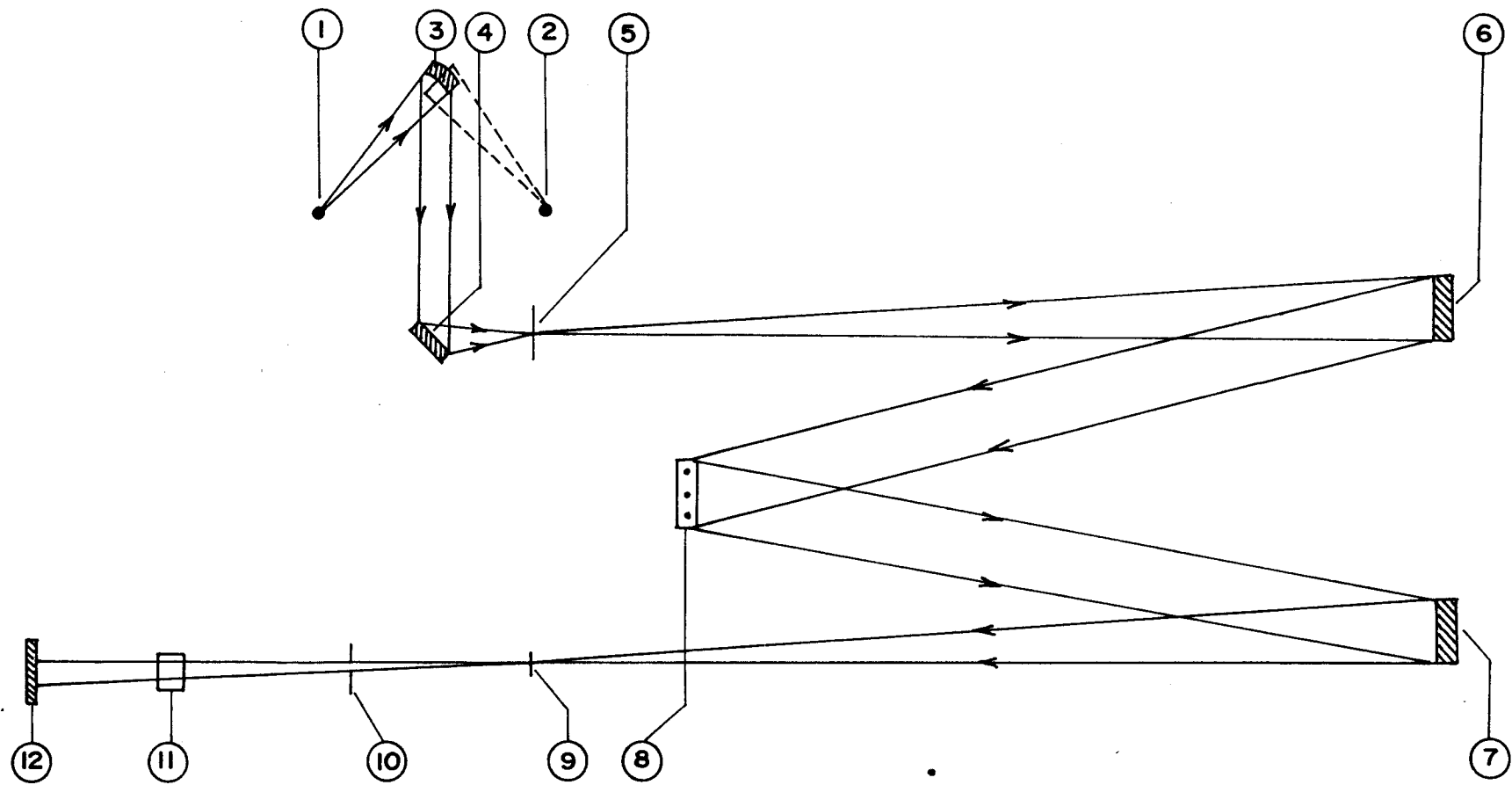
1. D2 LAMP
2. TUNGSTEN LAMP
3. SOURCE CONDENSER
4. TRANSFER MIRROR
5. ENTRANCE SLIT
6. COLLIMATOR

7. DECOLLIMATOR
8. GRATING
9. EXIT SLIT
10. FILTER
11. SAMPLE
12. PHOTOCELL

Figure 3.6: Ray Diagram of UV spectrophotometer 119

IR absorption takes place when there is a change in dipole moment associated with the vibrational mode excited. The dipole moment vector $\mathbf{M}$ is proportional to the displacement $\mathbf{u_i}$ and can be written as [Alben and Boutron (1975)]:

$$\mathbf{M} = \sum_{i(j,k)} [(\mathbf{r_{ik}} - \mathbf{r_{ij}})[(\mathbf{u_i} - \mathbf{u_j}).\mathbf{r_{ij}} - (\mathbf{u_i} - \mathbf{u_k}).\mathbf{r_{ik}}] \qquad (3.27)$$

where $\mathbf{u_i}$ are displacement vectors and $\mathbf{r_{ij}}$ is a unit vector joining sites i and j. In terms of bond compression;

$$C_{ij} = (\mathbf{u_i} - \mathbf{u_j})\mathbf{r_{ij}} \qquad (3.28)$$

$$\mathbf{M} = 2\sum_i (\sum_j C_{ij})(\sum_k \mathbf{r_{ik}}) \qquad (3.29)$$

A dipole moment arises due to an asymmetric atomic charge distribution. An induced dipole moment can be zero such as for perfect tetrahedral symmetry since $\sum_{ij} \mathbf{r_{ij}} = 0$.

IR spectroscopy measurements generally employ a grating together with a source and a detector. If the monochromator is replaced by a Michelson interferometer the measured transmitted spectrum is Fourier transformed into a frequency spectrum and the instrument is then called a Fourier Transform Infra-Red Spectrometer (FTIR). FTIR spectroscopy has the following three advantages: multiplex advantage; aperture advantage; and wavenumber precision advantage. FTIR measures a spectrum of all wavenumbers in a single scan. A spectrum with high signal-to-noise ratio can be obtained by scanning for a longer period. This is known as the multiplex advantage. A large aperture can be used on the FTIR, offering a large beam source area as in the case of a bright optical system. This helps in creating a spectrum having a high signal-to-noise ratio and is known as aperture advantage. The FTIR uses a He-Ne laser in sampling the interferogram. The use of monochromatic light helps in obtaining a spectrum with a high wavenumber accuracy.

The schematic of the IR spectrophotometer is shown in Fig.3.5 . The instrument uses black coated heated wire as the source of infra-red radiation. A KBr plate coated with Ge is used as a beam splitter. The transmitted radiation is measured by a high sensitivity

pyroelectric detector in the range 4600 cm^{-1} to 400 cm^{-1}. In the measurements reported here, the powdered glass samples were mixed with KBr and pelletised under 9 tons pressure.

UV/Visible absorption spectra of rare-earth glasses were studied using a standard spectrophotometer (Fig.3.6). The instrument covers a range of 200 to 1000 nm and uses a tungsten-halogen lamp for the visible range (i.e. 340 to 1000 nm) while a deuterium lamp is used as a source of UV light (200 to 340 nm). The transmitted beam is detected by a solid state silicon detector.

3.7 A.C. susceptibility measurements

The magnetization **M** of a material is a linear function of the applied magnetic field **H**.

$$\mathbf{M} = \chi \mathbf{H} \tag{3.30}$$

where χ is the magnetic susceptibility of the material. Paramagnetic substances have $\chi > 0$ while dimagnetic substances have $\chi < 0$. For an oscillating applied field, the magnetization of the substance is given by

$$\mathbf{M} = \chi' \mathbf{H}_1 \cos \omega t + \chi'' \mathbf{H}_1 \sin \omega t \tag{3.31}$$

where $\chi = \chi' + i\chi''$.

The experimental arrangement used for the measurements is shown in Fig. 3.7. The signal generator sends a low frequency A.C. current in the primary coil. The A.C. magnetic field produced by the primary induces a voltage in the secondary coil. The secondary consists of two coils of super enamelled Cu wire which are connected in series and wound in opposite direction. The number of turns are such that the induced EMF of each is nullified by the other. A third winding connected across a potentiometer detects a variable voltage of either polarity. In the ideal case, the windings are balanced and the induced voltage is zero in the absence of the sample. In practice, however. some offset voltage is always present but is subtracted from the sample voltage. When the sample is introduced, a net EMF is induced

in the coil which is proportional to the magnetic moment of the sample. In this study, the sample temperature was varied continuously from liquid nitrogen ($\approx$ 80 K) to room temperature with a heating coil arrangement.

3.7.1 Signal calculation

When the sample of susceptibility χ is placed in the secondary coil, the voltage E produced in the secondary is;

$$E = N_s A_s \mu_0 \chi (dH/dt) \tag{3.32}$$

where **H** is the magnetic field, due to the flow of A.C. current in the primary coil. A_s and N_s are the area and number of turns respectively of the secondary coil μ_0 is the permeability of vacuum. Thus,

$$E = N_s A_s \mu_0 \frac{dM}{dt} = N_s A_s \mu_0 (2\pi f) M \tag{3.33}$$

where M is the r.m.s. of the time varying intensity of the sample magnetization. If m is the r.m.s. amplitude of sample moment; $m = MV$ where V - volume of the coil.

Voltage may then be written as

$$E = N_s A_s \mu_0 (2\pi f)(m/V) = N_s \mu_0 (2\pi f)(m/l_s) \tag{3.34}$$

where L_s is the length of the secondary.

3.8 Compositional analysis of rare-earth phosphates

3.8.1 Phosphorus determination by volumetric analysis

Each sample powder was fused using a mixture of $KClO_3$ and Na_2O_2 and was subsequently dissolved in HCl to form a 100 ml solution. Ten c.c. of this solution was then treated with ammonium molybdate to obtain an ammonium phosphomolybdate precipitate. The

latter was subsequently dissolved in NaOH forming sodium phosphate. Excess NaOH was then titrated against HCl to obtain the concentration of phosphorus in the solution (Table 3.2).

$$(NH_4)_3[PO_4, 12MoO_3] + 26NaOH \rightarrow 12Na_2MoO_4 + Na_2HPO_4 + 3NH_3 \uparrow +14H_2O \quad (3.35)$$

These values of phosphorus concentration were used to deduce the rare-earth concentrations in each sample.

3.8.2 Concentrations of rare-earths by Neutron Activation Analysis

A part of the solution (50 ml) prepared for the above mentioned volumetric analysis of each glass was added to 0.1 N oxalic acid. As a result, rare-earth oxalates precipitated out of the solution. The precipitate was dried at 600 °C for two hours and weighed. The concentrations of rare-earths so obtained were at variance with those deduced from the volumetric method. In order to resolve the difference, Neutron Activation Analysis (NAA) was applied as follows.

Nitric acid was added to the above mentioned dried precipitate to obtain rare-earth nitrates. These were diluted with water a hundred fold (for the NAA) and dried. The powder residues from $50\mu l$ volumes were sealed in polyethylene pouches which were held in small plastic bottles. These were held in the core of Apsara Reactor, B.A.R.C. for irradiation together with standard samples for periods varying from a few minutes to two hours.

The principle of this technique is to measure the yield of a particular radionuclide in a radioactive decay chain initiated by neutron absorption. The decay of the nuclide from excited to ground state is accompanied by gamma emission whose energy and relative emission rate is measured by a gamma-ray spectrometer. The main components of a Ge(Li) detector are; pre-amplifier, multichannel analyser and computer. Each gamma photopeak relates to a particular radionuclide and is compared to the same peak from a standard of

known weight. The relative peak areas are proportional to the relative weights. From this ratio, the concentration of the particular radionuclide may be found.

The full area of a gamma photopeak as measured by the Covell method [Covell (1959)] (trapezoidal area under the peak regarded as background) is directly proportional to the concentration of the radionuclide and is given by;

$$c_e = \frac{m_e \times \theta \times N}{A} f\sigma(1 - e^{-\lambda t_i})e^{-\lambda t_{ce}}\epsilon\Omega\gamma \tag{3.36}$$

where

$m_e =$ mass of the element present in the sample

$\theta =$ fractional abundance of the isotope giving rise to the product

$N =$ Avogadro number

$A =$ atomic weight of the element

$f =$ neutron flux

$\sigma =$ cross section of activation

$\lambda =$ decay constant of the product nuclide and is equal to

         $0.693/t_{1/2}$ where $t_{1/2}$ is the half life

$t_i =$ duration of irradiation

$t_{ce} =$ time elapsed between counting and end of irradiation for

         the element in the sample

$\epsilon =$ full energy peak efficiency of the detector for that energy

$\Omega =$ solid angle subtended by the sample at the counter

$\gamma =$ fractional abundance of a particular gamma ray in the decay

         of the product

Estimation of concentration with these various parameters may lead to errors. To overcome this, a standard of known mass is irradiated together with the sample. The amount of the element present in the sample can thus be calculated by comparing the counts of both the sample and the standard. Thus for the standard, equation (3.36) has the form

$$c_s = \frac{m_s \times \theta \times N}{A} f\sigma(1 - e^{-\lambda t_i})e^{-\lambda t_{cs}}\epsilon\Omega\gamma \tag{3.37}$$

where t_{cs} is the time between the end of irradiation and counting for the particular element in the standard. Thus,

$$\text{Concentration of element in p.p.m.} = \frac{m_e c_s \, e^{-\lambda t_{ce}}}{m_s \ e^{-\lambda t_{cs}}} \qquad (3.38)$$

where m_s is in μgs and m_e is in gms.

The results are compared in Table 3.3. In order to recheck the results, powdered samples were also irradiated in the thermal column of the reactor. Concentrations of rare-earths obtained were found to be higher than expected. Thus values upto 25% higher from thermal column data and from 4.5 to 17% higher from core irradiation data were found. These differences between thermal column and core irradiation data are likely to have resulted on account of differences in neutron spectra between the two locations of irradiation. The concentrations of P_2O_5 were obtained using volumetric analyses and were found to be consistent (within error) with the values deduced from the NAA data from in-core irradiation. These discrepancies in the percentage concentrations of P_2O_5 are likely to be due to volatilization losses of P_2O_5 during glass preparation. Dysprosium concentrations obtained from the NAA of thermal column irradiations are shown in Table 3.4.

3.9   Density Measurements

The densities of the glass samples were measured at room temperature using Archimedes principle. Distilled water was used as the buoyant liquid. The samples were weighed in air and in water with an accuracy of $\pm$ 0.0025 gms. The density was calculated using the expression:

$$\rho_s = \frac{W_s}{(W_s - W_d)}\rho_w \qquad (3.39)$$

where ρ_s is the sample density, ρ_w is the density of distilled water at room temperature. W_s is the weight of sample in air and ($W_s - W_d$) is the difference in weight of the sample in air and weight of displaced water. Densities of waste glasses and rare-earth phosphate glasses are tabulated in Table 3.5 and Table 3.6

51

1 - GLASS CRYOSTAT
2 - PRIMARY COIL
3 - SECONDARY COILS
4 - SAMPLE
5 - WOODEN STAND
6 - SOURCE
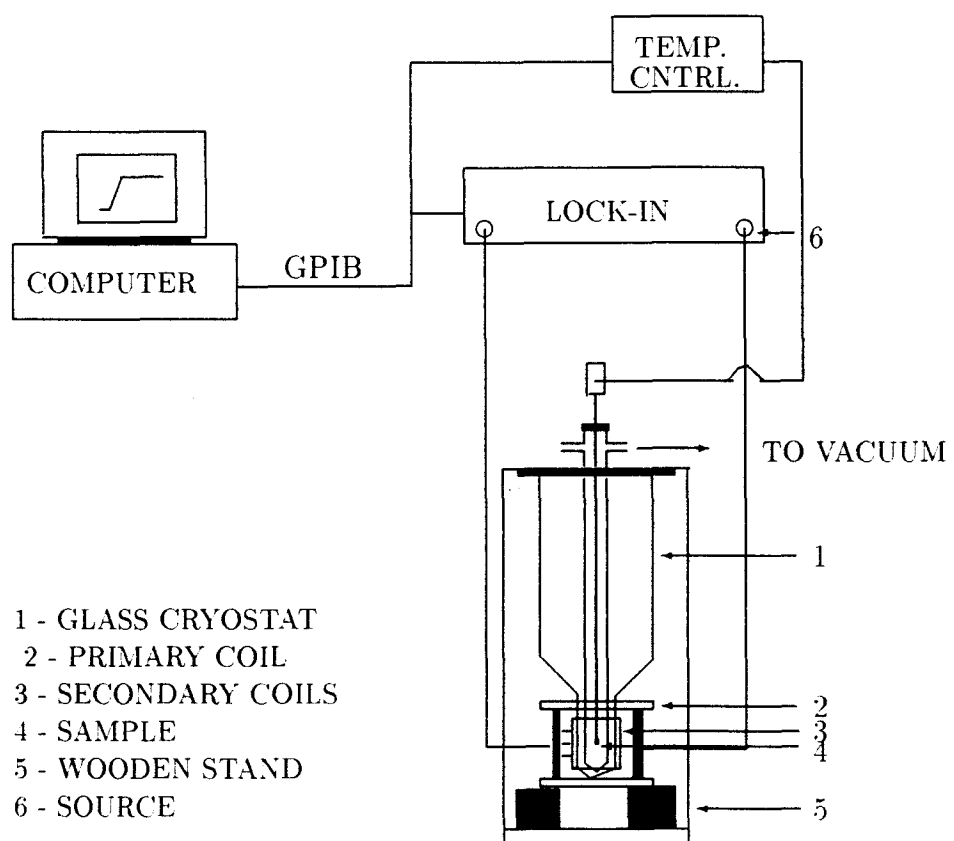
Figure 3.7: Setup of A.C susceptibility measurements

Table 3.2: Concentration of phosphorus in the sample (using volumetric analysis)

Sample	Moles%		
	P_2O_5	R_2O_3	R_2O_3
20SmP	78	22 (Sm_2O_3)	–
25SmP	74	26 (Sm_2O_3)	–
Dy-P	74.4	25.6 (Dy_2O_3)	–
La-Dy-P	76.7	5.88 (La_2O_3)	17.42 (Dy_2O_3)

Table 3.3: Rare earth concentrations from NAA using precipitates of gravimetric analysis

Sample	Wt. of rare earth using NAA (mg/ml)	Wt. of sample used for NAA (mg/ml)	Rare earth p.p.mg (NAA)	Expected p.p.mg (st. mix.)
20SMP	SM- 0.8345	2.426	343.9	328.1
25SMP	SM- 1.115	2.454	454.3	388.2
20DYP	DY- 1.0392	2.548	407.8	345
20LADYP	DY- 0.6297	2.38	264.5	262.6
20LADYP	LA- 0.0696	2.38	029.2	071.4

Table 3.4: Dy concentrations from NAA irradiation in thermal column

Sample		Wt. of sample (mg)	Dy (mg) in sample	Dy p.p.mg (NAA)	Mean (A.B)p.p.mg	Expected p.p.mg
20LADYP	A	22.3	7.9174	355	327	262.5
	B	22.5	6.73	299.1		
20DYP	A	22.9	9.6897	423.1	422	345
	B	24.5	10.313	420.9		

Table 3.5: Densities of some waste glasses.

Sample	density (gm/cc)
WTR46	2.949 ±0.017
WTR4	2.844 ± 0.012
WTR12	2.765 ± 0.021
WTR13	2.845 ± 0.016
WTR14	2.576 ± 0.013
WTR15	2.702 ± 0.014
WTR62	3.016 ± 0.008
WTR22	3.648 ± 0.024
WTR30	3.609 ± 0.034
WTR35	3.758 ± 0.026
Basic Glass	2.462 ± 0.009

Table 3.6: Physical properties of rare-earth phosphate glasses

	Density (gms/cc)	Visual appearence
La-P	3.102 ± 0.01	Colourless
La-Ce-P	3.199 ± 0.009	Pale yellow to colourless
La-Pr-P	2.999 ± 0.008	Green
La-Nd-P	3.284 ± 0.011	Violet
La-Eu-P	3.397 ± 0.011	Pale peach
La-Tb-P	3.494 ± 0.008	Colourless
La-Ho-P	3.777 ± 0.012	Golden Yellow
La-Er-P	3.844 ± 0.01	Pink
20SmP	3.757 ± 0.009	Yellow
25smP	3.85 ± 0.011	Yellow
DyP	3.62 ± 0.01	Pale Green
LaDyP	2.53 ± 0.002	Colourless

Chapter 4

NUCLEAR-WASTE GLASSES

A widely accepted technique for the immobilization of high-level liquid radioactive waste produced during the reprocessing of spent nuclear fuel is vitrification. This method of storing nuclear waste is about 40 years old. Studies in this field have continued in many different countries. In this method, the waste products are stored for about a year to allow the short lived radioactive atoms to decrease in activity and lose much of their potential for secondary ionization. The reprocessing of spent fuel to recover unused fissile isotopes involves the separation of fission products in the form of aqueous nitrates. These are converted to oxides in the form of dry powders. After the addition of glass-forming oxides such as boro-silicates, phosphates, the mixture is melted, quenched and cast into stainless steel containers which are welded and sealed. Such canisters are then transferred after some length of time to storage locations. The latter are preferably deep shafts in stable geological structures and in some cases these might be located in disused mines. The success of this vitrification programme is dependent on both the mechanical and chemical stability of these glasses. Such properties ultimately derive from the microscopic structures. Thus diffraction measurements to investigate these structures were made on the basic boro-silicate host glass as well as simulated (non-radioactive) vitrified waste.

4.1 Structural review

The structures of silica-based glasses are such that they can accommodate various waste constituents. However, as silica has a high melting point, B_2O_3 is often added in order to lower the temperature of melting. The major threat to the safe long-term storage arises from action of water. Thus a particular glass is considered acceptable if its leaching characteristics are considered to be good. Several leaching studies have already been made [Pederson et al. (1981), McVay and Buckwalter (1980), Ebert et al. (1991)]. The successful vitrification of these waste oxides requires that the included waste bonds with the host matrix without causing devitrification. In this respect, the structural study of such systems becomes important for the understanding of their physical and chemical properties e.g. its long term chemical stability and inertness. The techniques of X-ray diffraction and neutron diffraction were therefore applied to the host boro-silicate glass without waste, and to the nuclear-waste glass in order to examine the change in the structure of the host matrix after the inclusion of nuclear waste. The most important feature to determine is the change in the basic structural unit of the nuclear-waste glass with respect to the basic glass.

Vitreous SiO_2 and B_2O_3 have each been well studied [Mozzi and Warren (1969), Wright and Sinclair (1978), Johnson et al. (1979)]. These authors propose that the structure is a random network model of SiO_4 tetrahedra for $v - SiO_2$ and a mixture of BO_3 triangles and B_2O_6 boroxol rings in the case of $v - B_2O_3$.

The results of NMR investigations have shown that when R (= mole % Na_2O/ mole % of B_2O_3) is less than 0.5, the additional oxygen atoms introduced with the Na_2O are used entirely to convert BO_3 units to BO_4 units in sodium boro-silicate glass. Yun and Bray [1978] postulated that for $0.5 < R < R_{max}$, the added Na_2O is used solely to convert diborate groups to $(BSi_4O_{10})^-$ units.

A neutron diffraction study of borate glasses doped with Ag, Na and Li [Swenson et al. (1995)] reveals two different B-O nearest neighbour distances, 1.37 Å and 1.47 Å . They attribute these distances to BO_3 and BO_4 groups. From these measurements, they were able

to calculate the fraction of BO_4 units.

In sodium aluminosilicate glasses it is thought that when the Al/Na ratio is significantly less than unity, each Al^{3+} ion substitutes for a Si^{4+} ion in the network and two non-bridging ions are eliminated. The Al^{3+} ion and a nearby Na^+ ion are together electrostatically equivalent to an Si^{4+} ion maintaining local charge balance. Day and Rindone [1962] proposed that when the Al/Na ratio is more than unity the Al^{3+} will be six-coordinated by oxygen and act as network modifiers. However, Smets and Lommen [1981] used XPS to investigate glasses where the Al/Na ratio is less than 1 and proposed that some Al^{3+} ions are probably incorporated as $(AlO_6)^{3-}$ octahedra.

A Small Angle Neutron Scattering study of a nuclear waste containing boro-silicate glass [Sinclair et al. (1983)] revealed that there are regions with average radius of gyration 121 Å in the matrix. The authors have suggested that these regions could be inhomogeneities in the glass matrix formed by clustering of modifier atoms.

4.2   Sample preparation and Experimental method

The simulated nuclear-waste glass samples were prepared and supplied by the Process Engineering and Systems Development Division, B.A.R.C., Mumbai. In the preparation of waste glasses [Vaswani and Jahagirdar (1986)], the method used was the same for all the samples studied here. Solutions of $NaNO_3$ were prepared containing simulated waste inclusive of corrosion compounds and fission products of unreacted heavy metals such as uranium, cerium etc. The glass forming host matrix consisting of dry powders of B_2O_3, SiO_2, Na_2O etc. was mixed together with the dry residue from the waste solution. The mixture was introduced in a furnace at $800°C$ and the temperature was increased to $1100°C$ in steps of $50°C$ every two hours. Typical pouring temperatures were about $1050°C$. Homogeneity tests by these authors included optical microscopy (SEM) and X-ray diffraction. Apart from this, the suitability of the sample for long term storage was tested by leaching studies.

Table 4.1: Composition of Waste Oxides included in nuclear-waste glass

Waste oxide	UO_2	Na_2O	MoO_3	Fe_2O_3	SO_4	SrO	Cs_2O	NiO	CeO_2	CrO
Wt%	54%	29%	3.5%	6.3%	4.8%	◄——— 2.4% ———►				

Samples were kept in boiling water for a week and the resultant weight loss was measured. Those having the least leaching rate (a few micrograms in a week) were considered to be acceptable candidates as storage glasses. Compositions of the samples studied are shown in Table 4.1 and 4.2. For the discussion, hereafter, the basic boro-silicate glass will be referred to as basic glass and the waste glasses will be termed 'WTR'. Various samples were studied, out of which WTR46 and WTR62 were found to be vitreous. The other samples were found to be partially crystalline (Fig. 4.1). From leaching rate measurements, the sample WTR62 was considered 'acceptable' [Jahagirdar (1992)]. Three additional samples with waste loadings straddling that of WTR62 (i.e. WTR30, WTR35 and WTR22) were also studied to check for a possible correlation between structural features and a property such as leaching rate.

Neutron diffraction measurements were made with the High-Q diffractometer (discussed in chapter 3) in transmission geometry with a wavelength of 1.27 Å ($Q_{max} = 8.7$ Å^{-1}) for WTR46 and boro-silicate glass whereas WTR62, WTR22, WTR30 and WTR35 were measured with 0.783 Å ($Q_{max}=14$ Å^{-1}). The presence of ^{10}B in the sample made the experiments difficult (due to the high absorption cross-section of ^{10}B) resulting in a relatively low signal-to-noise ratio of the data. X-ray measurements were made on waste glasses with $\lambda = 1.54$ Å on a rotating anode Rigaku X-ray diffractometer. Normal data reduction procedures were applied (Chapter 3).

Table 4.2: Compositions (in wt%) of the waste glasses

Sample	WO	SiO_2	B_2O_3	Na_2O	Others	CFL (gms/3 days)
WTR46	25	40	10	10	$5(Al_2O_3)$, $5(TiO_2)$, $5(BaO)$	0.0018
WTR4	25	30	15	10	$20(CaO)$	–
WTR12	30	30	15	10	$15(CaO)$	0.0605
WTR13	30	30	15	10	$15(MgO)$	0.2712
WTR14	30	30	15	10	$15(MnO)$	0.1933
WTR15	30	30	15	10	$15(BaO)$	0.2712
WTR62	25	30	10	–	$25(PbO)$, $10(Fe_2O_3)$	0.0004
WTR22	22.5	31	10.3	–	$25.8(PbO)$, $10.3(Fe_2O_3)$	–
WTR30	30	28	9.3	–	$23.3(PbO)$, $9.3(Fe_2O_3)$	–
WTR35	35	26	8.7	–	$21.7(PbO)$, $8.7(Fe_2O_3)$	–
Basic Glass	–	53.3	13.3	13.3	$6.7(Al_2O_3)$, $6.7(TiO_2)$, $6.7(BaO)$	–

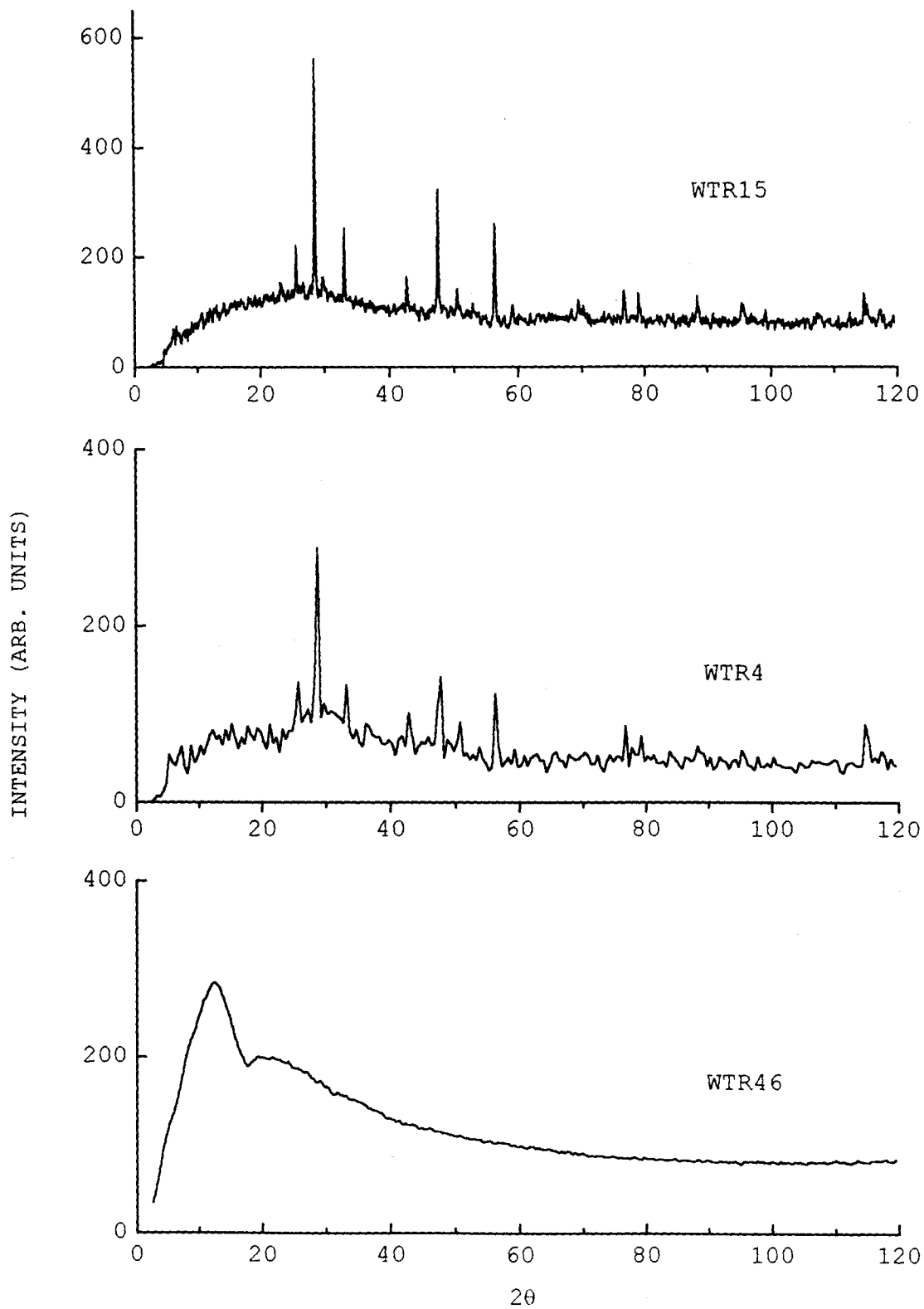*CFL – Cumulative fraction leached on weight loss basis (gms/ 3 days)

WO – Waste Oxide

Figure 4.1: X-ray diffraction pattern of WTR4, WTR15 and WTR46
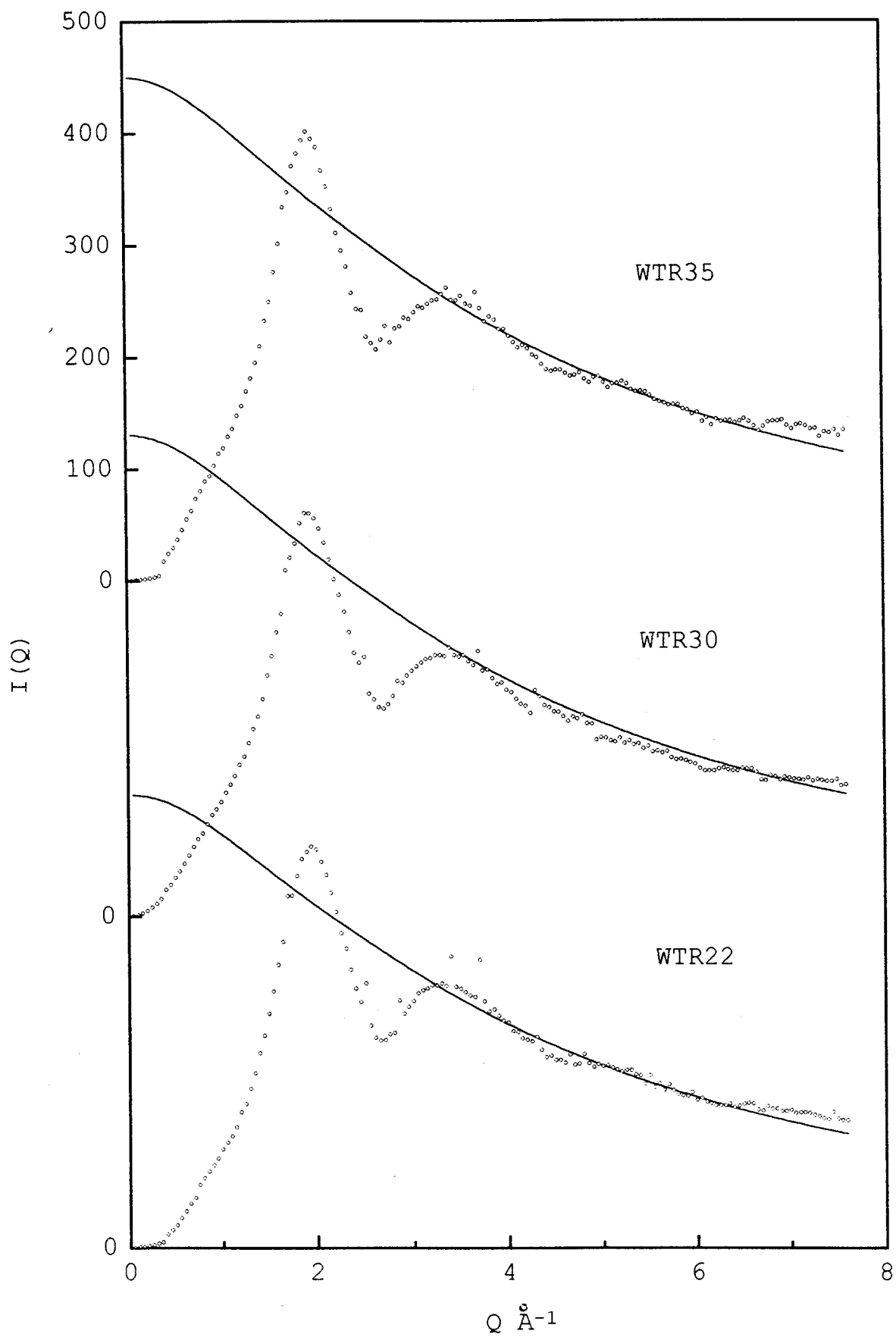
Figure 4.2: $I(Q)$ of WTR22, WTR30 and WTR35 obtained using X-rays
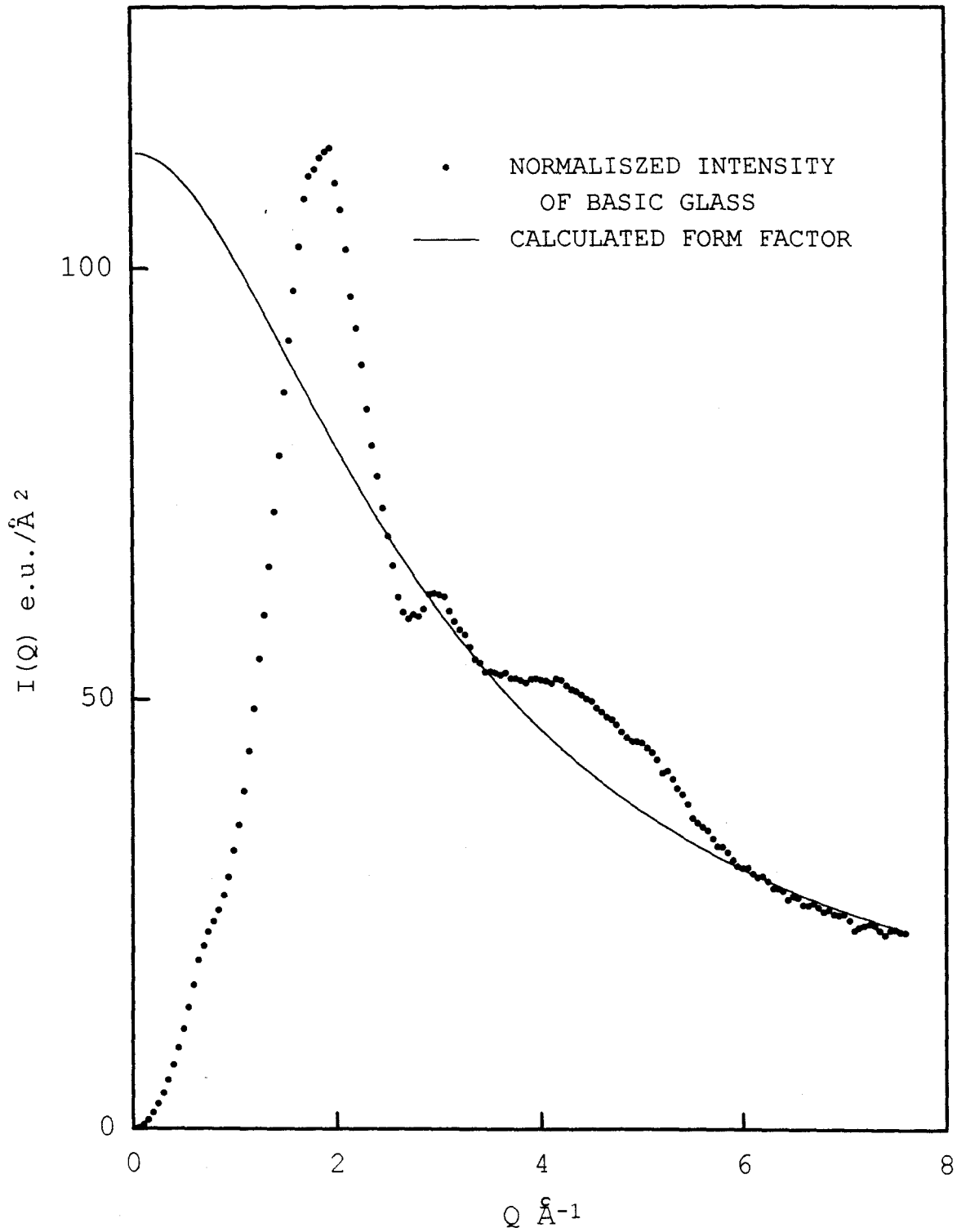
Figure 4.3: $I(Q)$ of Basic glass obtained using X-rays
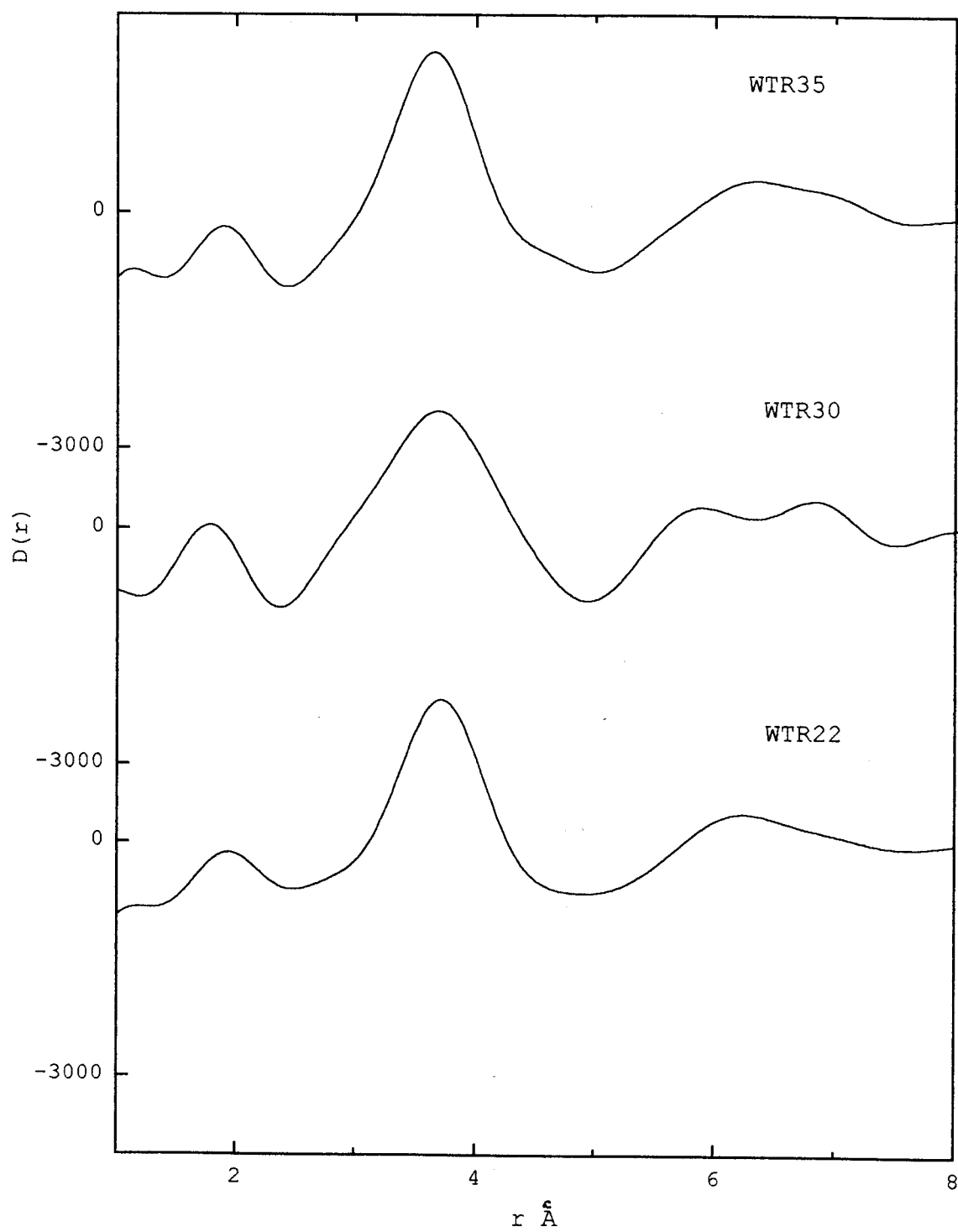
Figure 4.4: $D(r)$ WTR22, WTR30 and WTR35 obtained using X-rays

4.3 Results and Discussion

X-ray raw intensities of some devitrified samples are compared with the vitreous samples in Fig.4.1. The functions $I(Q)$ of WTR22, WTR30, WTR35 and the basic glass are compared in Figs. 4.2 and 4.3. On account of uncertainties in the detailed compositions of these glasses (caused by vaporization losses of B_2O_3 during preparation) errors in the normalization (due to low Q_{max} nature of the data), the resultant differential correlation functions from these measurements are to be interpreted with caution. The X-ray $D(r)$'s shown in Fig. 4.4 have a first peak at 1.94 Å and a second peak at 3.69 Å in the nuclear-waste glass.

Figures 4.5 and 4.6 show the neutron intensity functions of these glasses. The total correlation function $T(r)$ of WTR46 shows a peak at 1.55 Å due to the Si-O and B-O correlations and at 2.64 Å mainly due to the nearest neighbour O-O correlations together with the other correlations which are very similar to the peaks at 1.56 Å and 2.64 Å observed in boro-silicate glass (Fig. 4.8). The first maxima for the basic and the waste glass were each fitted to two Gaussian functions representing the B-O and Si-O correlations (whose approximate positions and areas were obtained from Wright and Sinclair [1978], Johnson et al. [1979] (Fig. 4.9)). These are summarized in in Table 4.3. From this it may be concluded that the structure of the basic glass may be considered to be made up of cation-centered units (SiO_4 tetrahedra and BO_3 triangles) each separated by an average cation-cation distance forming a continuous but open random network of these units. The waste cations occupy 'holes' in the network and act as network modifiers. The nearest neighbour correlations are not resolved because of poor real space resolution due to a low value of Q_{max} (8.7 Å^{-1}). The large number of constituents present in the waste glass results in a multitude of component correlations. Some of the latter may be separated out using high resolution diffraction data collected to high values of Q_{max}. Nevertheless, the diffraction data reported here confirm that the basic structure is that of a boro-silicate network formed of SiO_4 tetrahedra and BO_3 triangles. The present data also show that the correlations pertaining to these units do not change in position (in r-space) in going from the basic to the waste glass. Thus, from these

results it may be concluded that 25 wt% of waste oxide does not alter the short-range order of the basic boro-silicate network.

Identification of other features in T(r) is difficult on account of its complex nature. The second peak in T(r) of these glasses results from the O-O correlations in the SiO_4 tetrahedra and BO_3 triangles as well as the modifier atom-oxygen correlations. An attempt has been made to fit this feature from the previous knowledge of the correlations of these modifiers in either the silicate or the borate glass (Fig. 4.10 and Fig. 4.11). The component correlations of this second peak in r are based on assumptions of their positions and areas and may thus be regarded as non-unique but possible fits to the data. The schematic 2-D model of a nuclear-waste glass is shown in Fig 4.12. This representation was drawn from a projection onto a plane of a 62 atom hand-built model that maintained average inter-tetrahedral bond angles in the range 135° to 170° and valency constraints. Also, the Si-O-B was kept in the range 140° to 170°.

4.4   Conclusions

Diffraction measurements were made to investigate the structure of a boro-silicate network containing 25 wt% simulated nuclear waste oxides. The method of RDF was used for this study. The results of these measurements were compared to those of the host network to find the change in the host network after the inclusion of nuclear waste. The total correlation functions of these glasses showed a first maximum corresponding to unresolved B-O and Si-O correlations. Nearest neighbour coordination numbers obtained from Gaussian fits centred at an average distance 1.36 Å for B-O and 1.62 Å for Si-O indicated the presence of BO_3 triangles and SiO_4 tetrahedra as the basic units of the network.The waste cations occupy 'holes' and act as modifiers of the continuous random network. A detailed study of the other features in the total correlation function is difficult on account of the large number of overlapping component correlations arising from the multicomponent nature of the samples.
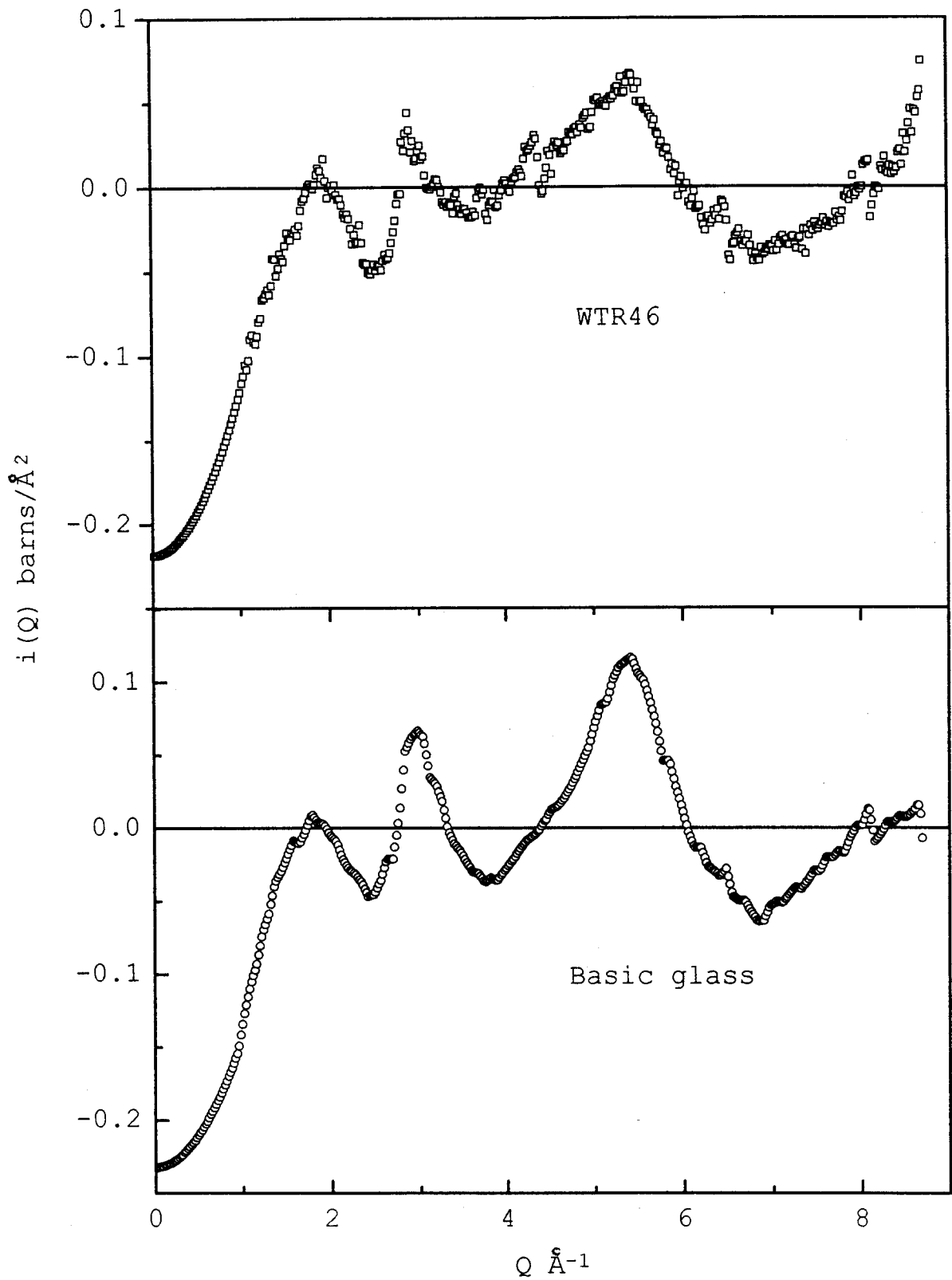
Figure 4.5: $i(Q)$ of WTR46 and the Basic glass obtained using neutrons (neutron data)
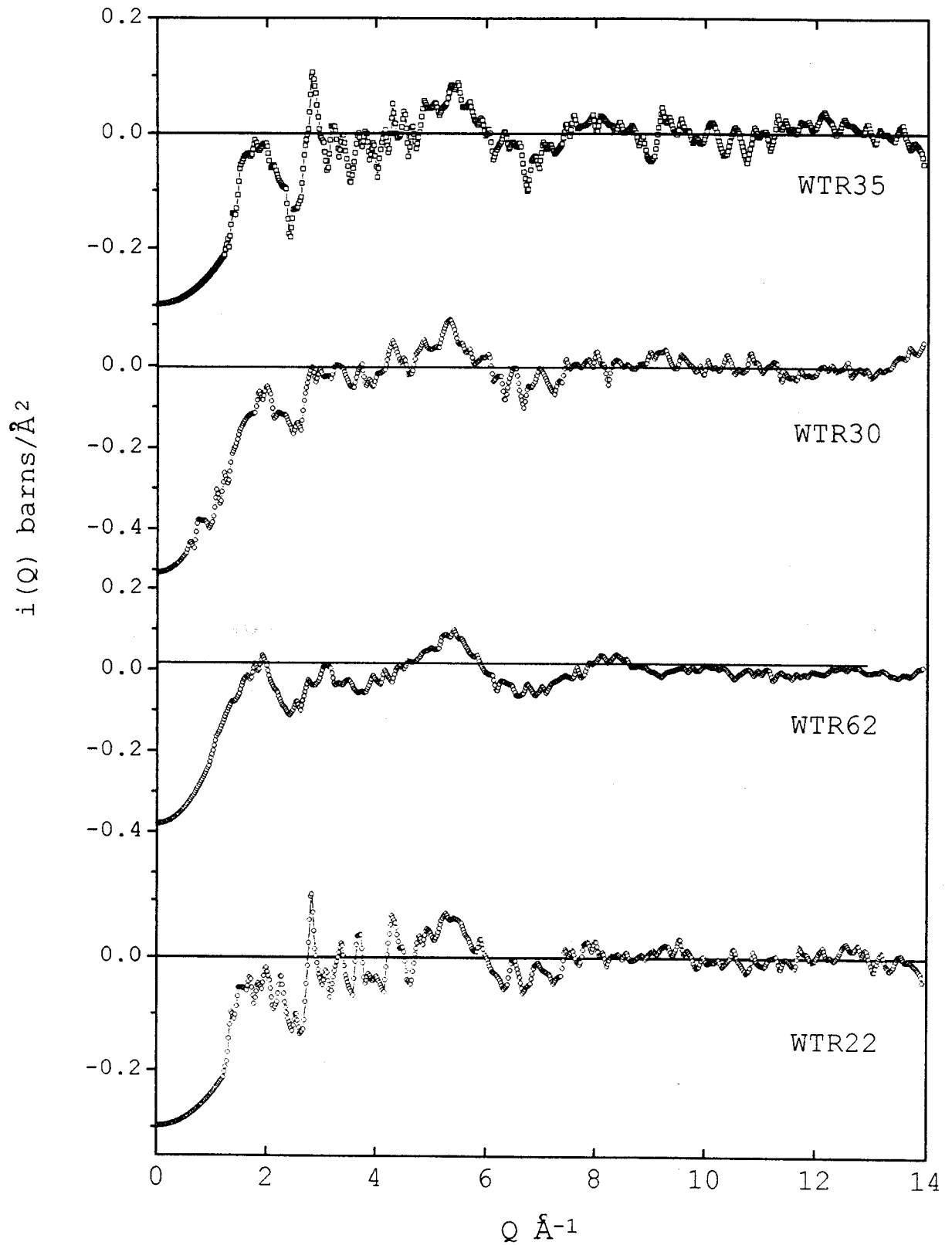
Figure 4.6: $i(Q)$ of WTR22, WTR30, WTR35 and WTR62 glass obtained using neutrons
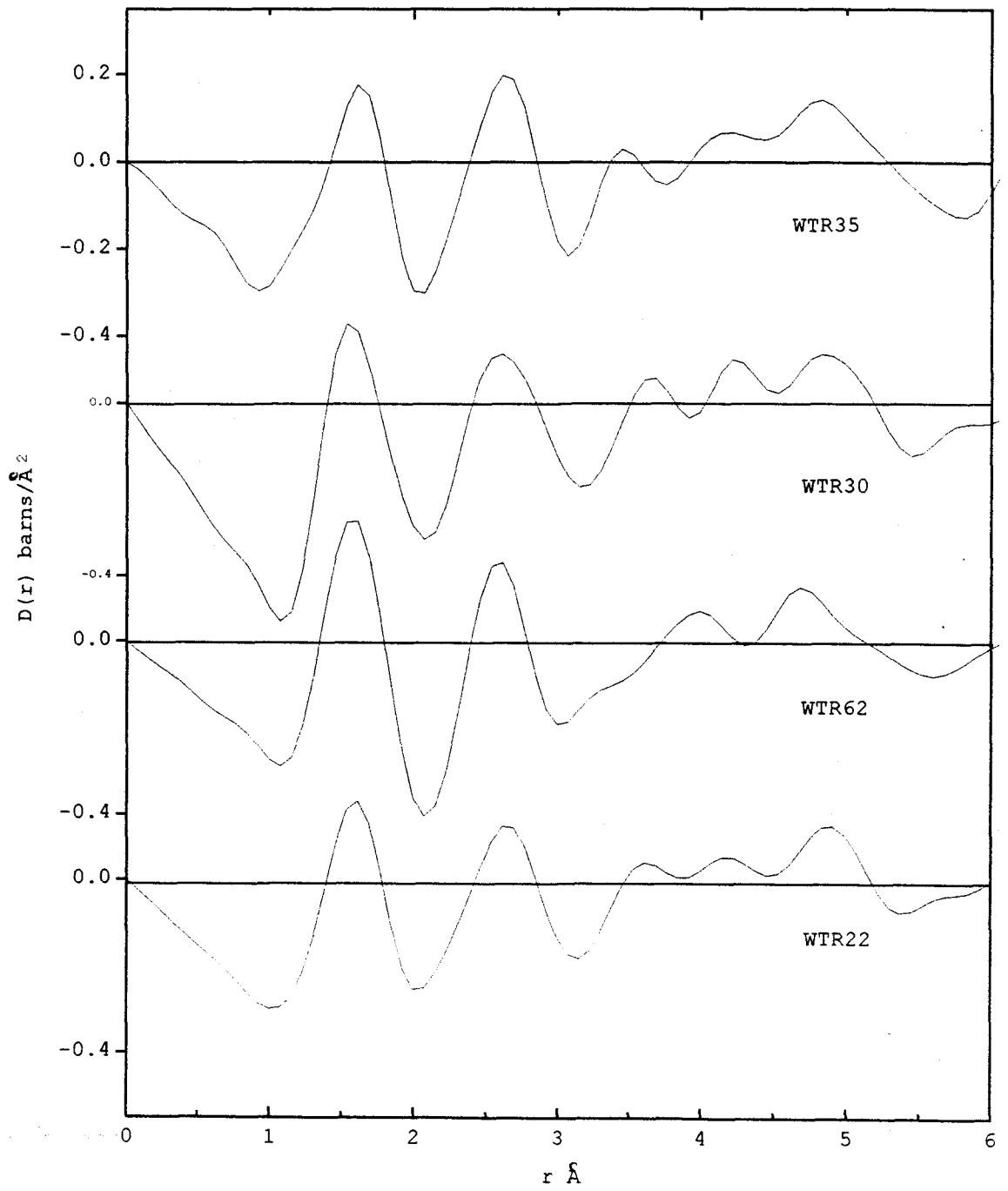
Figure 4.7: $D(r)$ of WTR62, WTR22, WTR30 and WTR35 glasses (neutron data)
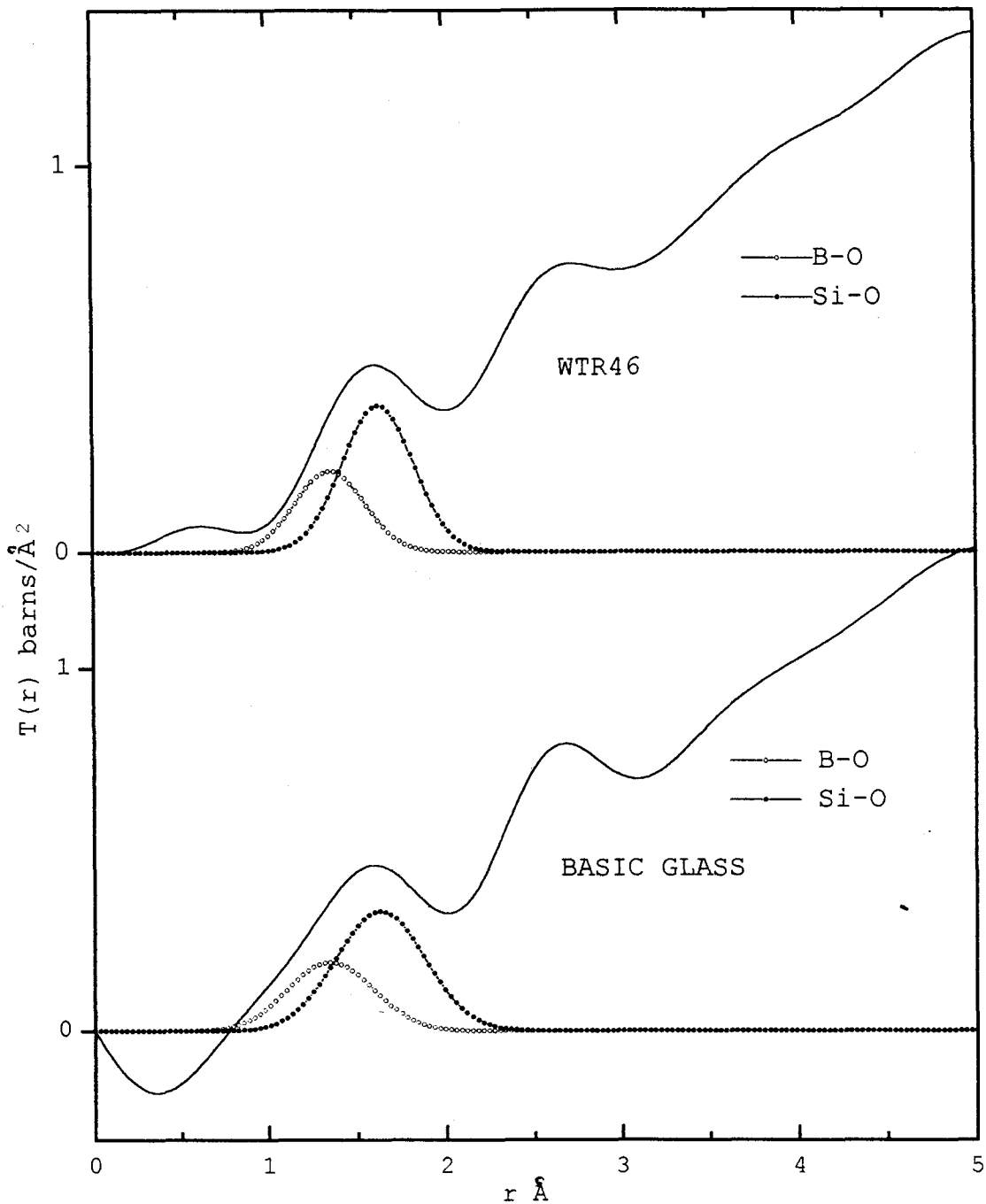
Figure 4.8: Fit to the basic glass and WTR46 glass (neutron data)

71
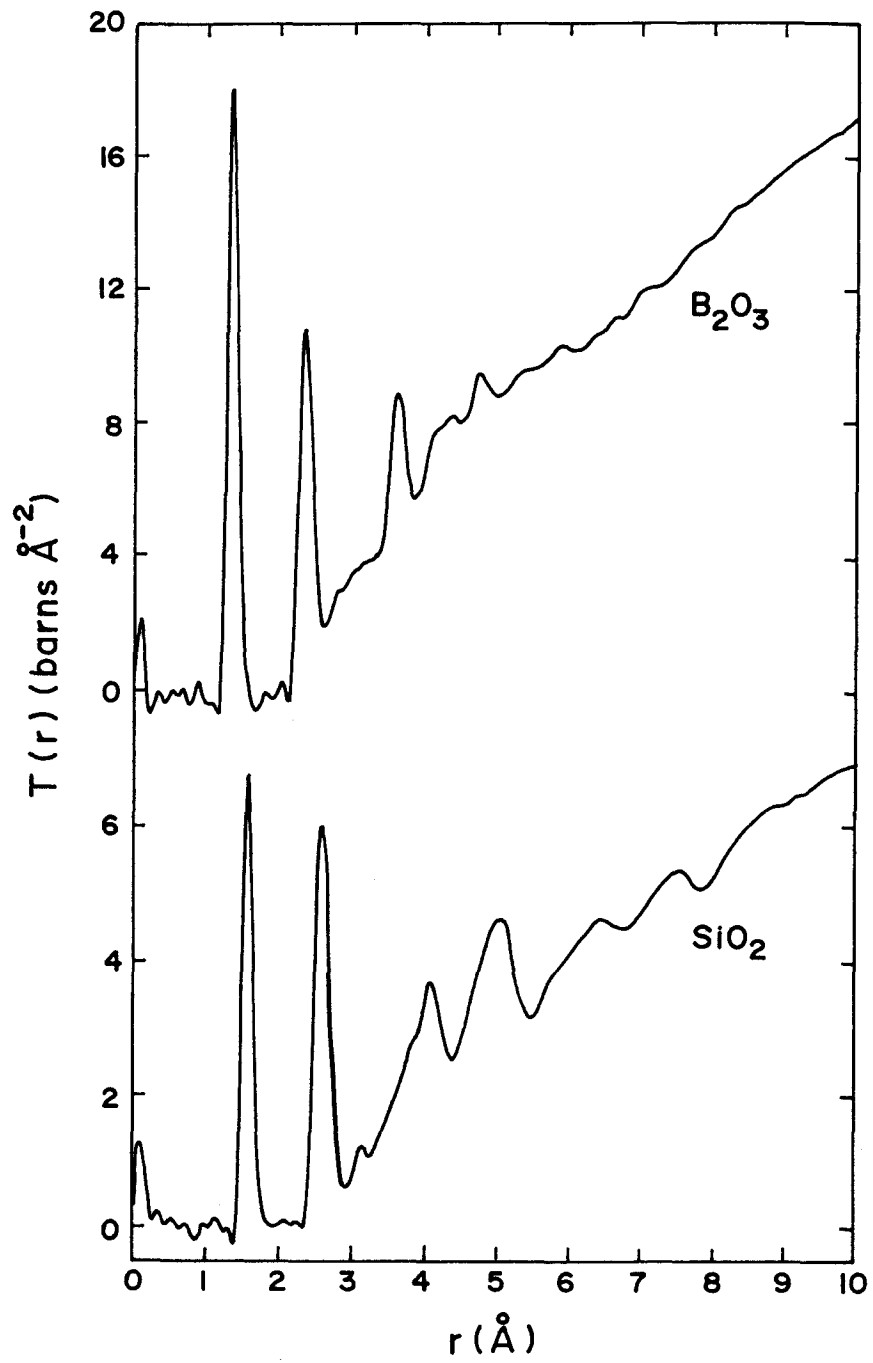
Figure 4.9: Comparison of total correlation functions of vitreous B_2O_3 (after Johnson, Wright and Sinclair [1979]) and Silica (after Wright and Sinclair [1978])
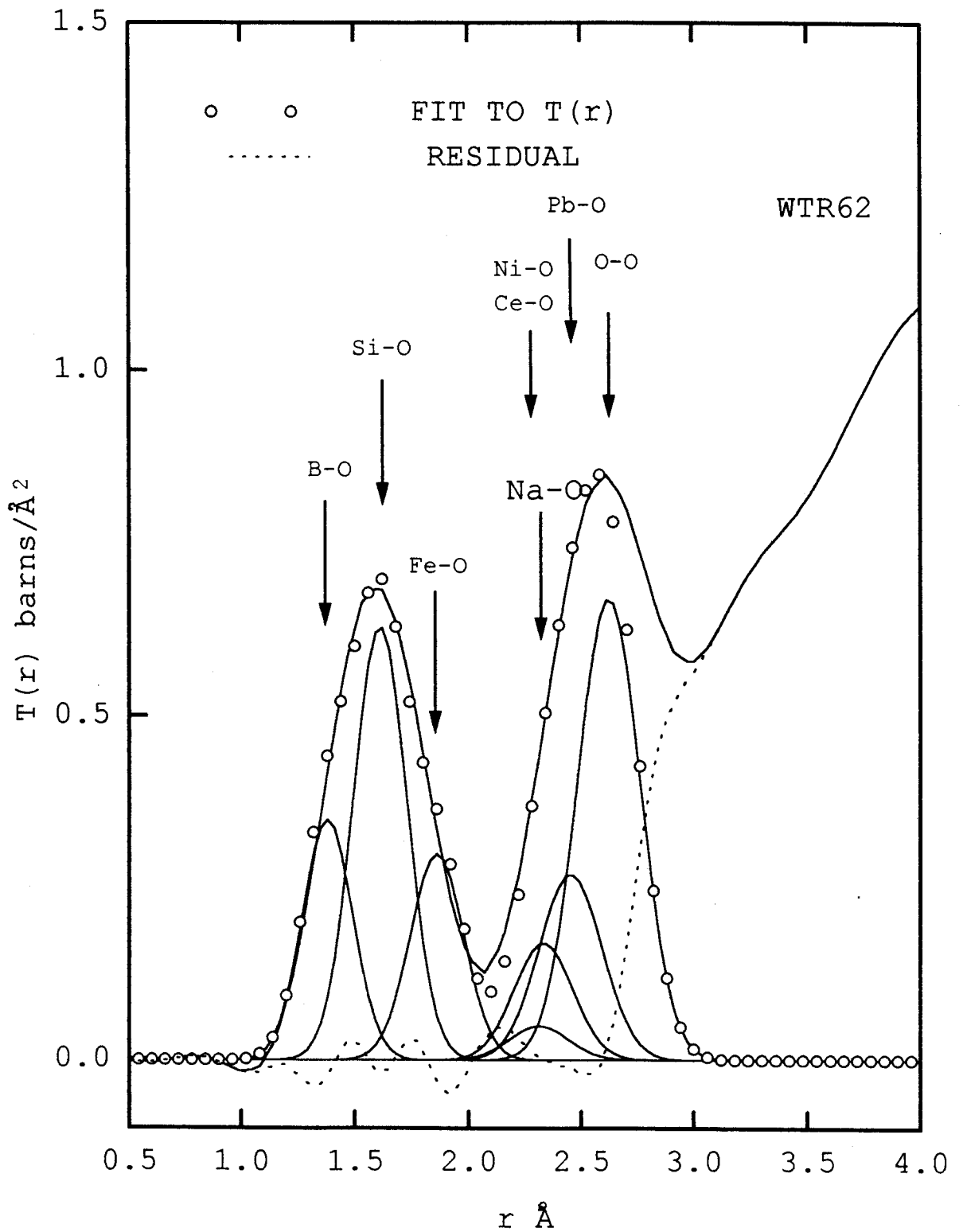
Figure 4.10: $T(r)$ of WTR62 glass with fit to the second peak (neutron data)
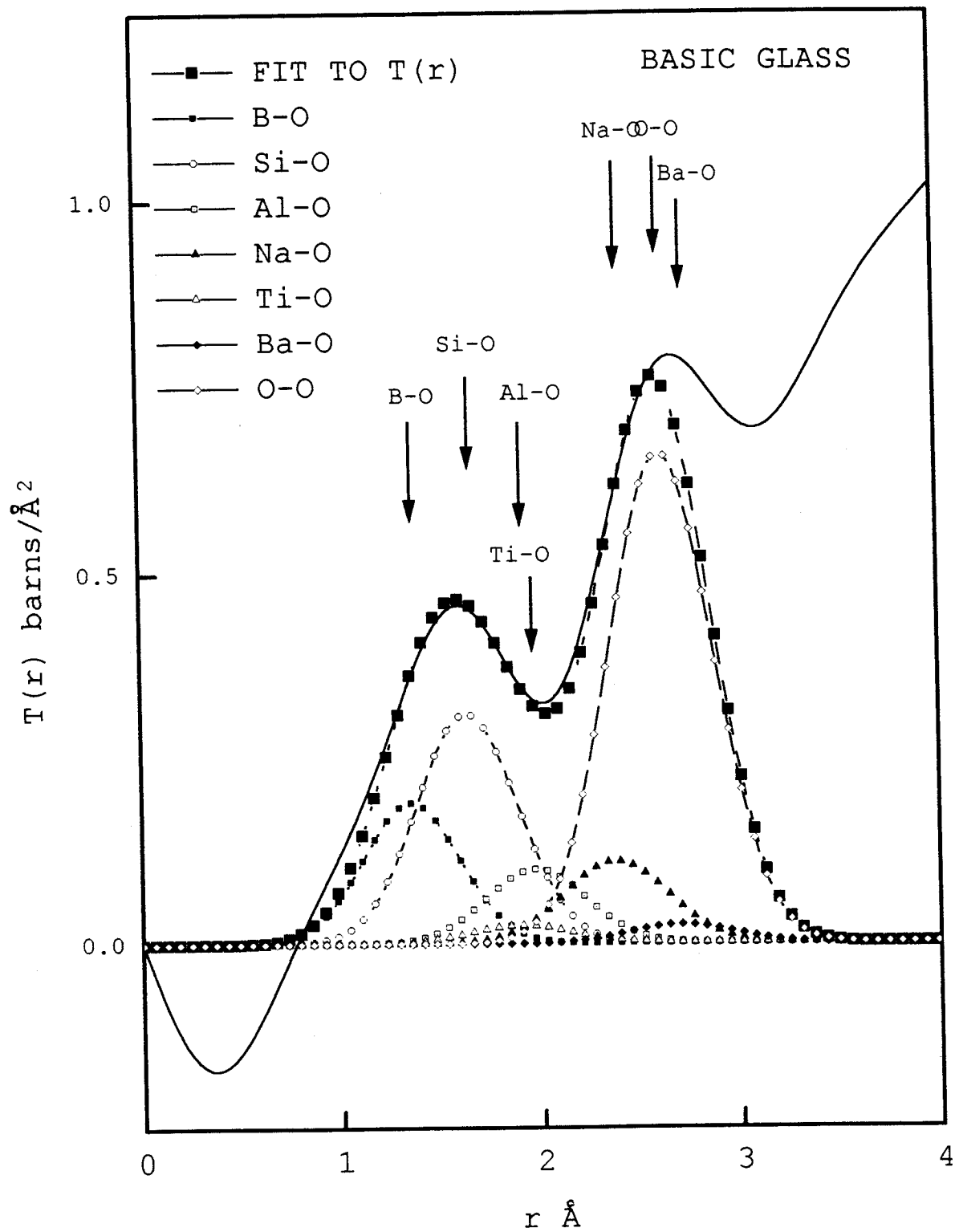
Figure 4.11: $T(r)$ of Basic glass with fit to the second peak (neutron data)

Table 4.3: Parameters obtained for waste glasses using neutron diffraction

sample	B-O		Si-O	
	n_{jk}	r_{jk} Å	n_{jk}	r_{jk} Å
Basic Glass	3.2±0.12	1.35	3.88±0.05	1.63
WTR46	3.38±0.13	1.36	4.21±0.06	1.63
WTR22	2.54±0.14	1.38	4.28±0.05	1.61
WTR30	2.4±0.16	1.38	4.21±0.06	1.62
WTR35	3.44±0.12	1.36	4.21±0.07	1.62
WTR62	2.65±0.14	1.38	4.31±0.06	1.61
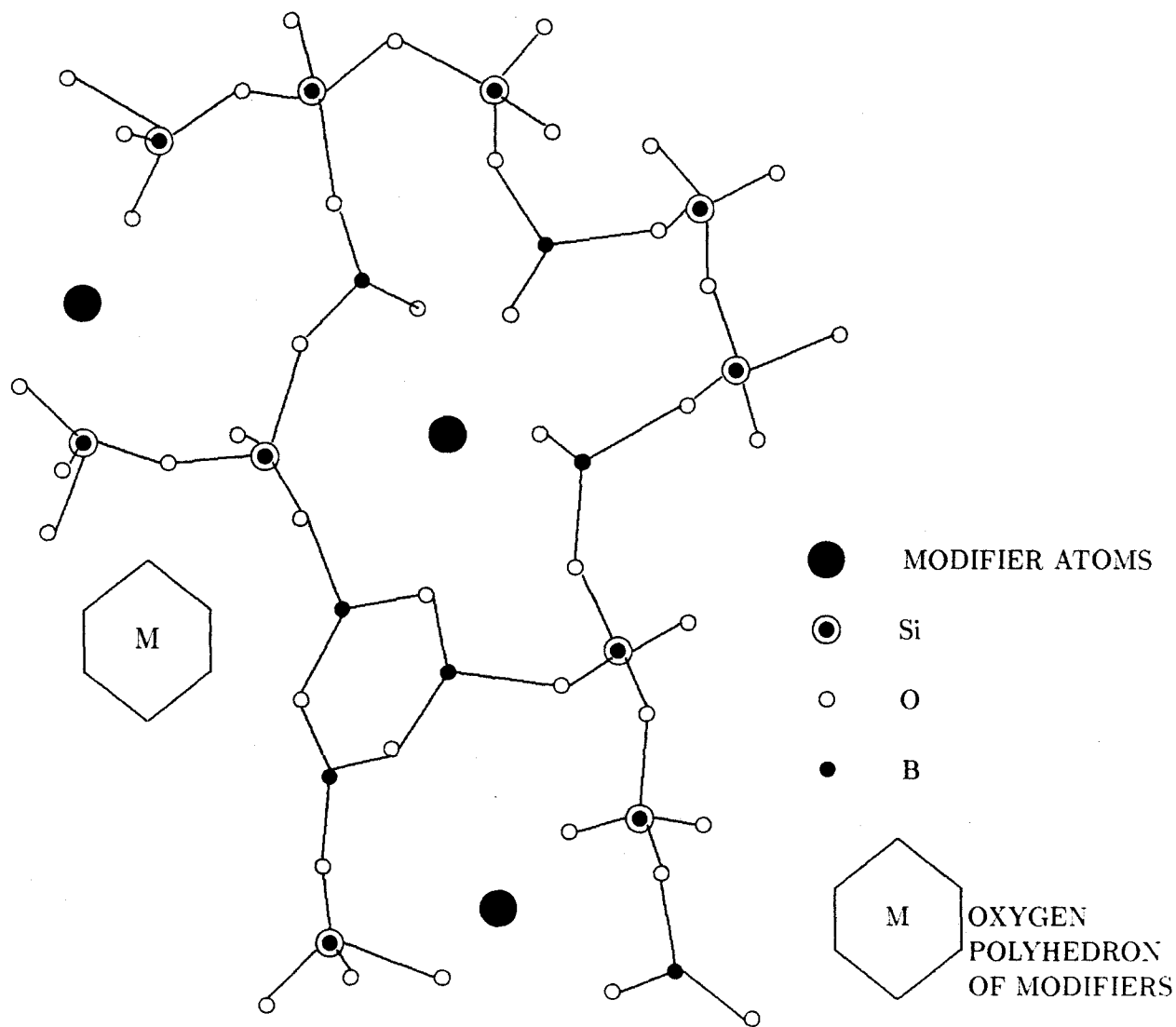
Figure 4.12: Schematic 2-D model of the network of the nuclear-waste glass

Chapter 5

RARE-EARTH PHOSPHATE GLASSES

5.1 Introduction

In Chapter 4, the difficulties encountered in the study of a multicomponent simulated nuclear-waste glass have been discussed. In order to gain insight into the effects that heavy element inclusions have on a typical host network, it was decided to study a comparatively simpler system incorporated with one type of heavy atom. The relevance of such a study to that of nuclear-waste glasses would thus be limited to a consideration of the major structural changes of the host after inclusion of the heavy element.

Phosphate glasses doped with a series of rare-earth atoms were made for this purpose. Topologically, $v - P_2O_5$ is similar to $v - SiO_2$ in the sense that the 3-D random network has tetrahedron as the basic unit. However, the tetrahedra are different in the number of bridging oxygens, but the network would be expected to be similarly affected by inclusion of heavy element oxides. In this chapter, we consider the preparation and characterization of these phosphate glasses by diffraction, optical spectroscopic and magnetic measurement methods.

5.2 Phosphate glass systems

There are three known oxides of phosphorus, viz P_2O_3, P_2O_4 and P_2O_5 of which only the latter forms a glass. The development of inorganic glasses has attracted both academic and industrial interest in recent years because they generally have higher thermal expansion characteristics and lower glass transition temperatures (T_g) compared to silicate and borate glasses [Rawson H. (1980)]. However, phosphate glasses are often degraded by water and other solvents. Because of this poor chemical durability and difficulty in maintaining pure samples, relatively little structural information is available on these glasses. These problems also limit their widespread commercial exploitation. Nevertheless, durable phosphate glasses achieved through the addition of iron oxide were developed in the last decade [Greaves et al. (1988), Sales and Boatner (1984), Sales et al. (1986)]. Ultra-low-melting phosphate glasses based on the $SnF_2 - SmO - P_2O_5$ system having a glass transition temperature around 100 °C have been synthesized [Tick (1984), Shaw (1988)]. Aqueous durability of this system was further improved by adding PbO and B_2O_3 while retaining the T_g of the earlier systems. Furthermore, phosphate glass has been used in high-power laser applications e.g. laser fusion systems [Payne et al. (1992)]. Phosphate glasses such as lead indium pyrophosphate has been used as the host glass for the first promethium-doped phosphate glass laser at 923 nm and 1098 nm [Krupke et al. (1987)]. Rare-earth phosphate glasses have drawn attention of researchers due to their applications in laser and optoelectronic technology [Durville et al. (1986), Martin (1991), Marion and Weber (1991)]. In these glasses, the rare-earth ions are incorporated in the matrix in large modifier concentrations, rather than at low dopant level. These glasses are comparatively more water stable than other binary phosphate glasses. Addition of Al_2O_3 and B_2O_3 to phosphate glasses within a certain range of composition results in an improvement in chemical durability and an increase in deformation temperature. These changes in properties, it is suggested, are due to the formation of $AlPO_4$ and BPO_4 groups in the glass affecting the properties of the glass in ways similar to changes in silicate glasses [Takahashi (1962), Kreidl et al. (1941)]. In order to understand in a general way the

wide range of properties that these systems possess, it is essential to have an insight into their atomic scale structures.

5.3 Structural review

5.3.1 Phosphates

In a recent review article, Martin (1991) noted that 'glassy P_2O_5 remains to date an almost unstudied glass'. Only a few studies have been made of the atomic structure of this glass by diffraction and other techniques.

Crystalline P_2O_5 exists in sheet form at low temperatures and in molecular form P_4O_{10} at high temperatures. The structures of these two crystal forms have been refined by Cruickshank [1964a, 1964b]. In both structures, phosphorus is tetrahedrally coordinated to oxygens with three of the oxygens bridged to neighbouring tetrahedra while the fourth oxygen is non-bridging. In P_4O_{10}, the P-O distances are 1.4 and 1.6 Å respectively for the non-bridging and the bridging oxygen. In sheet form, the corresponding values are 1.49 and 1.56 Å . The first neighbour P-P distance in sheet form is 3.0 Å which is longer than 2.82 Å found in the molecular form. A Raman study on vitreous P_2O_5 at high temperatures (530 °C) by Galeener et al. [1979] shows that this glass is made up of a 3-dimensionally connected network in which each P atom is surrounded tetrahedrally by one non-bridging and three bridging oxygen atoms (NBOs), as seen in the crystalline phase. A neutron diffraction study of this glass could not confirm the two distinct P-O distances [Wright (1991)] due to the overlapping of the corresponding peaks. Recently, a structural model for phosphate glasses has been proposed by Hoppe [1996]. In this model, addition of modifier cations not only leads to depolymerization of the network producing NBOs, but also leads to repolymerization in which the doubly-bonded oxygens (DBO) take part in creating a modified network. Three structural regions are identified, in which the number of terminal oxygen atoms is greater than, equal to, or less than the modifier cations.

In most early investigations dealing with the structure of phosphate glasses, paper chromatography techniques were used (Van Vazer [1958], Westman [1960]). It was found that the structure of alkali phosphate glass changes from a continuous network (cross-linked PO_4 tetrahedra) into a polymer type as the phosphate content decreases i.e. as the glass composition is changed from the ultraphosphate ($0 < R < 1$ where R is the metal oxide to phosphorus pentoxide ratio) to the polyphosphate ($1 < R < 2$). For the metaphosphate composition (R=1) the mean chain length approaches infinity and rings of phosphorus-oxygen tetrahedra appear.

Quinn et al. [1992] reported that in the case of binary sodium phosphates ($Na_6P_4O_{13}$), the dominant structure species will be the tetramer $(P_4O_{13})^{6-}$ while with zinc phosphates a broad spectrum of independent orthophosphate tetrahedra, dimers, trimers, tetramers, longer chains and even rings of phosphate tetrahedra occur [Beall, G.H. (1996)].

Alkali zinc phosphate glasses have been studied by Sammler et al. [1996], Crowder et al. [1997] and Efimov [1997]. These studies show that these phosphate glasses contain a mixture of n-corner linked $(PO_4)_n$ tetrahedra to an extent that depends on the composition of glass. Their results are similar to previous studies on binary lead phosphate glasses [Hosono et al. (1985), Sales et al. (1987)].

Metaphosphate glasses containing Mg, Cr, Zn, Sr and Ba have been examined by Small Angle X-ray Scattering (SAXS) [Walter et al. (1990)] to extract information on their microstructure and intermediate range structure. From the magnitude of concentration fluctuations it was concluded that the $Ba(PO_3)_2$ and $Sr(PO_3)_2$ glasses tend to form compounds. The glass $Mg(PO_3)_2$ showed its tendency towards segregation resulting in the formation of clusters of 1 nm size.

An XPS study of zinc borophosphate glass by Brow [1996] indicates the presence of tetrahedral borophosphate units in the glass when B_2O_3 in incorporated in the Zn metaphosphate network. This leads to an increasing concentration of B-O-P bonds at the expense of both P-O-P and P-O-Zn bonds.

According to Sales and co-workers [1985] and [1986] while pure lead metaphosphate glass is rather sensitive to water corrosion, the addition of 10 wt% of Fe_2O_3 results in a glass with leaching resistance as high as 10^4 times that of the Fe-free glass. Consequently, lead-iron phosphate glasses have been tested as the possible hosts for nuclear waste storage. An XRD study of such a glass [Musinu (1990)] showed that the iron ion is hexa-coordinated with oxygen atoms and interacts with lead ions giving rise to a new stable structural modification. The latter could be responsible for the chemical properties of iron-lead phosphate glass.

Differences in the various types of interlinks between Pb^{2+} and Zn^{2+} cations and the host phosphate network, when both the cations are incorporated as network formers has been studied [Shafi and Ibrahim (1998)]. Such differences have been correlated to the variation in the dissolution rates of these glasses.

5.3.2 Rare-earth phosphates

The local environment of the rare-earth ions incorporated in various host networks has been studied as the lasing properties of trivalent rare-earths depend on the type of host matrix into which it is incorporated. Peters and Houde-Walters [1997] have studied the Er^{3+} environment in aluminosilicate, flurosilicate and alkali phosphate glasses by EXAFS and found to be appreciably different in each case.

The structure of zinc metaphosphate glasses doped with Eu has been studied by Bionducci et al. [1995] by neutron diffraction. the results indicate the presence of PO_4 tetrahedra with the P-O correlation at 1.53 Å and the O-O correlation at 2.47 ± 0.02 Å. The O-O distance has been found to be in the range 2.47 to 2.5 Å [Bionducci et al. (1995), Musinu et al. (1989)] in metal-doped phosphate glasses.

A recent high resolution neutron diffraction study of the structure of the LaP_3O_9 glass revealed two different P-O distances within the PO_4 tetrahedron due to DBO and NBO's [Hoppe et al. (1998)]. The coordination number La-O was found to be of the order of 7. EXAFS studies on rare-earth metaphosphate glasses [Bowron et al. (1996)] indicate that

the average coordination number of oxygens around the rare-earth cation varies between 6 and 8.

5.4   Sample Preparation and Data collection

The rare earth oxide glasses were prepared by melting appropriate quantities of Ammonium Dihydrogen Orthophosphate (ADOP) and the rare earth oxide. A finely ground mixture of the constituents was heated in a furnace at 600 °C for about 30 minutes to remove ammonia and water vapour present in ADOP. All samples were made under similar heating schedules (Fig 5.1). The mixtures were typically kept at 1500 °C for 5-6 hours before being quenched in air. They were annealed at 550 °C for about an hour and cooled slowly to room temperature over 10 hours. Cylinders and plates of each sample were cast for neutron diffraction and X-ray as well as optical measurements respectively. Samples thus obtained were homogeneous, clear, transparent glasses having the general formula:

$$(R_2O_3)_{0.2}(P_2O_5)_{0.8}(Al_2O_3)_{0.05} \quad \text{and} \quad (R_2O_3)_x(P_2O_5)_{1-x}$$
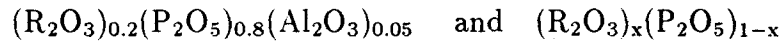
where x = 0.2 and 0.25 and R stands for La, Ce, Pr, Nd, Sm, Eu, Tb, Dy, Er or Ho. The rare-earth in this formula taken to represent both La and a second rare-earth from this series. Hereafter, the samples will be referred to as La-R-P where R is the second type of rare-earth atom. The two binary samarium and dysprosium phosphate glasses will be referred to respectively as 20SmP, 25SmP and Dy-P. Compositions of the samples are shown in Table 5.1. Vitreous P_2O_5 was not made due to the difficulty in preparation of pure water-free v-P_2O_5. However, high resolution data on v-P_2O_5 from the literature [Suzuya et al. (1998)] was used in comparisons with the data from the present work.
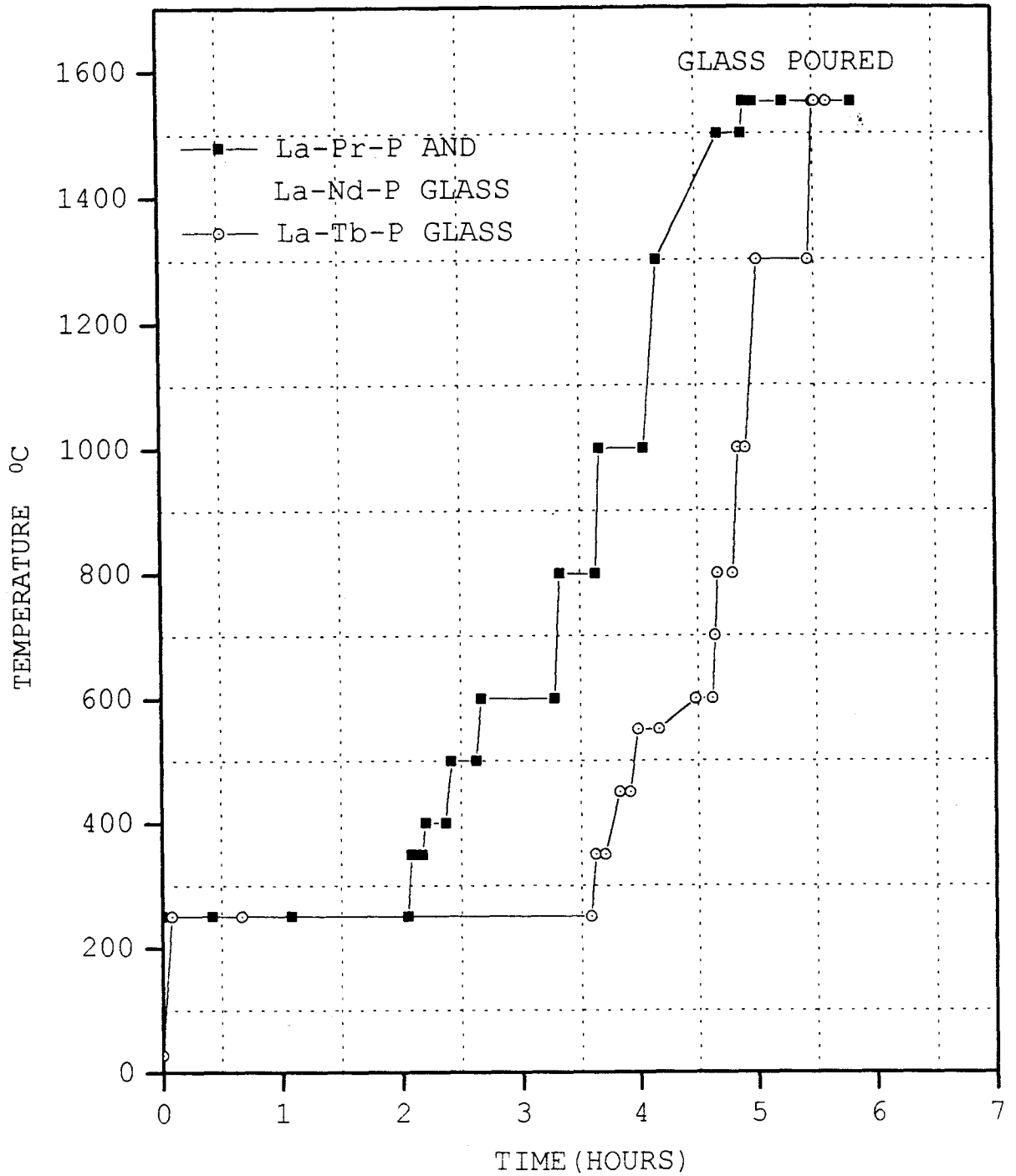
Figure 5.1: Typical heating schedules in the preparation of the rare-earth metaphosphate glasses

Table 5.1: Composition of Rare-earth phosphate glasses

Sample	P_2O_5	La_2O_3	R_2O_3	Al_2O_3
La-P	75	19.99	-	5.01
La-Ce-P	74.98	10	10.02(Ce)	5
La-Pr-P	80.49	10.73	3.46(Pr)	5.32
La-Nd-P	75	10	10(Nd)	5
La-Eu-P	75	10	10(Eu)	5
La-Tb-P	75.02	14.99	4.99(Tb)	5
La-Ho-P	74.99	10	10(Ho)	5.01
La-Er-P	75	10	10(Er)	5
20SmP	80	–	20(Sm)	–
25SmP	75	10	25(Sm)	–
Dy-P	80	–	20(Dy)	–
La-Dy-P	80	5	15(Dy)	–

5.5 Results and Discussion

5.5.1 X-ray diffraction

X-ray diffraction measurements were made with an incident Mo K_α wavelength ($\lambda =$ 0.71 Å) using a Rotating Anode Rigaku diffractometer. The angular range covered was 7° to 145° (2θ). Details of the diffractometer have been discussed in Chapter 3.

The corrected and normalized intensities $I(Q)$, intensity functions $i(Q)$ and the differential correlation functions of some glasses derived from the diffraction data are shown in Fig.5.3 to 5.12. For each glass, the quality of the normalization (to the calculated form factor) is an indication of the correctness of the assumed composition. The intensity functions appear to be similar indicating that the real-space structures are likely to be similar.

The first feature in $i(Q)$, generally known as the First Sharp Diffraction Peak (FSDP), is considered to be the signature of medium-range order and is compared for samarium containing glasses (Fig.5.10). A decrease in intensity of this feature is observed for the higher concentration of Sm and may be explained using the model proposed by Elliot [1992]. In this model, the origin of this feature in the overall $i(Q)$ is the low density or void regions in the structure of covalently bonded non-crystalline materials. The pre-peak in the partial structure factor is thought to be due to chemical short range ordering of interstitial voids around 'clusters' of the basic structural unit in the glass. According to the Bhatia-Thornton formalism [Bhatia and Thornton (1970)] for neutrons;

$$S^{BT}(Q) = \left[\frac{1}{\overline{b}^2}(\overline{b^2}S_{NN}(Q) + 2\overline{b}(\Delta b)S_{NC}(Q) + (\Delta b)^2 S_{CC}(Q)) \right] \tag{5.1}$$

where b_i is the neutron scattering length of component i, $\overline{b} = \Sigma c_i b_i$ is the compositionally weighted average neutron scattering length, the subscripts N and C for the partial structure factors refer to the number density and concentration respectively and $\Delta b = b_1 - b_2$ is the contrast factor between cluster and void. For voids, $b_2 = 0$. These authors have shown that the first peak, FSDP, in the measured structure factor originates from the pre-peak in the third term (eq.5.1) and arises from the difference between the scattering length of the

structural unit and a void. According to the above formalism, when the incorporated ions act as network modifiers by occupying positions in these voids, the scattering length of the void is a non-zero number resulting in a change in Δb. For X-ray data, the decrease in the intensity of the first feature may be explained when the neutron scattering length is replaced by the atomic scattering factor.

Total correlation functions are shown in Figs.5.13 to 5.17 and have a first peak at 1.55 Å to 1.57 Å which is a characteristic of the P-O correlation (Musinu (1989) and (1990), Suzuya et al. [1998] compared to La-P glass in Fig. 5.19a). The second feature in $T(r)$ has contributions from R-O and O-O correlations and cannot be separated due to lack of resolution. The average O-O and R-O correlations show a decreasing trend with increasing atomic number of the rare-earth on account of the "lanthanide contraction". Decomposition of further features in the $T(r)$ becomes difficult beyond the second peak. The contribution from Al-O correlations is neglected because of the relatively small concentration of Al_2O_3 and low scattering strength. The areas of the first two peaks in $T(r)$ were evaluated by fitting Gaussians. Calculation of coordination numbers of oxygen around rare-earth was attempted by fixing the O-O correlation at 2.53 ± 0.01 Å . Results are summarized in Table 5.3 and 5.4. The errors associated with the coordination numbers are large due to difficulties in assigning a unique fit to the peak. In addition to this, both the $n_O(O)$ and $n_R(O)$ coordination numbers varied appreciably depending on the positions of the $r(R - O)$ and $r(O - O)$ correlations as well as their relative areas. The $n_R(O)$ and $n_O(O)$ values that were acceptable in these (Figs.5.13 to 5.17) fits are as shown in Table 5.4. The reasons for accepting these are discussed later in this chapter (see section 5.5.2).

To evaluate the coordination number of oxygen atoms around phosphorus, it was assumed that each tetrahedron consists of a phosphorus surrounded by three singly bonded oxygens and one DBO. The coordination numbers $n_R(O)$ of this series indicate that the rare-earths occupy 'holes' or 'voids' within the network such that they are surrounded by 6-8 oxygen atoms. The coordination number larger than 6 would point to the tendency of RO_n polyhedra

to share vertices. Hoppe and co-workers [1998] attribute the features at 4.6 Å and 6.4 Å in the partial correlation function of LaP_3O_9 glass to La-La correlations from such polyhedra. The phosphate network may be formed from PO_4 tetrahedra having three, two or one corner being shared with surrounding tetrahedra. These may be designated as Q^3 (branching), Q^2 (middle) and Q^1 (end) groups in which the superscript, n, denotes the number of P-O-P links of a PO_4 tetrahedron [Brow (1994)]. In this description, the structure of phosphate glasses is determined by the number of terminal oxygens available from these Q^3, Q^2 and Q^1 groups as they coordinate the modifier cation [Hoppe (1996)]. Their numbers are related to M_{TO}, which is the ratio of number of terminal oxygen atoms to the number of metal cation (R plus Al). The number of M^{3+} cations per P atom is y/3 where y is the molar compositional ratio of $R_{2/3}O$ to P_2O_5. In the present case, y=1 when $R_2O_3 + Al_2O_3$ is considered. Every P atom has (y+1) terminal oxygens on an average. For y=1, M_{TO} is given by:

$$M_{TO} = (y + 1)/(y/3) = 6 \qquad (5.2)$$

The coordination number N_{RO} should thus be M_{TO} and are found to agree with this explanation within error. The rare-earth ions would occupy 'interstices' in the network enabling them to bond ionically with this number of surrounding oxygens held by PO_4 tetrahedra such that a continuous three dimensional network is maintained. This may account for the non-hygroscopic nature of these glasses in which the network is fastened by the rare-earth ions thereby reducing the susceptibility of linked PO_4 tetrahedra to aqueous attack.

An attempt was made to separate out the R-O correlations of the samples containing heavier rare-earths by the difference method. This method has been demonstrated on lead iron phosphate glasses to obtain iron correlations [Musinu et al. (1990)]. Difference $T(r)$ were calculated for the samples La-Eu-P, 20SmP, La-Dy-P and La-Er-P and the results for La-Dy-P are shown in Fig. 5.18. The first peak in this difference T(r) comprised the difference between the La-O and R-O correlations. Thus the shift in the position of this peak is also related to the lanthanide contraction. Its shift is compared to the ionic radii contraction in Table 5.2. Also. the increase in the scattering factor of the replaced rare-earth

ion compared to that of lanthanum has the effect of increasing the peak height as a function of rare-earth element in the *partial correlation function* for rare-earth. Three main features can be observed in the difference $\Delta T(r)$ and may be attributed to R-O and R-P correlations [Bowron et al. (1996)]

5.5.2 Calculation of O...O coordination number for vitreous P_2O_5 and rare-earth metaphosphate composition

For vitreous P_2O_5, the smallest unit is $PO_{5/2} \sim PO_{3/2}O$ (Fig. 5.2(a))

i.e. 3 oxygens are bridging oxygens (BO) and each has 6 oxygen atoms as its nearest neighbours at ≈ 2.5 Å. 1 oxygen atom is a non-bridging oxygen (NBO) and has 3 oxygen neighbours at ≈ 2.5 Å. Thus, the number of oxygen atoms around the oxygens of the $PO_{3/2}O$ unit is given by;

$$N_{O...O} = \frac{[(3/2)_{BO} \times 6] + [1_{NBO} \times 3]}{5/2} = 4.8$$

The rare-earth metaphosphate composition is given by:

$$R_2O_3 + 3P_2O_5 \rightarrow 2R(PO_3)_3$$
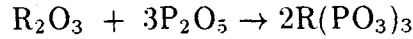
The smallest unit is $R_{1/3}PO_3$. As shown in Fig.(5.2(b)), an R atom links ionically to a $\approx POO_{2/2}O^-$ unit. In this arrangement, 2 oxygens are BO's and each of these has 6 oxygen atoms as its nearest neighbours at ≈ 2.5 Å. The oxygen atom that is doubly bonded to phosphorus is a NBO and has 3 oxygen neighbours at ≈ 2.5 Å. Also, one oxygen atom is a terminal oxygen (TO) which links to an R atom and has 3 oxygen neighbours.

Thus the coordination number of O...O is given by

$$N_{O...O} = \frac{[1_{TO} \times 3] + [1_{NBO} \times 3] + [(2/2)_{BO} \times 6]}{3} = 4$$

Thus we see that the oxygen around oxygen coordination, $n_O(O)$, is 4.8 in the pure P_2O_5 glass and decreases to 4 in the rare-earth metaphosphate.

VITREOUS P_2O_5 $R(PO_3)_3$

POO$_{3/2}$ POO$_{2/2}$O$^-$
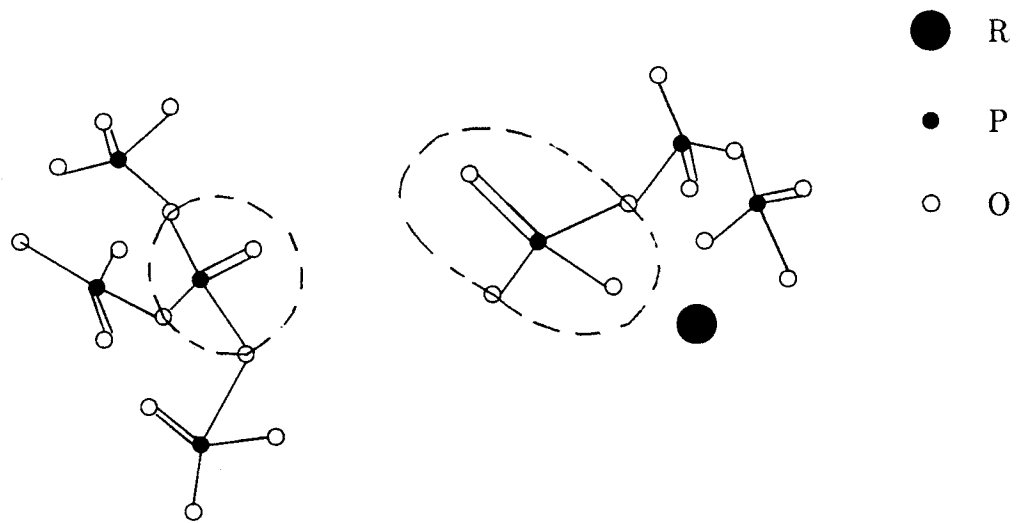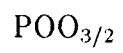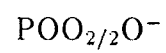
(a)   (b)

Figure 5.2: Structural unit of v $-$ P_2O_5 and rare-earth metaphosphate
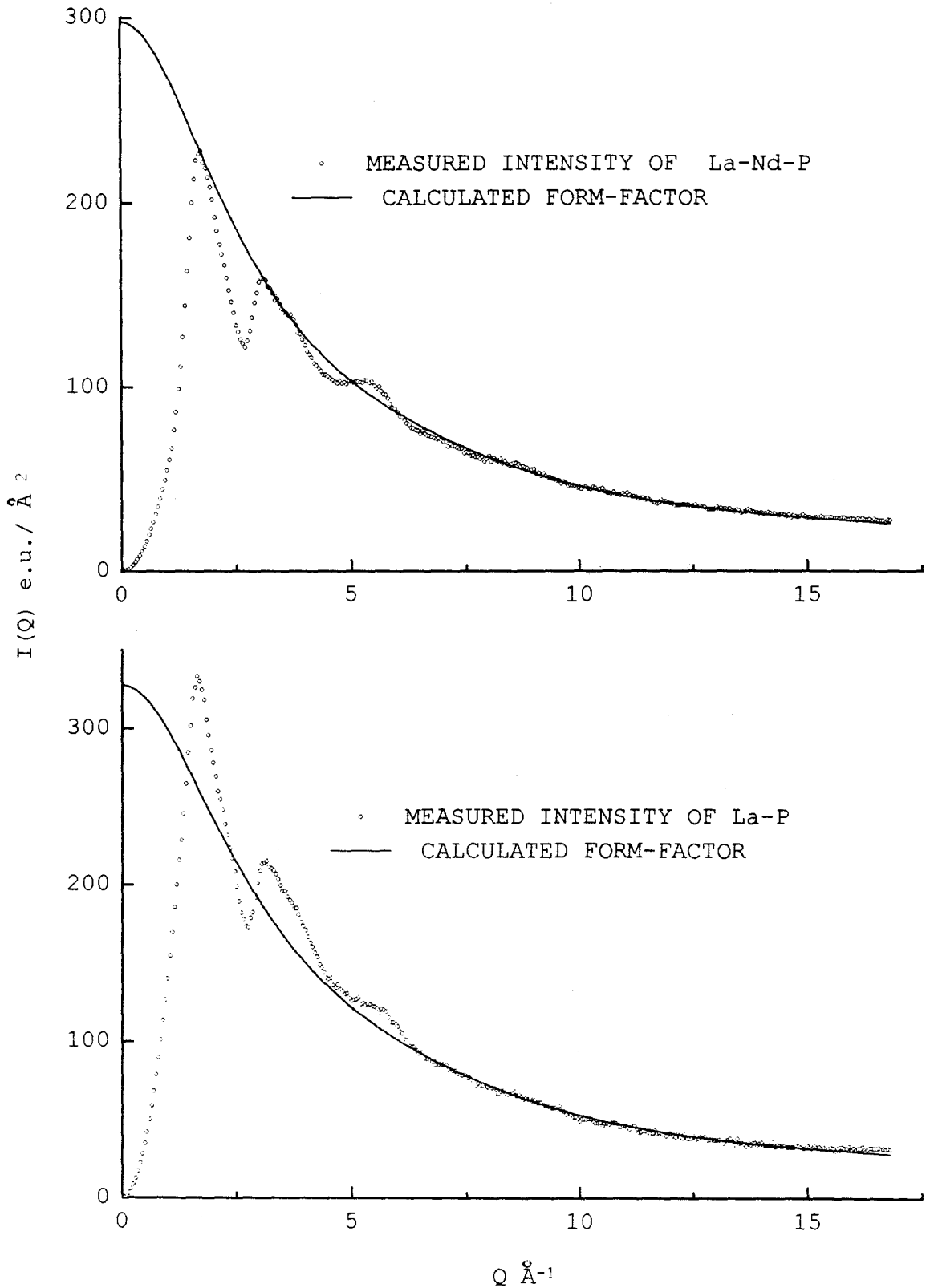
Figure 5.3: X-ray intensity pattern normalized to the calculated form factor of La-P and La-Nd-P glasses
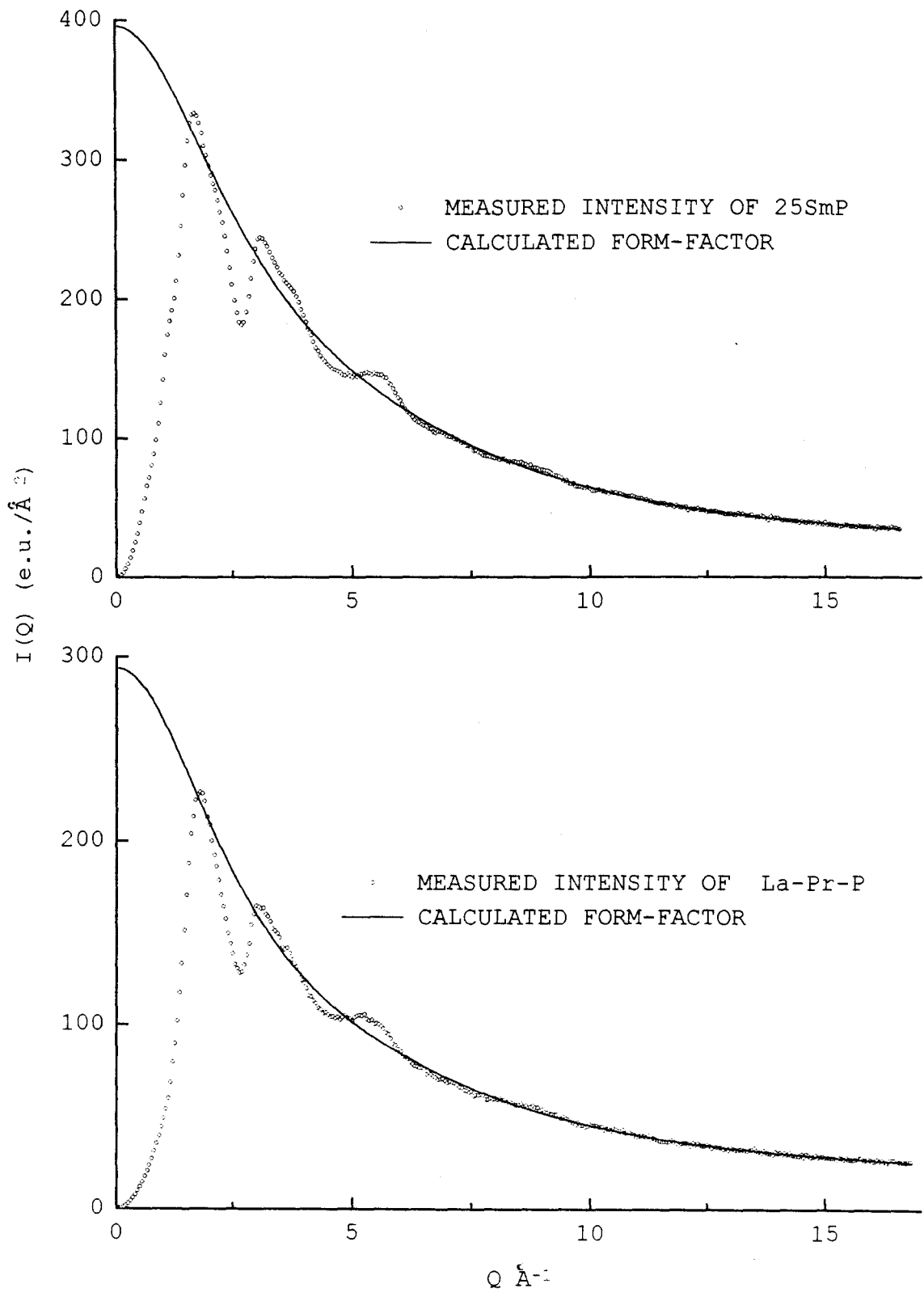
Figure 5.4: X-ray intensity pattern normalized to the calculated form factor of La-Pr-P and 25SmP glasses
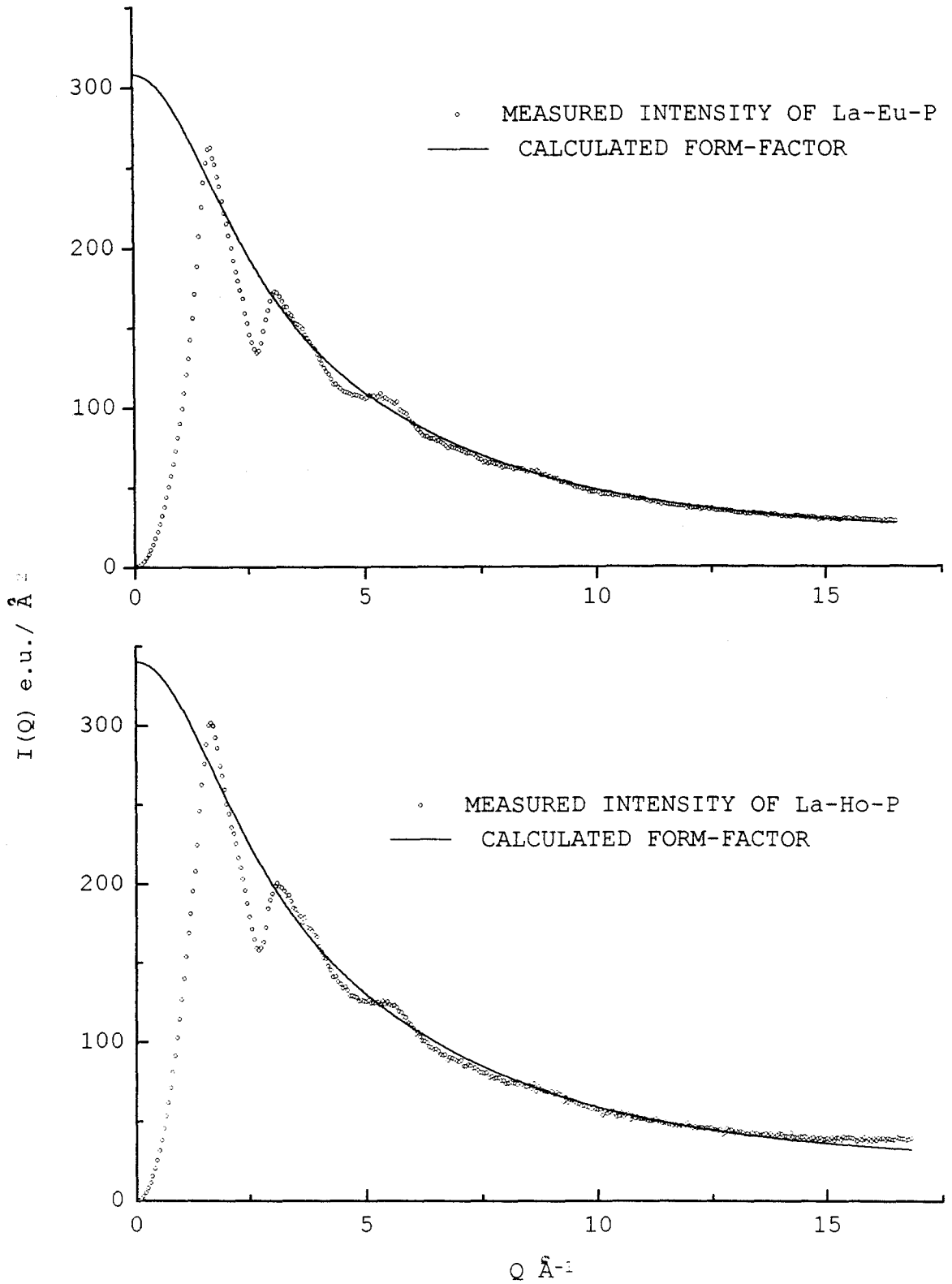
Figure 5.5: X-ray intensity pattern normalized to the calculated form factor of La-Eu-P and La-Ho-P glasses
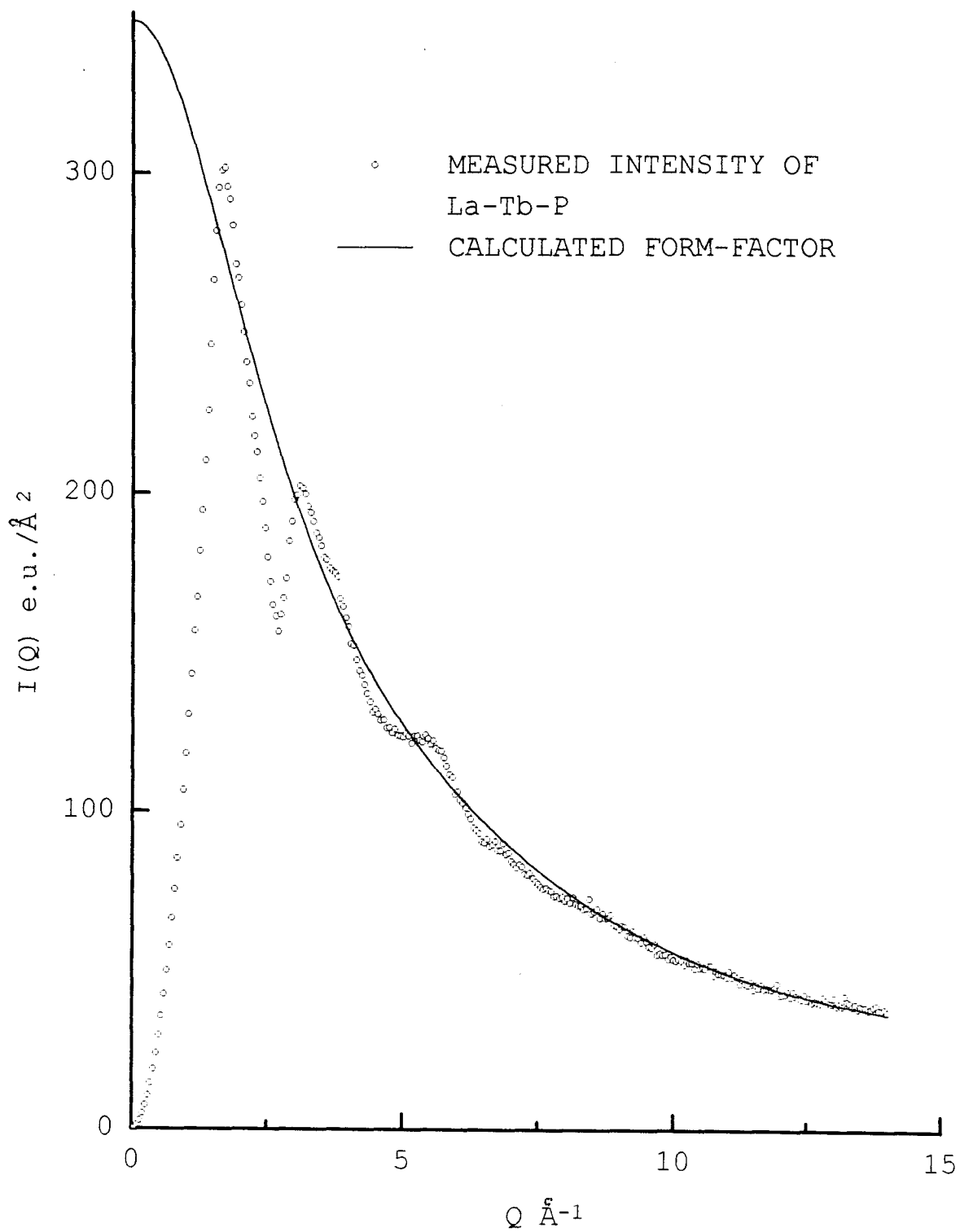
Figure 5.6: X-ray intensity pattern normalized to the calculated form factor of La-Tb-P glass
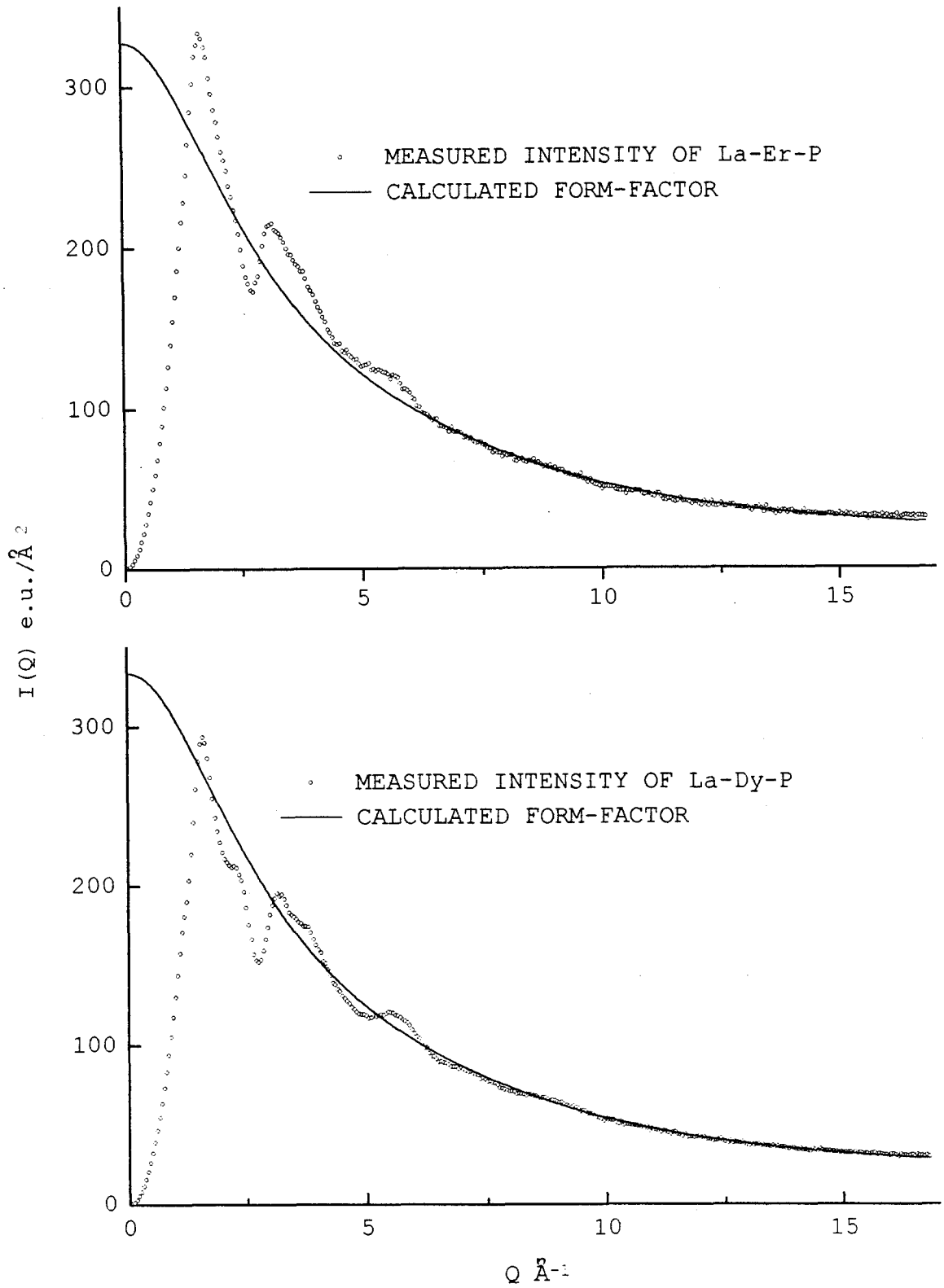
Figure 5.7: X-ray intensity pattern normalized to the calculated form factor of La-Er-P and La-Dy-P glasses
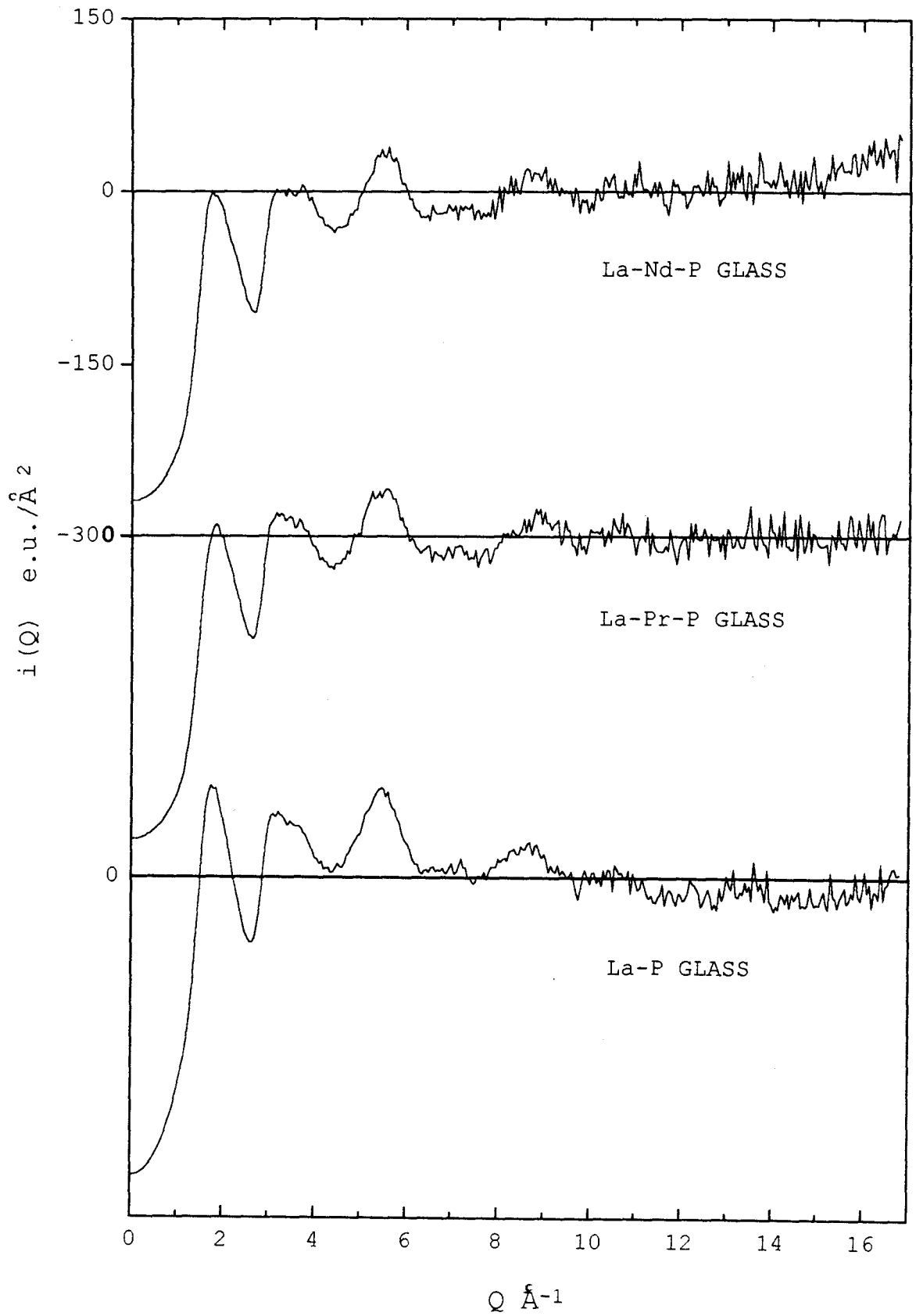
Figure 5.8: X-ray intensity function $i(Q)$ of La-P, La-Pr-P and La-Nd-P glasses
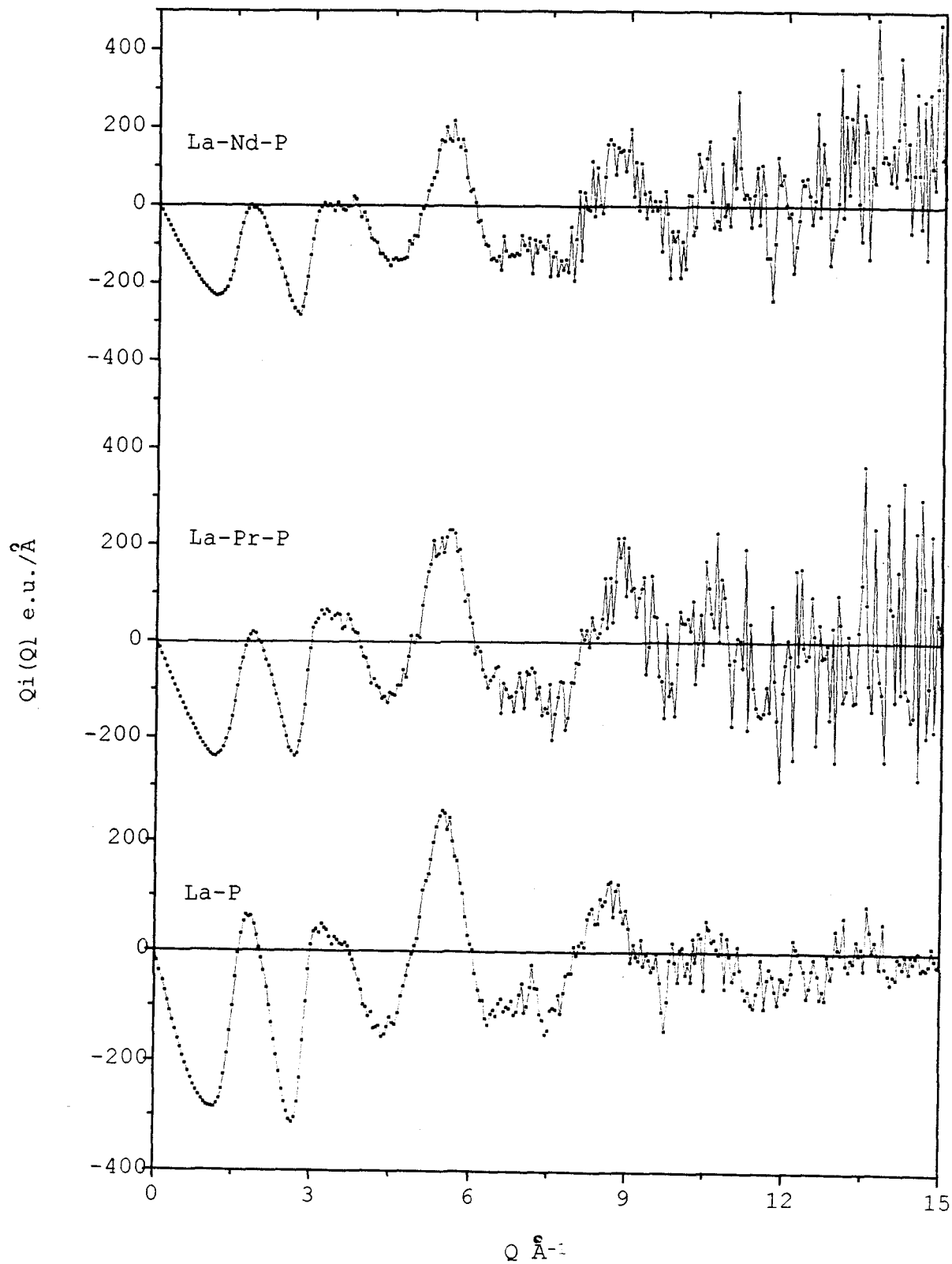
Figure 5.9: X-ray $Qi(Q)$ of La-P, La-Pr-P and La-Nd-P glasses
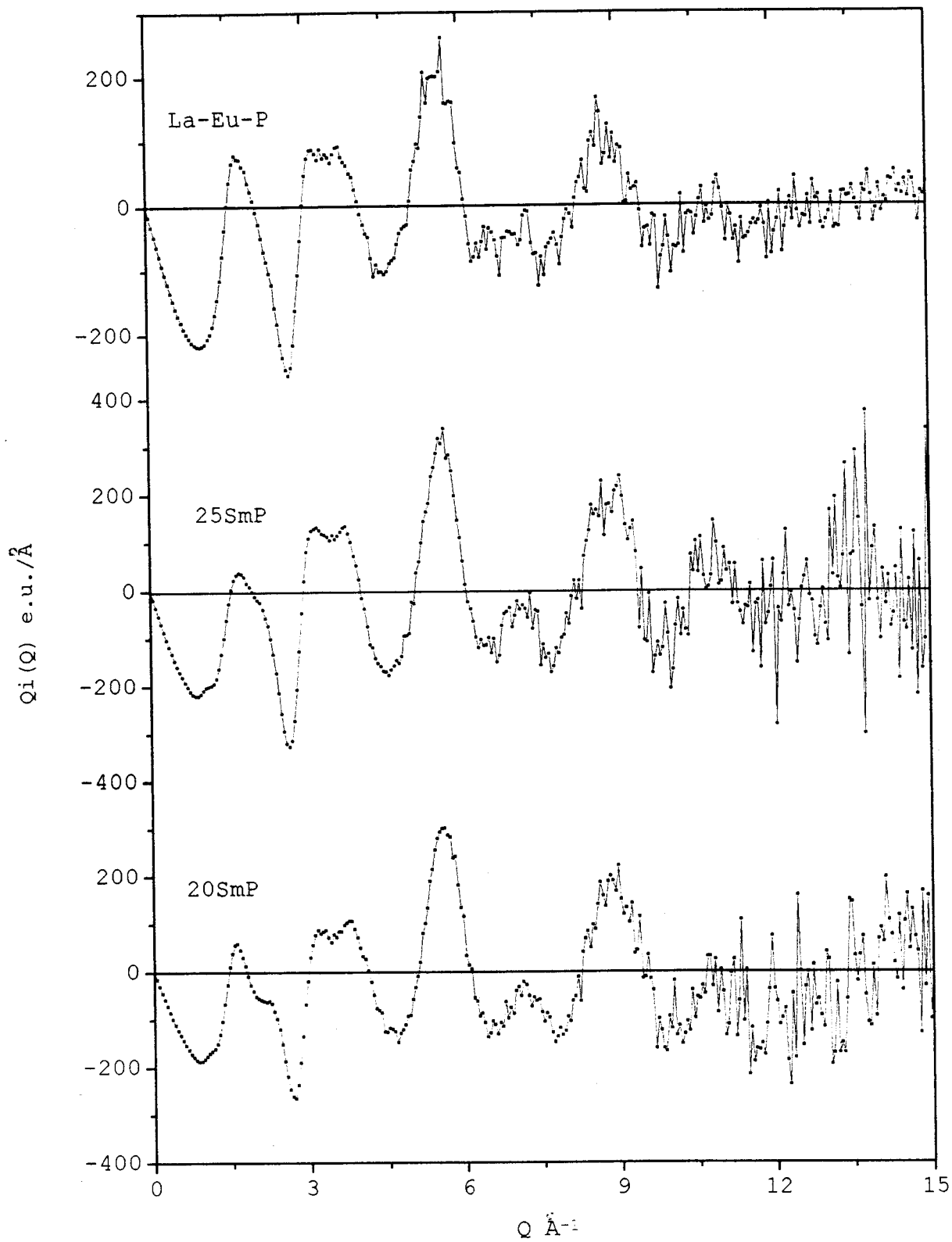
Figure 5.10: X-ray $Qi(Q)$ of 20SmP, 25SmP and La-Eu-P glasses
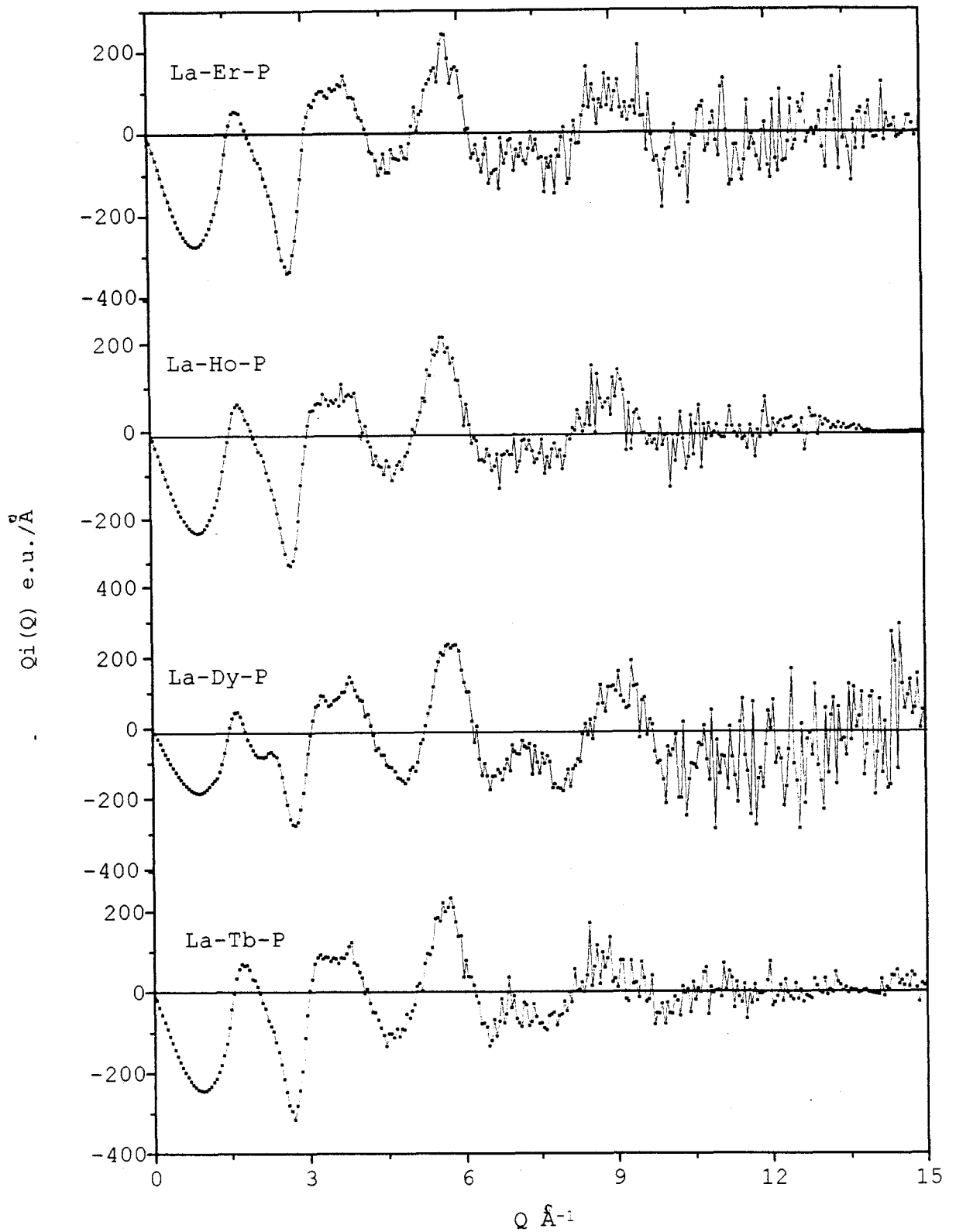
Figure 5.11: X-ray $Qi(Q)$ of La-Tb-P, La-Dy-P, La-Ho-P and La-Er-P glasses
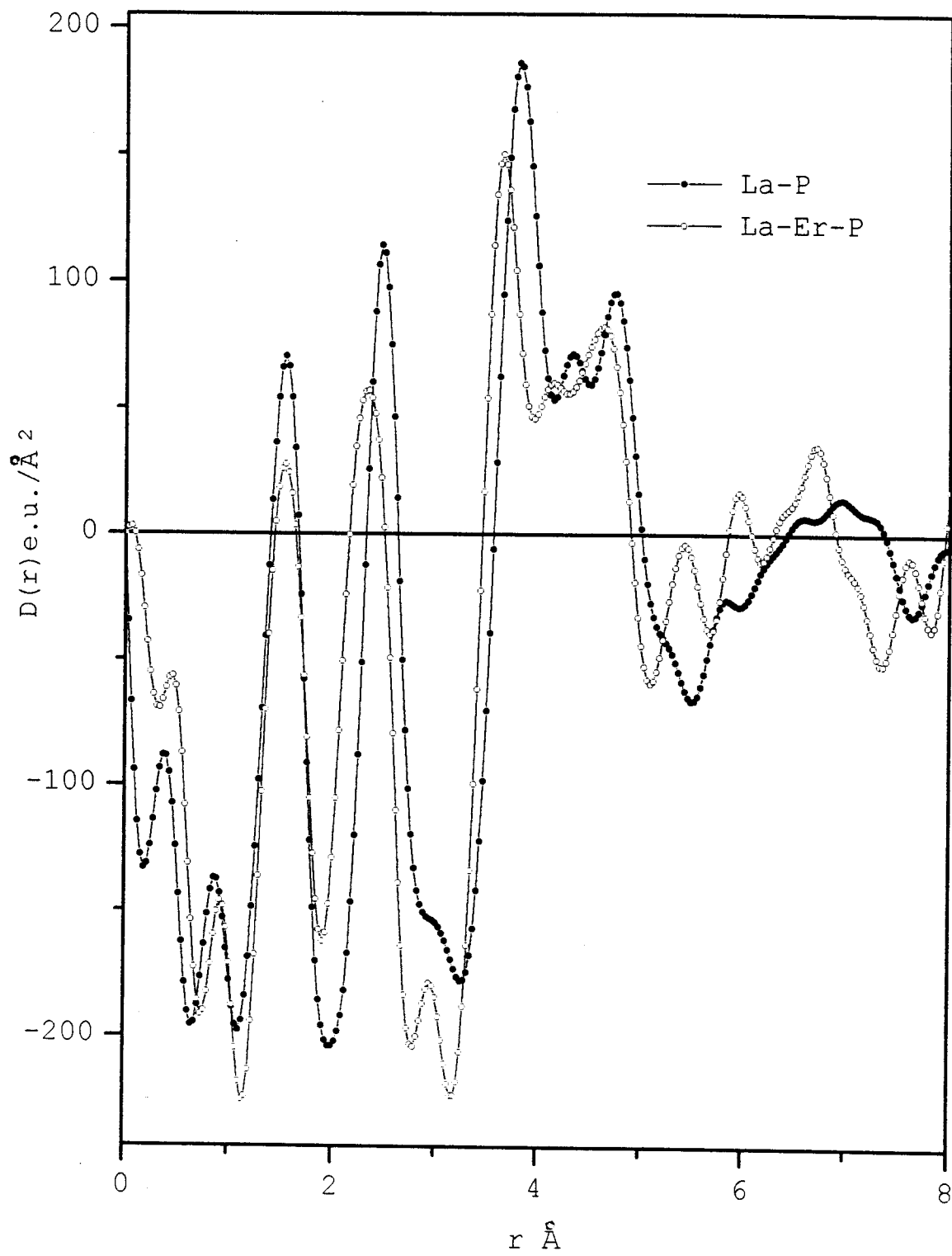
Figure 5.12: Differential correlation function $D(r)$ of La-P and La-Er-P glasses (X-ray data)
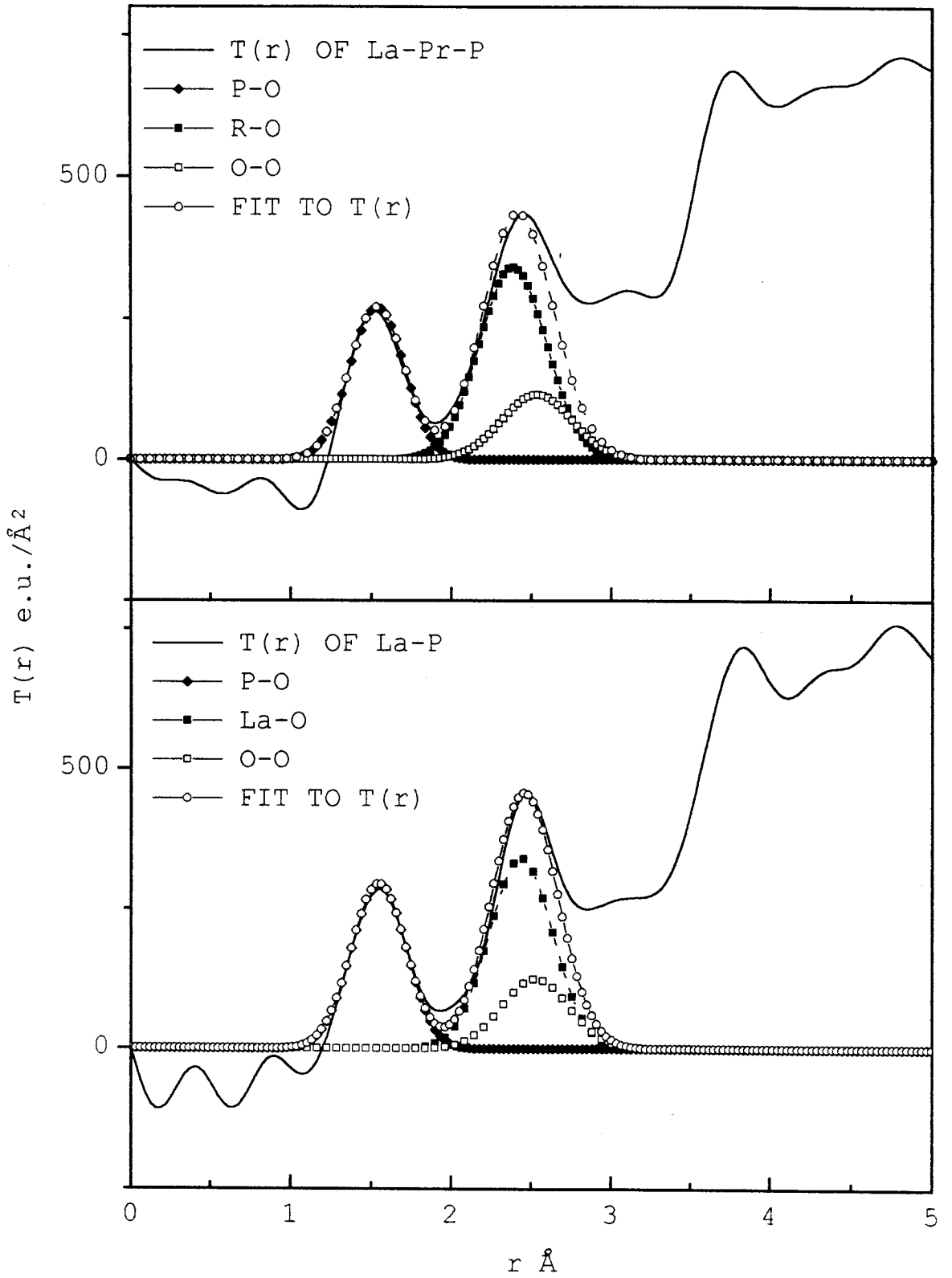
Figure 5.13: Total correlation functions $T(r)$ of La-P and La-Pr-P glasses (X-ray data)
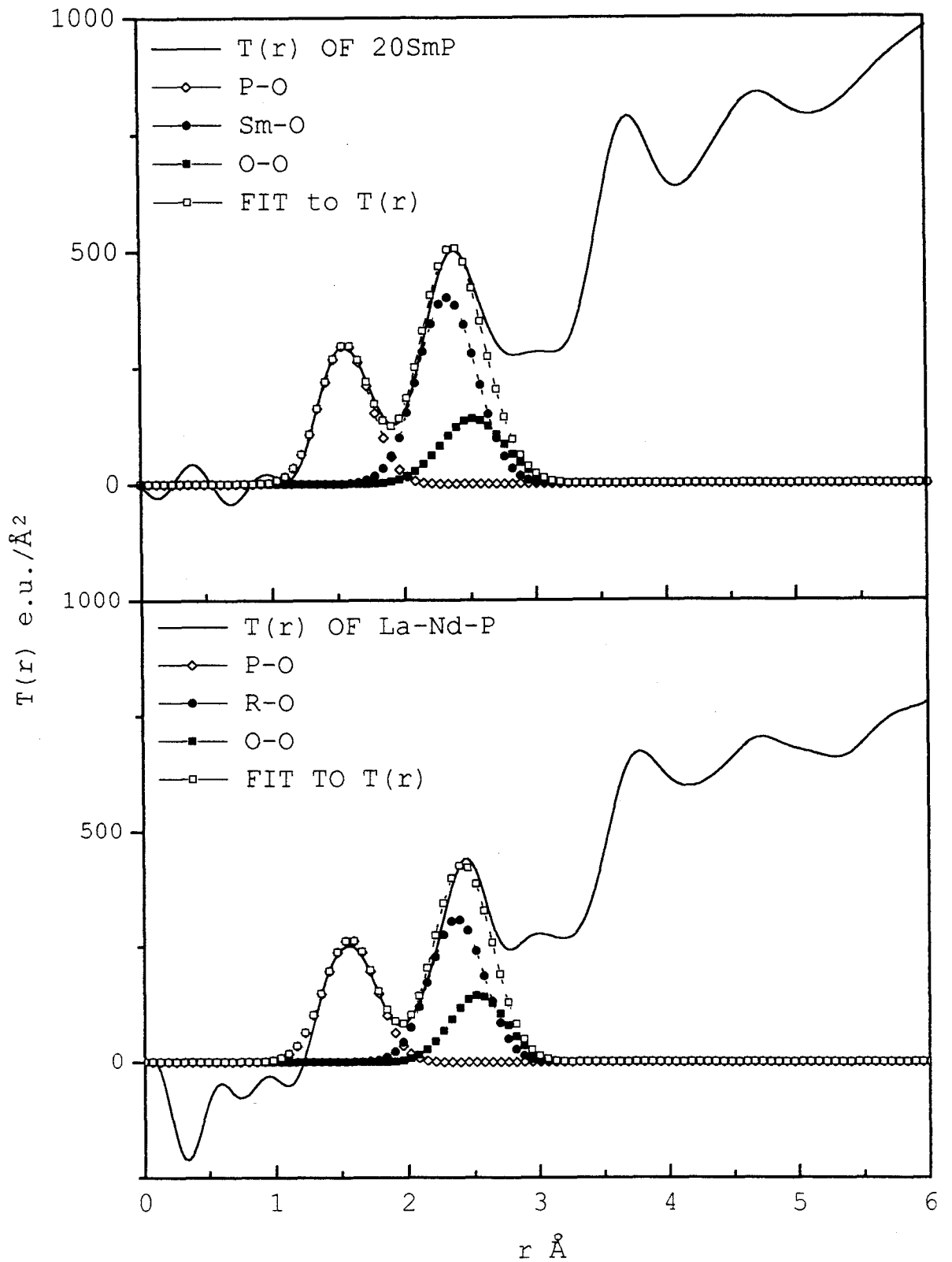
Figure 5.14: Total correlation functions $T(r)$ of 20SmP and La-Nd-P glasses (X-ray data)
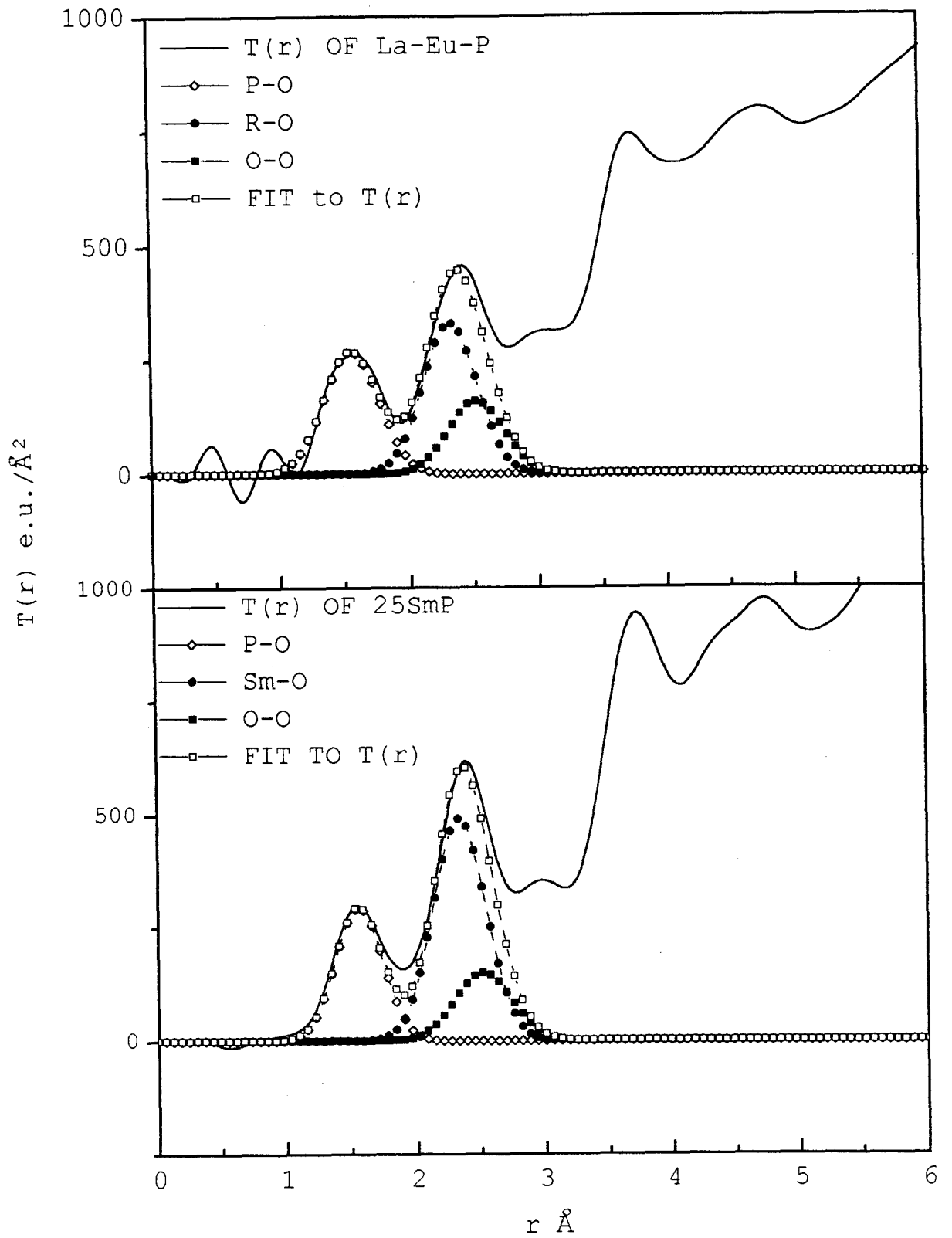
Figure 5.15: Total correlation functions $T(r)$ of 25SmP and La-Eu-P glasses (X-ray data)
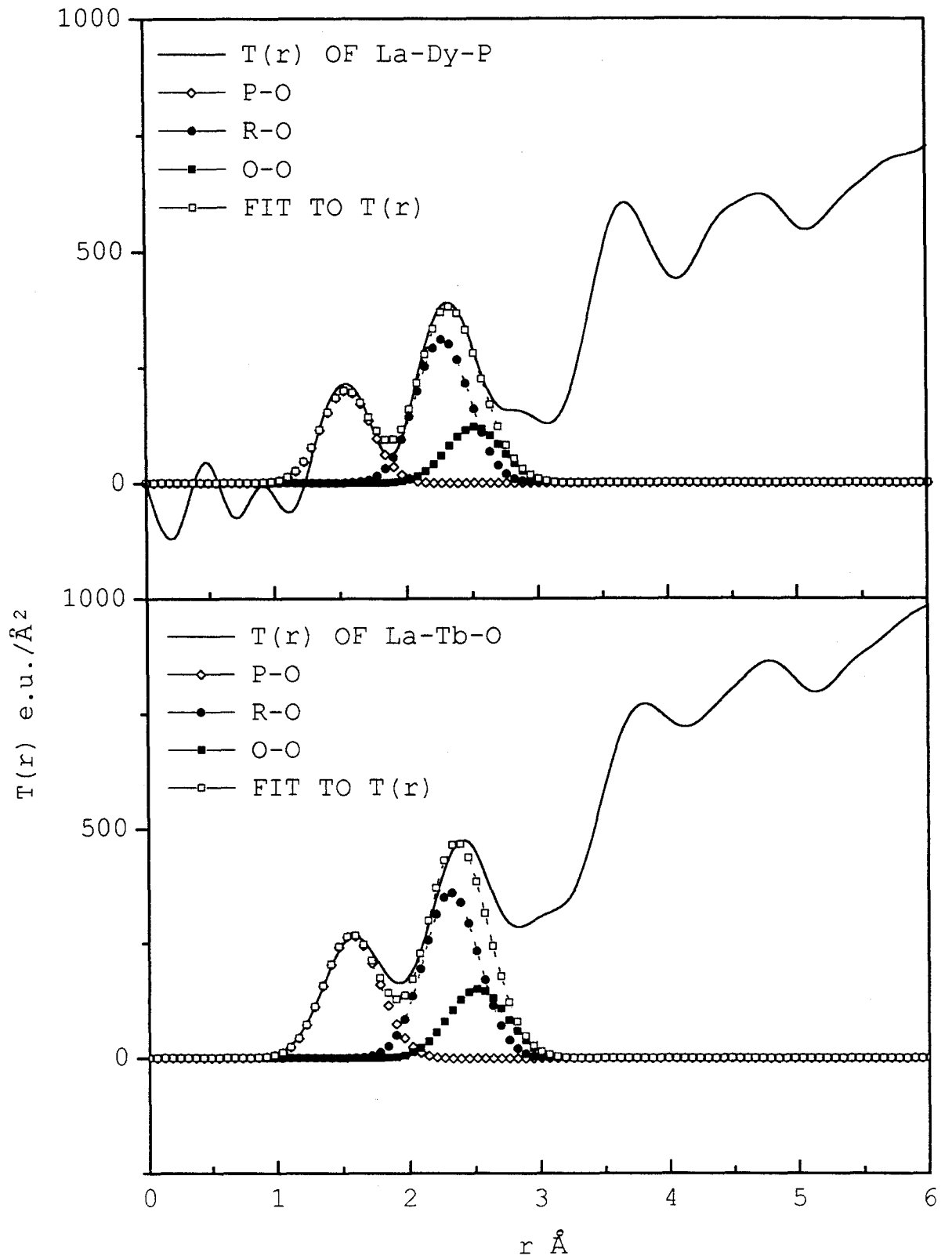
Figure 5.16: Total correlation functions $T(r)$ of La-Tb-P and La-Dy-P glasses (X-ray data)
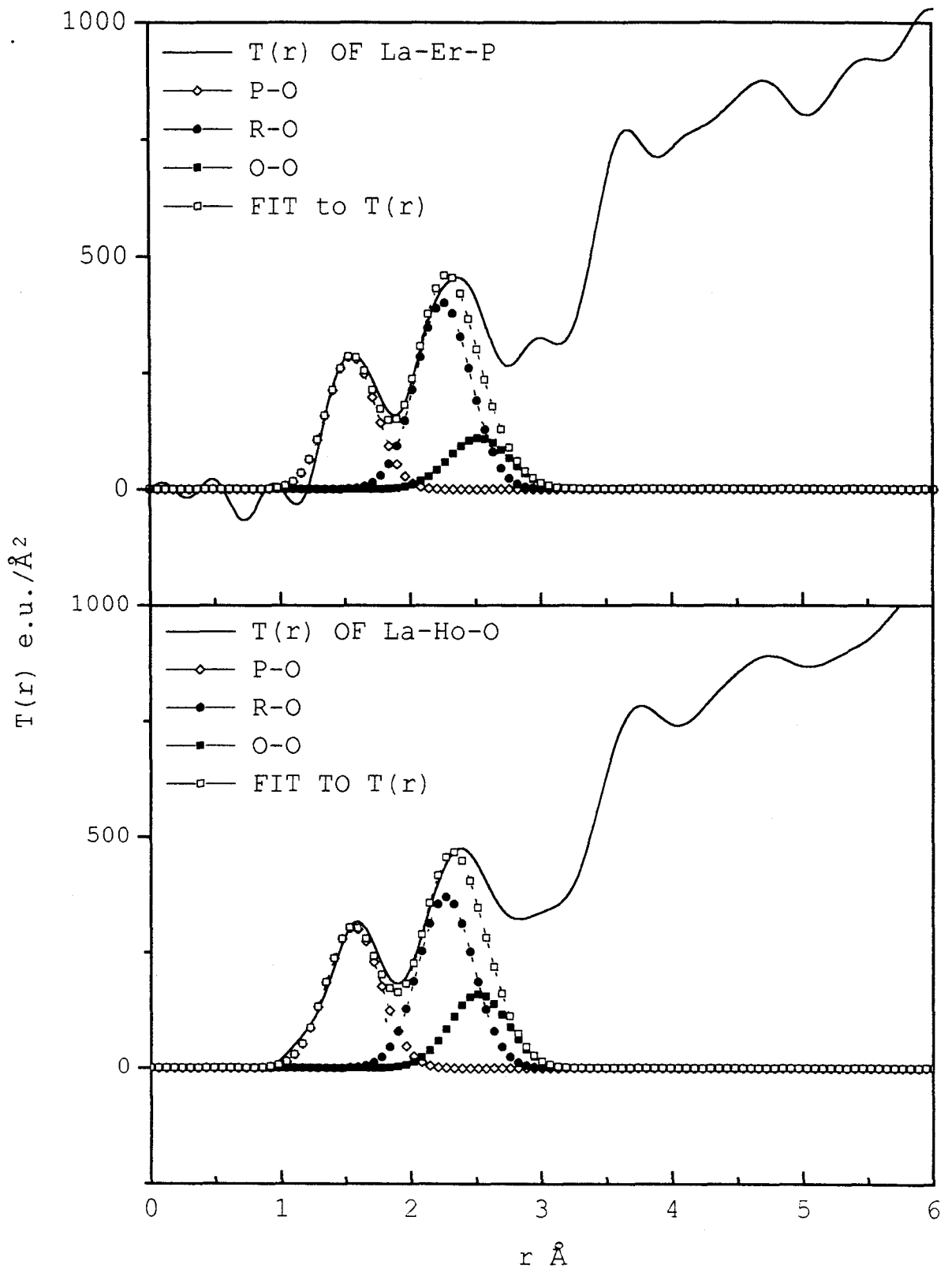
Figure 5.17: Total correlation functions $T(r)$ of La-Ho-P and La-Er-P glasses (X-ray data)
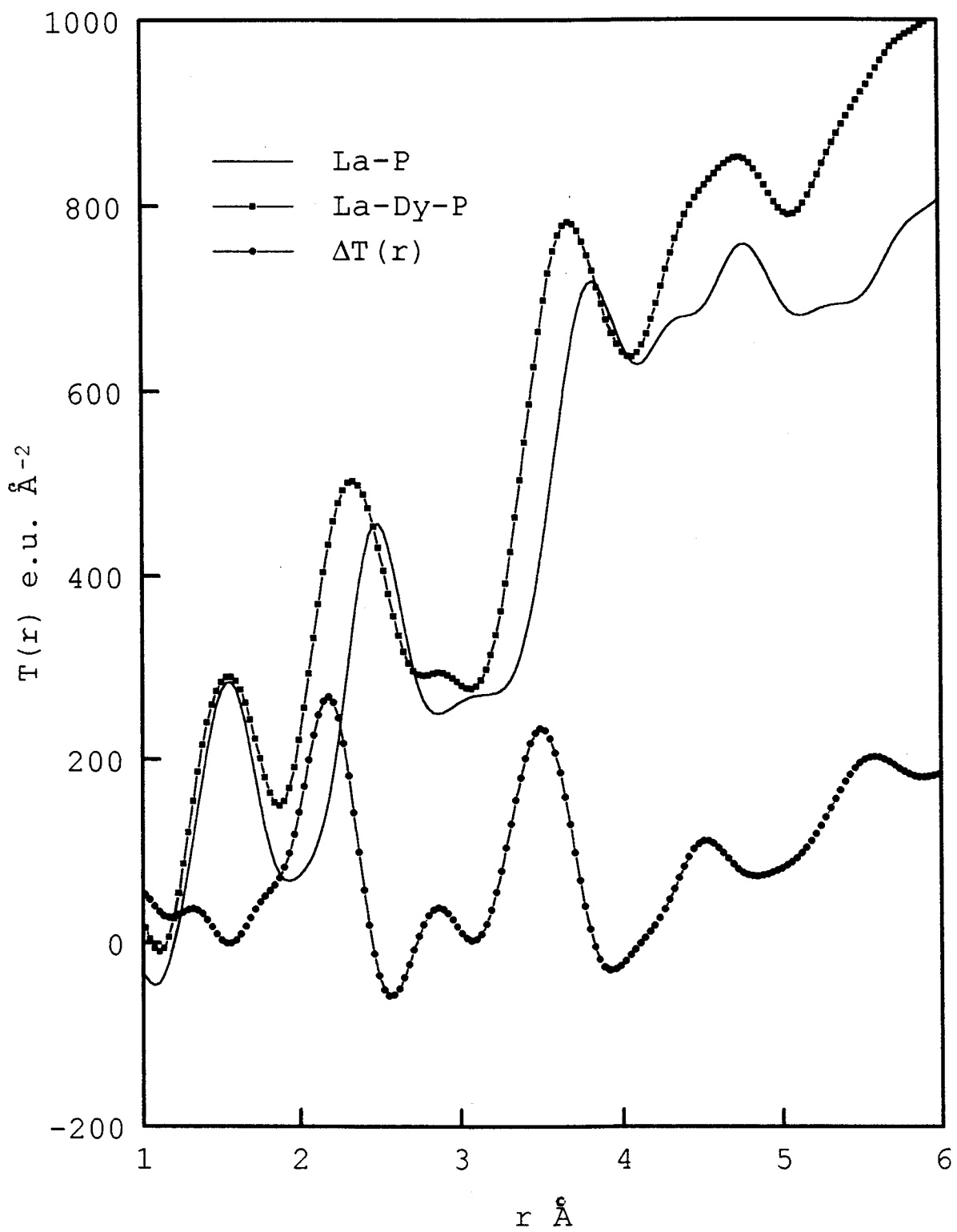
Figure 5.18: Partial total correlation function $\Delta \ T(r)$ of La-Dy-P glass   (X-ray data)

Table 5.2: Comparison of the r(R-O) correlations [after Templeton and Dauben (1954)] and the position of the second peak in $T(r)$ from XRD

Sample	r(R-O) Å (reported)	Change w.r.t. r(La-O) (Å)	Position of 2nd peak in $T(r)$ (Å)	Position of 2nd peak in $\Delta T(r)$ (Å)
La-P	2.44 (La)	-	2.48	-
La-Pr-P	2.393 (Pr)	0.047	2.47	-
La-Nd-P	2.375 (Nd)	0.065	2.46	-
25smP	2.344 (Sm)	0.096	2.39	2.25
La-Eu-P	2.33 (Eu)	0.11	2.41	2.21
La-Tb-P	2.303 (Tb)	0.137	2.39	2.19
La-Dy-P	2.288 (Dy)	0.152	2.31	2.18
La-Ho-P	2.274 (Ho)	0.166	2.37	2.17
La-Er-P	2.261 (Er)	0.179	2.36	2.13

106

Table 5.3: Calculated areas of Peak shape functions

Sample	P-O	La-O	R-O	O-O
La-P	122.737	435.714	—	73.085
La-Pr-P	123.409	438.101	454.898	73.485
La-Nd-P	122.49	434.838	459.776	72.938
La-Eu-P	122.227	433.906	483.32	72.78
La-Tb-P	122.677	435.501	501.306	73.049
La-Dy-P	120.797	428.484	501.104	71.873
La-Ho-P	119.774	425.196	537.07	71.32
La-Er-P	121.875	432.65	521.482	72.572

Table 5.4: Correlations and bond distances obtained by X-ray diffraction

Sample	Parameters					
	$r(P-O)$ Å	$n_P(O)$	$r(R-O)$ Å	$n_R(O)$	$r(O-O)$ Å	$n_O(O)$
La-P	1.54(1)	3.44(16)	2.44(2)	7.76(83)	2.53(3)	3.27(49)
La-Pr-P	1.54(1)	3.13(18)	2.38(3)	7.81(85)	2.54(2)	3.15(39)
La-Nd-P	1.56(1)	3.67(17)	2.37(3)	6.86(54)	2.53(2)	3.82(43)
La-Eu-P	1.56(1)	3.90(19)	2.32(4)	7.14(67)	2.52(3)	4.30(64)
La-Tb-P	1.56(1)	4.09(26)	2.30(3)	6.42(68)	2.52(2)	4.40(57)
La-Dy-P	1.55(1)	3.69(21)	2.28(3)	6.21(93)	2.52(3)	3.17(37)
La-Ho-P	1.56(1)	4.54(25)	2.27(4)	7.40(63)	2.52(2)	4.46(63)
La-Er-P	1.55(1)	3.76(23)	2.26(4)	8.09(97)	2.53(4)	3.19(42)
20SmP	1.56(1)	3.81(18)	2.33(3)	8.50(92)	2.52(3)	4.18(53)
25SmP	1.56(1)	4.36(20)	2.34(3)	7.44(96)	2.52(4)	4.15(71)

N.B.: Figures in parentheses refer to errors in the last decimal place(s).

5.5.3 Neutron Diffraction studies of Phosphate glasses

Neutron diffraction experiments were performed using an incident wavelength $\lambda = 0.783$ Å with the High-Q diffractometer discussed in Chapter 3. The set of four samples with rare-earth cations having low magnetic moment were chosen for the measurements. These were (see Table 5.5); La-P, La-Ce-P, La-Pr-P and La-Nd-P. Transmission factor values were found to vary from 82% for the Ce-containing sample to 75% for the Nd containing sample. The standard data corrections such as background, absorption, multiple scattering etc. were all applied. Vanadium normalized intensities were corrected for deviations from the static approximation. This correction was small due to the presence of heavy atoms. Intensities normalized using the Krogh-Moe-Norman method are shown in Figs.5.19 and 5.20.

The FSDP which generally occurs between 1 Å^{-1} to 2 Å^{-1} for covalent glasses [Elliot (1992)] is at 1.65 Å^{-1} (Fig. 5.21). The intensity of this peak shows an increasing trend from the sample containing La to that containing Nd. Elliot [1992] interpreted the model of Bhatia and Thornton regarding the FSDP as being due to voids which are filled by added cations serving as network modifiers. Thus the scattering length of the void which is initially zero, changes to a non-zero number and hence the increase or decrease in the height of FSDP depends on the sign of the neutron scattering length (positive or negative) as also its magnitude. In the present case, the neutron scattering length of La is 8.24 fm which is higher than the other three rare-earth cations i.e. the neutron scattering lengths of Ce, Pr and Nd are respectively 4.84, 4.58 and 7.69 fm. Thus the value of Δb in eq.(5.1) is smallest for the La-P glass. This explains the decrease in intensity of the FSDP and may be considered as an indication of the network modifying role of the rare-earth atoms. In order to check the possible contribution from magnetic scattering to the scattered intensities. a sample having a rare-earth ion of high magnetic moment (e.g. Tb) was measured with polarized neutrons. However, no magnetic scattering was observed in this sample indicating that only the atomic structure factor contributed to the scattered intensities.

Differential correlation functions are shown in Fig.5.22. The first feature at 1.55 Å is

due to P-O bonds while the second peak is a combination of R-O and O-O correlations. The total correlation functions from which the coordination numbers were calculated are shown in Figs.5.23 to 5.26. These functions primarily determine the details of P-O correlations. The details of the Gaussian fitting to the peaks in $T(r)$ to obtain the coordination numbers and correlations are summarized in Table 5.6. The contribution from R-O correlations was calculated by fixing the O-O correlation at approximately 2.53 Å . The parameters obtained from the second peak are in error due to the difficulty in assigning a unique fit to this feature. As with the X-ray data, it was observed that small variations in the $r(R - O)$ and $r(O - O)$ positions and areas of these fits gave significant variations in the $n_R(O)$ and $n_O(O)$ with good fits to the second peak in $T(r)$ [Fig.5.27(b)]. Those fits which gave $n_O(O)$ values of about 4 were considered acceptable. A knowledge of the position of the $r(P - P)$ correlation at 2.94 Å to 2.98 Å (also found by Mountjoy et al. [1998]) gave (from a geometrical consideration) inter-tetrahedral bond angle β in the range 143° to 148° and a consequent $n_O(O)$ of about 4. The implication of this β value is that these glasses have an open structure of corner linked (Q^2) tetrahedra. The fits to the second peak in which $n_O(O)$ lay in the range of 6-8 were rejected, as the value of $r(P-P)$ (2.94 Å to 2.98 Å) put a constraint on the value of β (143° to 148°). For $n_O(O)$ to lie in the range 6-8, β would need to be approximately 108° as expected in a random close packed (r.c.p.) structure. Thus it may be concluded that an r.c.p. array of oxygen atoms is inadmissible in these glasses.

The variation of contrast by X-ray and neutron diffraction measurements was used to obtain information about the coordination numbers of R-O and O-O. The results of such a comparison are shown in Table 5.7. Thus the coordination number R-O of these glasses is in the range 7-8 with the O-O coordination at a value close to metaphosphate composition.

A model of this type of rare-earth phosphate glass may thus be based on corner-linked PO$_4$ tetrahedra in which Q^2 units predominate. The rare-earth ions in this system occupy 'holes' in this continuous tetrahedral network while being ionically bonded to the oxygen atoms of the tetrahedral tetrahedral units and six to eight-fold coordinated to these atoms.

A 74 atom hand-built model based on these structural considerations has been made. A 2-D projection of this model may be seen in Fig. 5.28.

5.5.4   IR absorption studies on phosphate glasses

The structural role of trivalent cations in phosphate glasses has been investigated by several workers [Greaves et al. (1988), Mierzejewski et al. (1988)]. It is known that the addition of Al^{3+} to the phosphate glass helps in improving its chemical durability [Takahashi (1962), Kreidl et al. (1941)].

All samples were ground to fine powders and mixed with potassium bromide before being pelletised for the IR measurements. The instrumental details have been given in Chapter 3. A frequency range of 400-1400 cm^{-1} was scanned in these FTIR measurements. The spectra are shown in Figs. 5.29 and 5.30. The peak positions in the IR spectra of these glasses are shown in Table 5.8. The regions of interest are the breathing modes of PO_n groups ($\nu > 900$ cm^{-1}), the stretching P-O-P modes (600-1000 cm^{-1}) and the bending modes of PO_n (400 - 600 cm^{-1}) [Exarhos et al. (1978), Corbridge and Lowe (1954)]. The detailed assignment of these is compared with the reported values in Table 5.9. From the presence of the P=O and O-P-O stretching modes and the PO_3 symmetric mode, it is clear that the basic unit is a PO_4 tetrahedron. The changes after addition of Al^{3+} to the phosphate network are as follows:

- The band at 1071 cm^{-1} decreases in intensity with a slight increase in 1180 cm^{-1} band.

- The feature at 1254 cm^{-1} shows a downward shift in its frequency value.

- The well defined peak at approximately 1308 cm^{-1} in binary phosphate glasses disappears after addition of Al_2O_3.

The addition of Al_2O_3 results in a significant variation in the number and intensities of the IR bands indicating structural change. More specifically, the decrease in the intensity of the 1071 cm^{-1} ($\nu_s - PO_2$) in aluminophosphates with a replacement by a new band at

Table 5.5: Samples used for neutron diffraction measurements

Sample	Diameter (cm)	Length (cm)	% Transmission
La-P	0.717	3.20	81.1
La-Ce-P	0.708	2.75	82.5
La-Pr-P	0.721	3.10	81.3
La-Nd-P	0.729	2.80	75.4
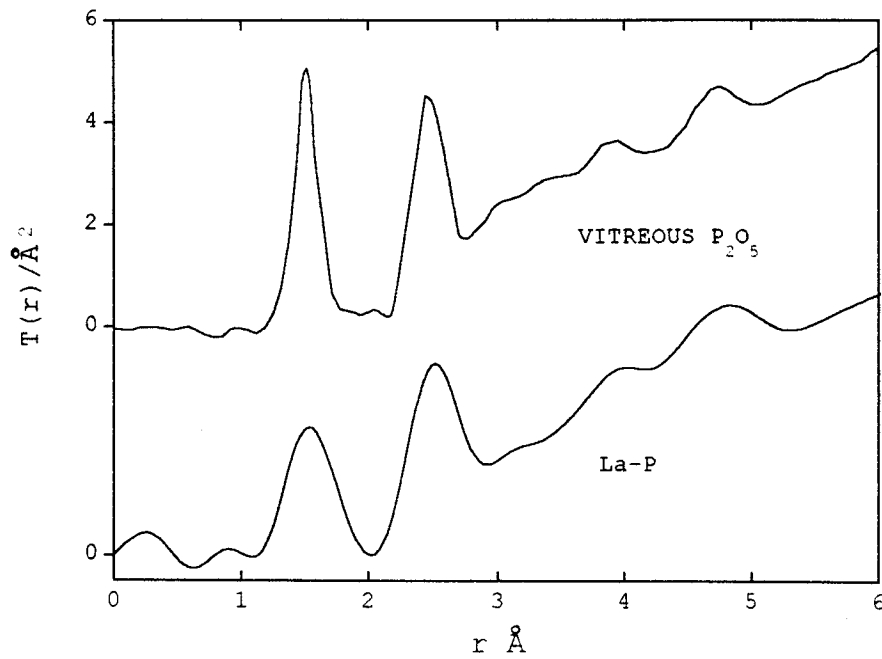
Fig. 5.19a: Comparison of $T(r)$'s of v-P_2O_5 (after Suzuya et al. [1998] and La-P glass (neutron data)
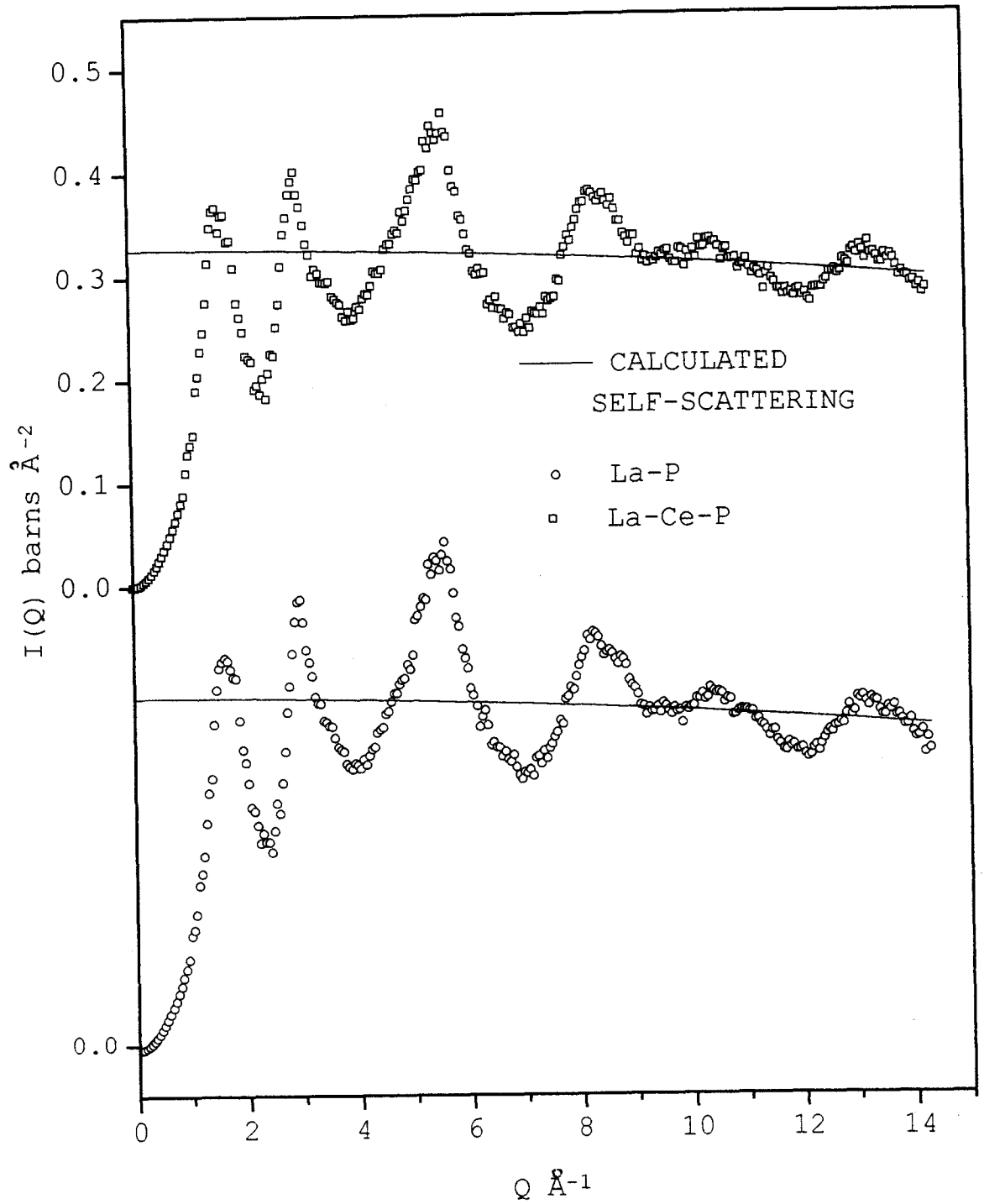
Figure 5.19: Normalized intensity $I(Q)$ of La-P and La-Ce-P glasses (neutron data)
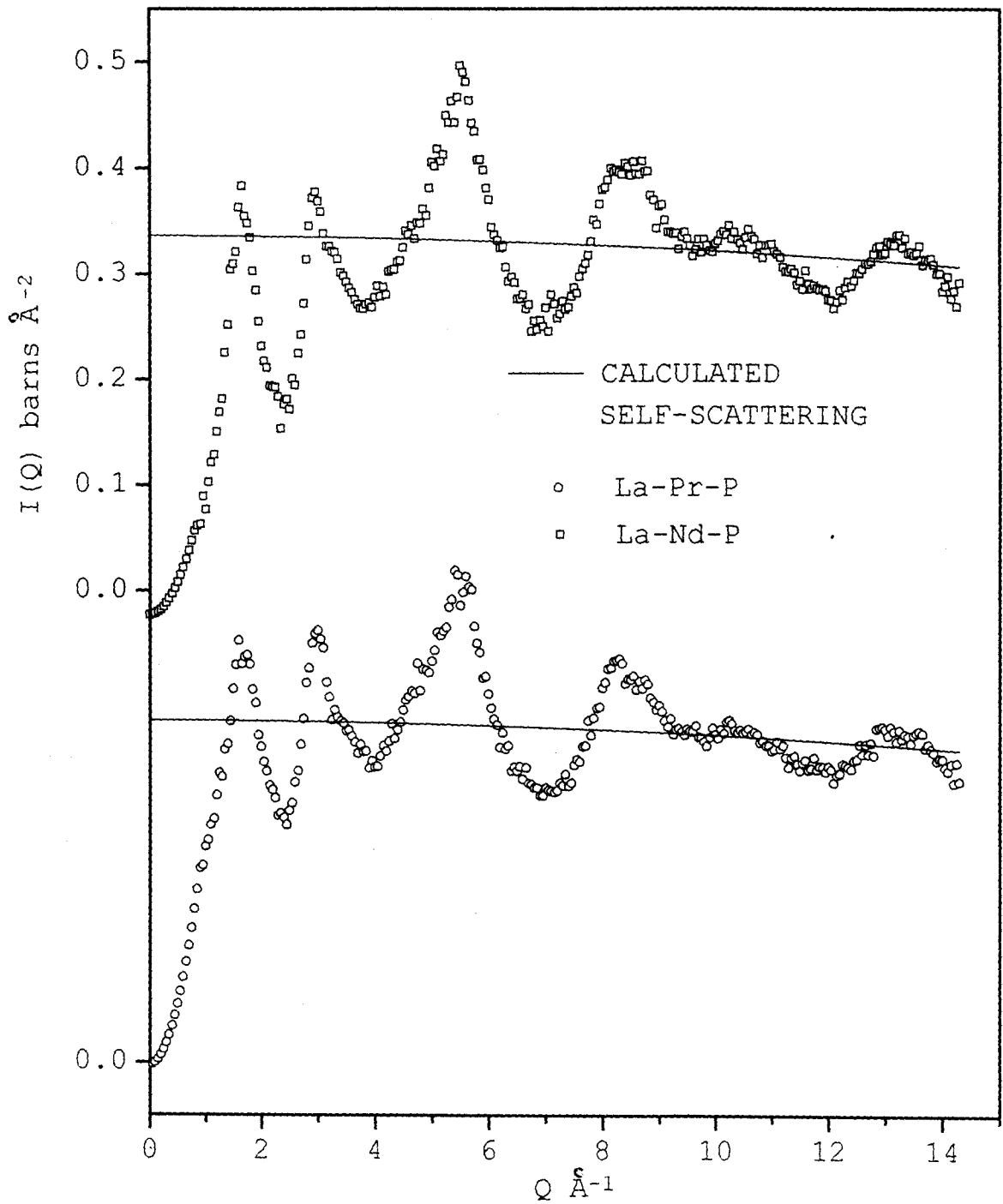
Figure 5.20: Normalized intensity $I(Q)$ of La-Pr-P and La-Nd-P glasses (neutron data)
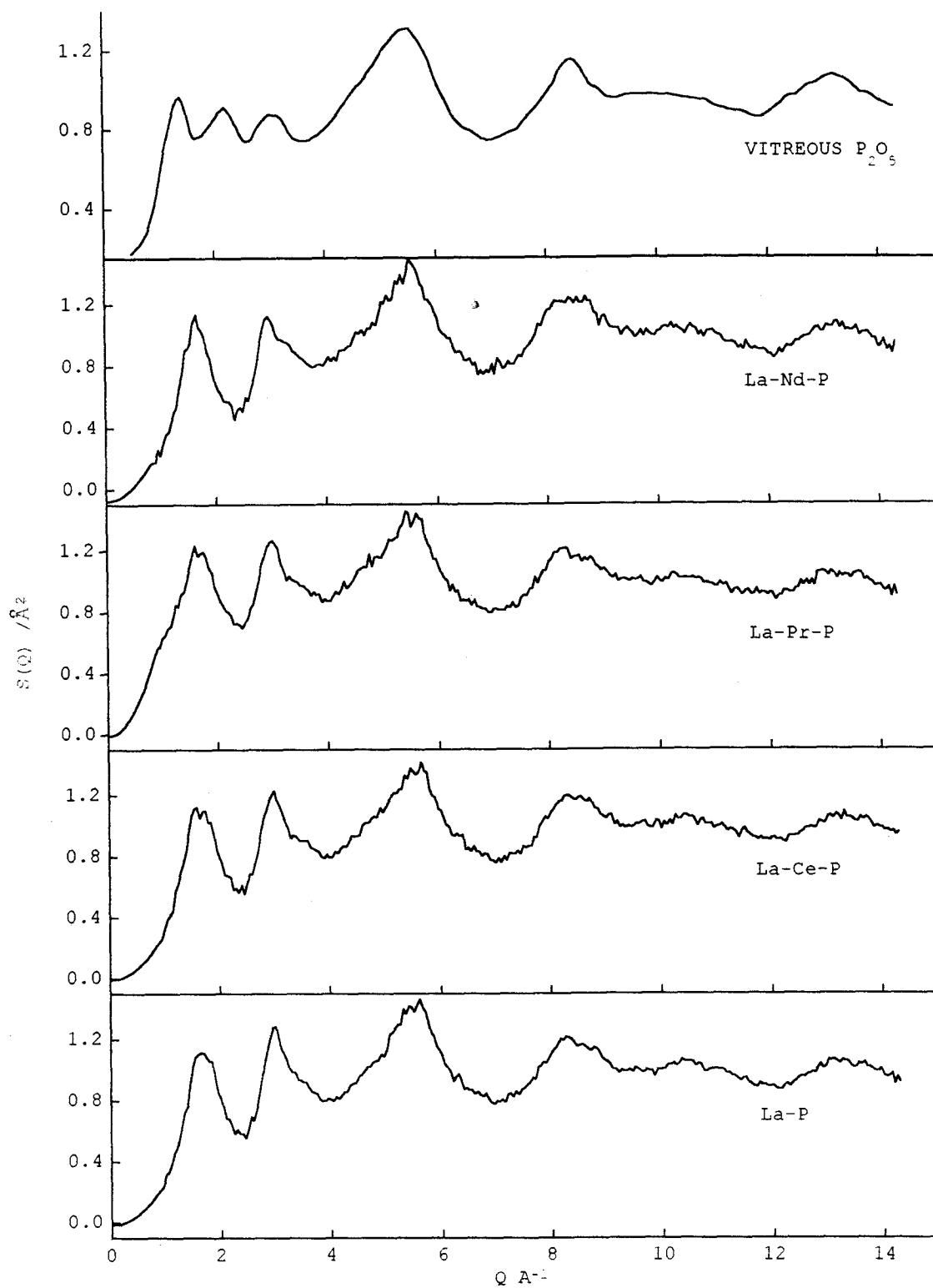
Figure 5.21: Comparison of the neutron structure factor $S(Q)$ of rare-earth phosphate glasses with v-P_2O_5 (after Suzuya et al. [1998])
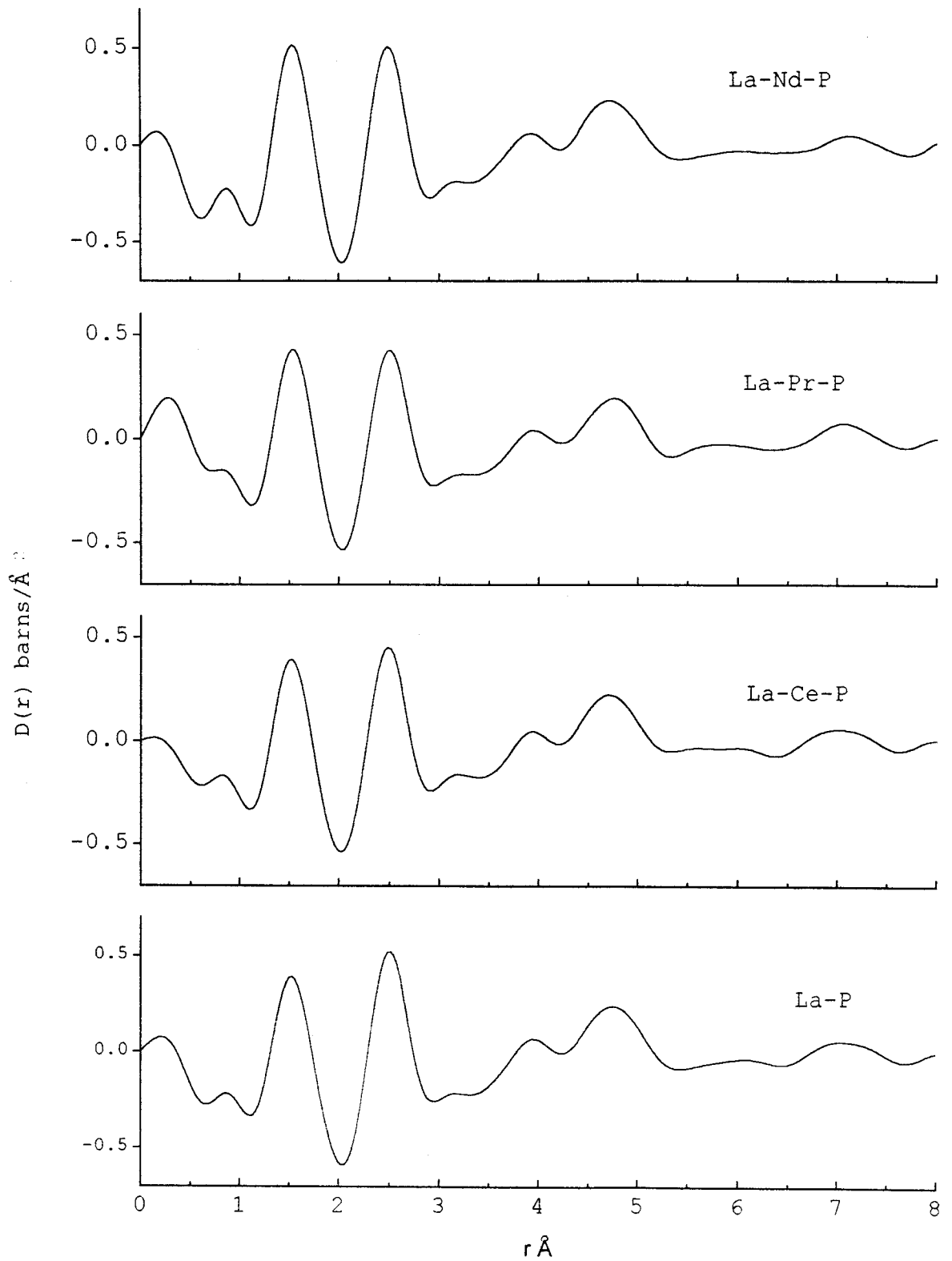
Figure 5.22: Differential correlation function $D(r)$ of phosphate glasses (neutron data)

116
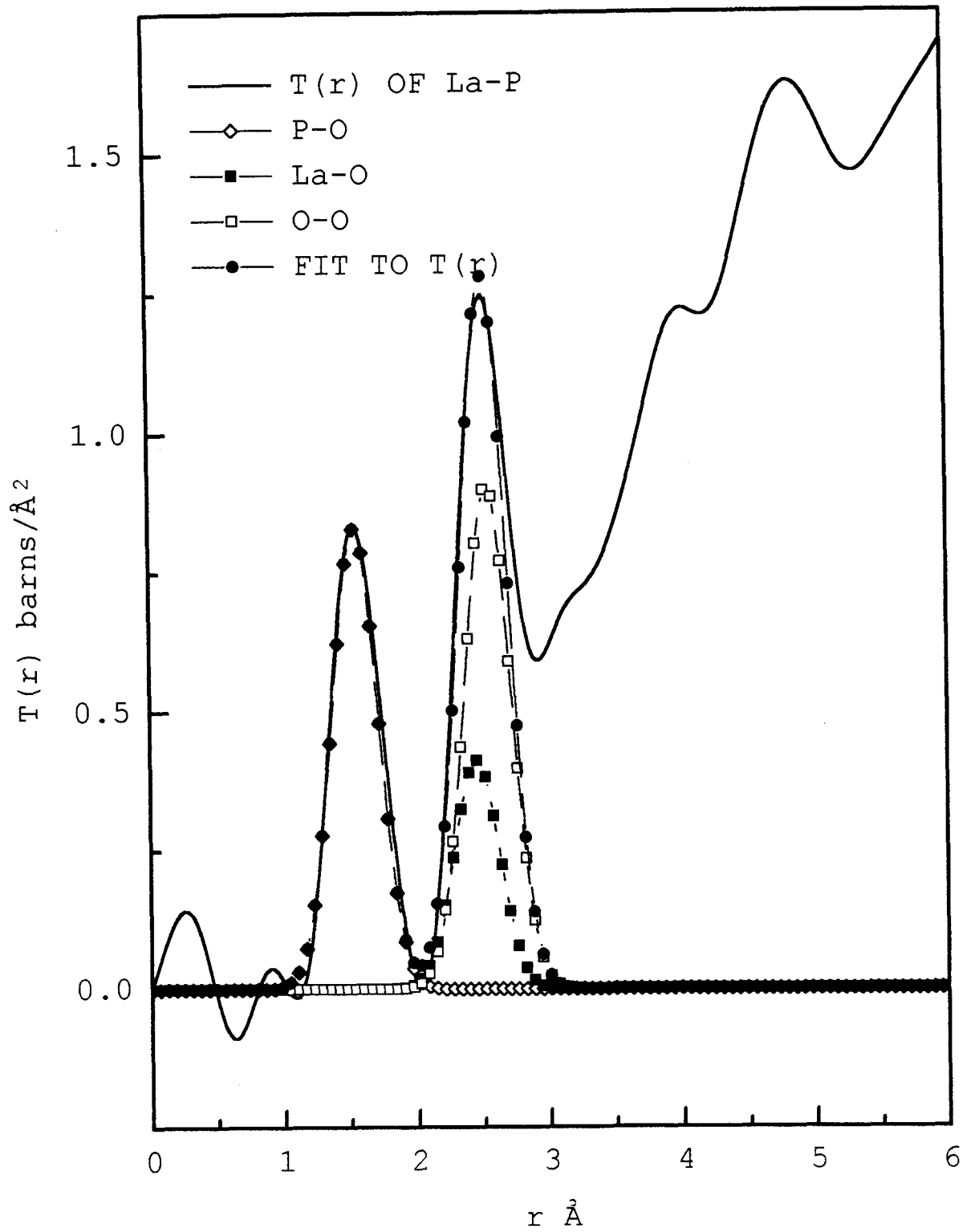
Figure 5.23: Fit to the total correlation function $T(r)$ of La-P glass (neutron data)
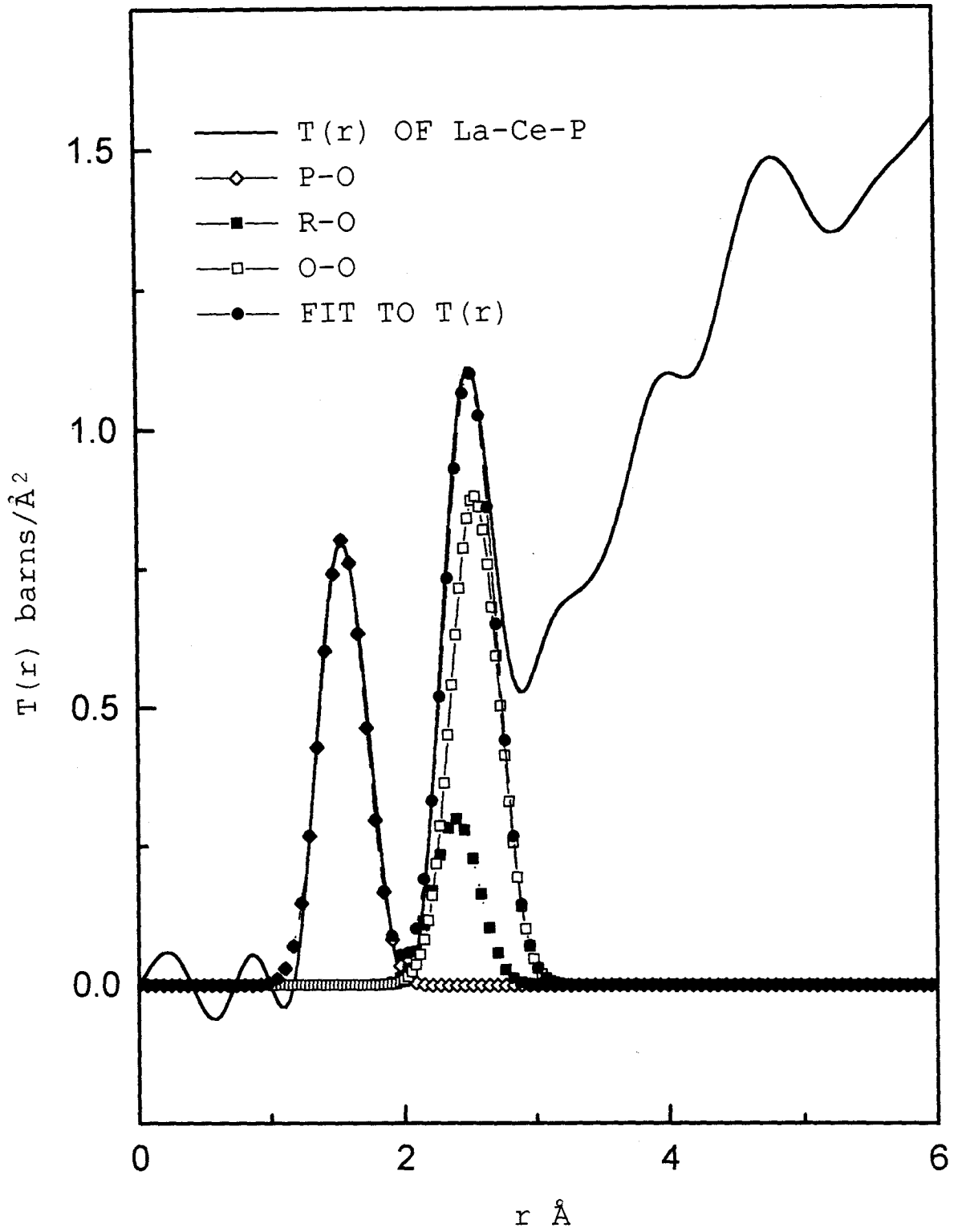
Figure 5.24: Fit to the total correlation function $T(r)$ of La-Ce-P glass (neutron data)
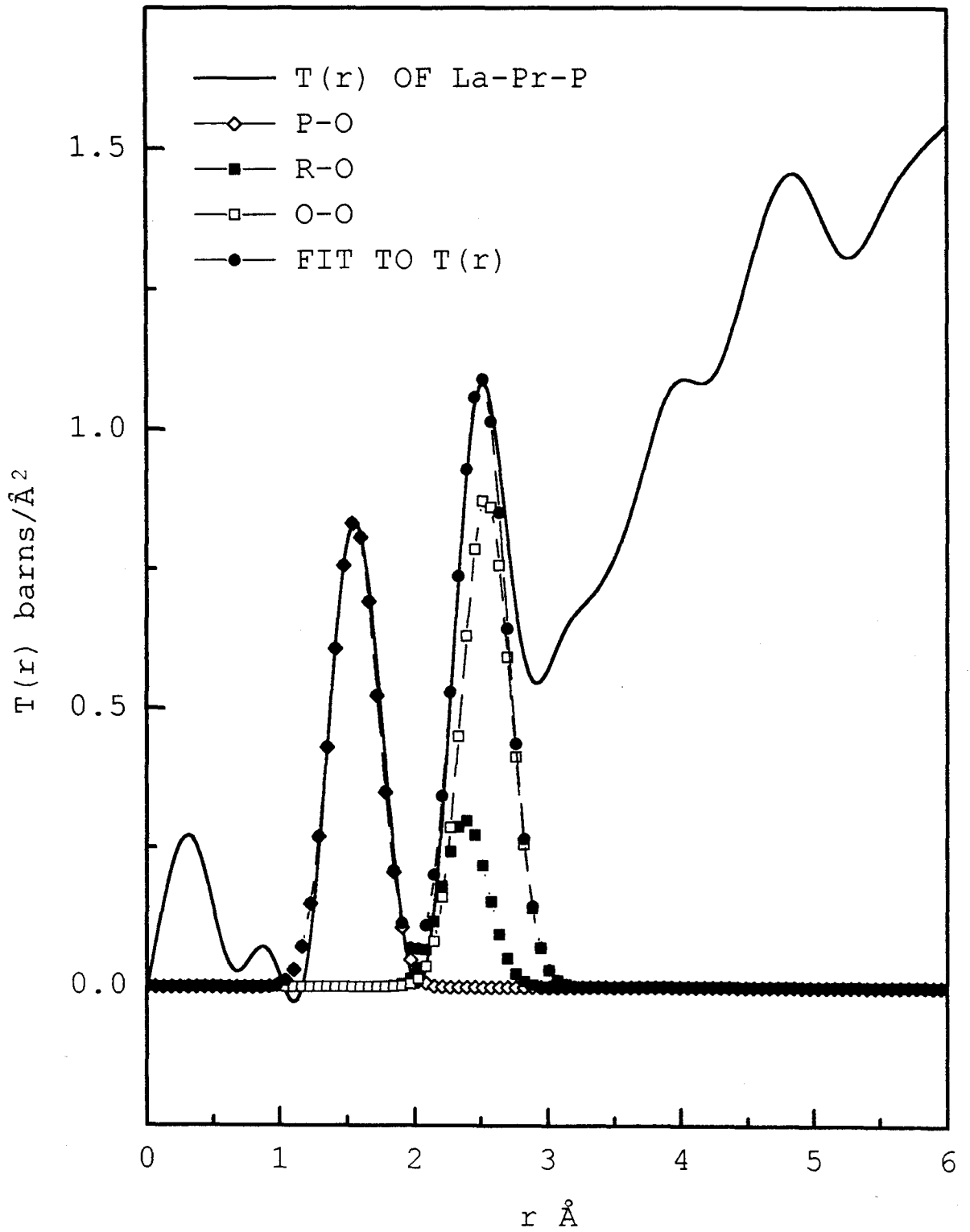
Figure 5.25: Fit to the total correlation function $T(r)$ of La-Pr-P glass (neutron data)
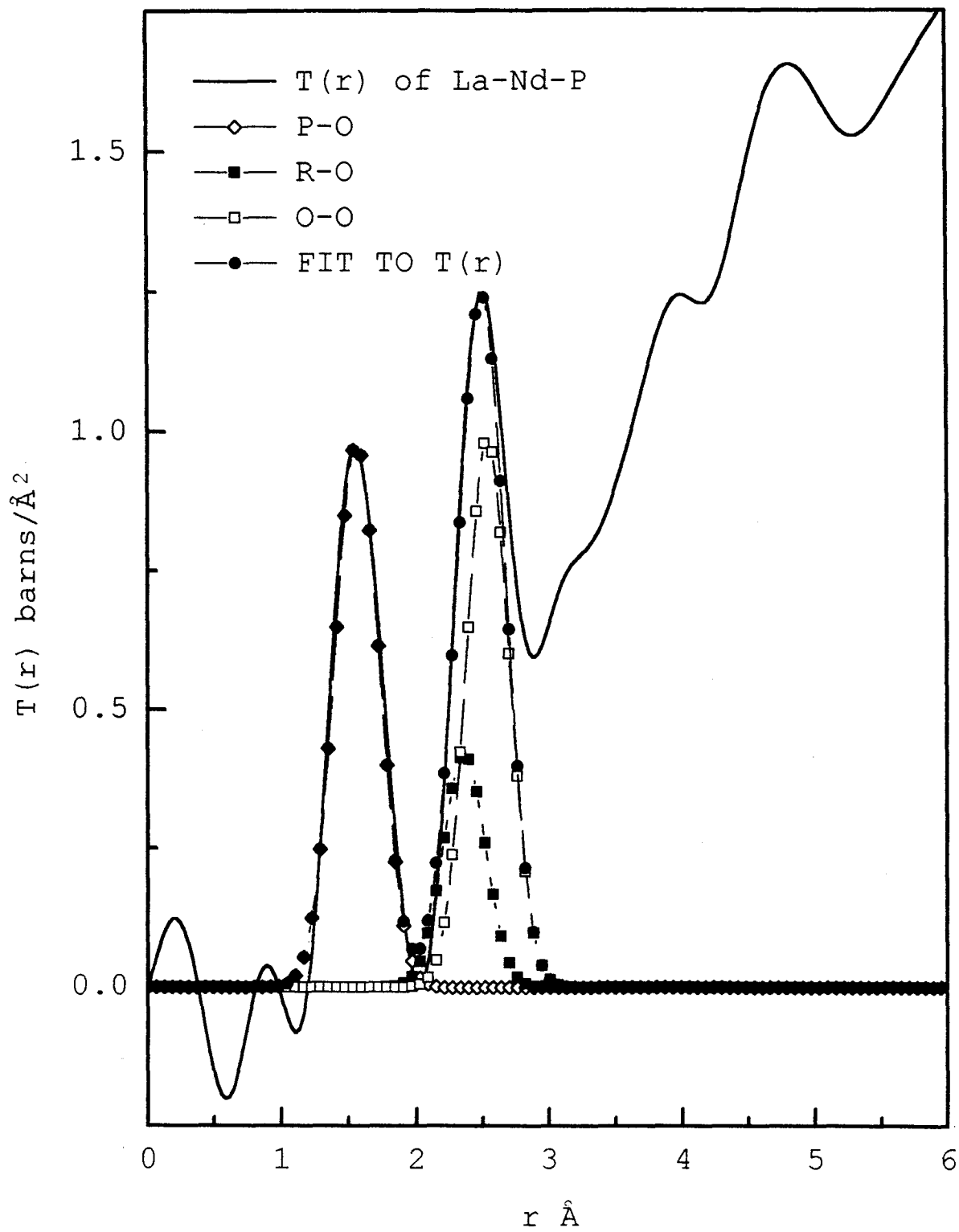
Figure 5.26: Fit to the total correlation function $T(r)$ of La-Nd-P glass (neutron data)
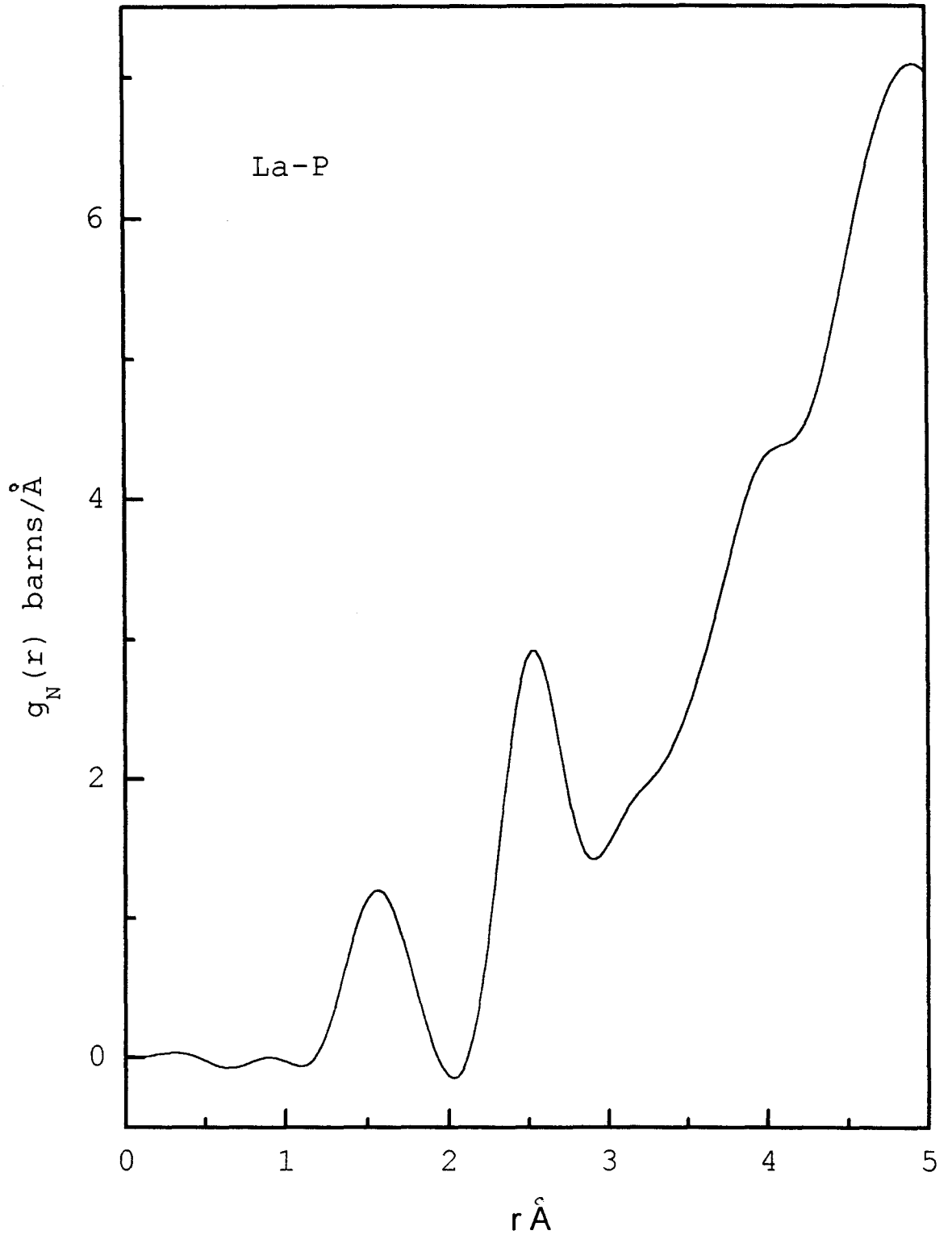
Figure 5.27: Radial Distribution Function $g(r)$ of La-P glass (neutron data)
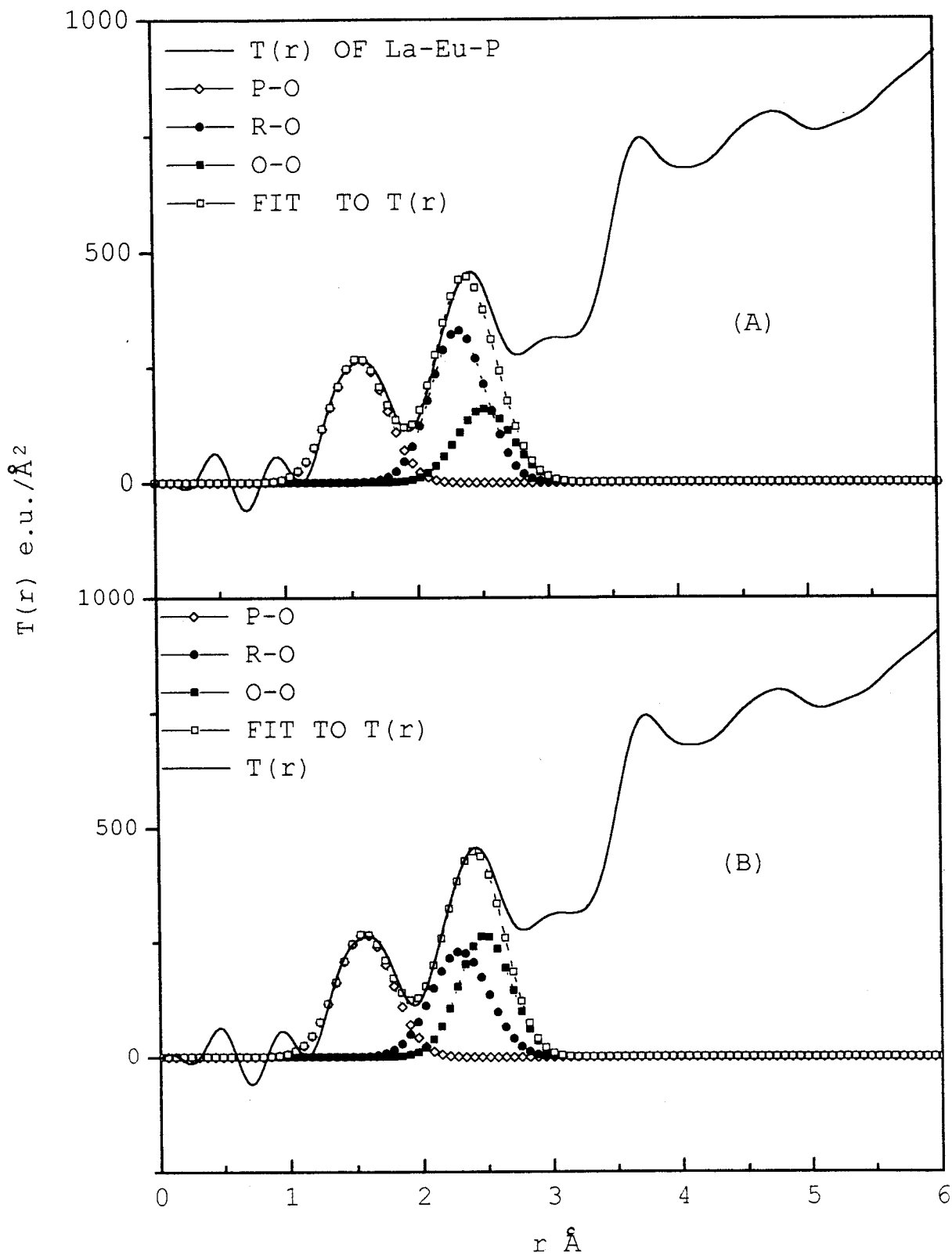
Fig. 5.27 b: Gaussian fits to the second peak in $T(r)$ in which $n_O(O)$ is 4 [Fig.(A)] or 6 [Fig.(B)]

Table 5.6: Coordination numbers and correlations of the phosphate glasses from neutron diffraction data

Sample	Correlation	r Å	FWHM (Å)	$n_j(k)$
La-P	P-O	1.545(5)	0.17	3.97(19)
	La-O	2.44(2)	0.17	7.29(52)
	O-O	2.53(2)	0.172	4.34(32)
Ce-P	P-O	1.545(5)	0.17	3.72(17)
	R-O	2.39(2)	0.17	8.08(71)
	O-O	2.53(2)	0.18	4.01(30)
Pr-P	P-O	1.553(4)	0.174	4.14(20)
	R-O	2.38(2)	0.17	6.70(59)
	O-O	2.53(2)	0.18	3.88(29)
Nd-P	P-O	1.561(5)	0.164	4.57(37)
	R-O	2.36(1)	0.16	6.87(49)
	O-O	2.53(1)	0.16	4.52(39)

N.B.: Figures in parentheses refer to errors in the last decimal place(s).

Table 5.7: Parameters obtained from the combination of X-ray and Neutron correlation functions

Sample	R-O Å	$n_R(O)$	O-O Å	$n_O(O)$
La-P	2.44	7.41	2.51	4.29
La-Pr-P	2.38	8.63	2.51	3.86
La-Nd-P	2.36	8.18	2.51	4.36
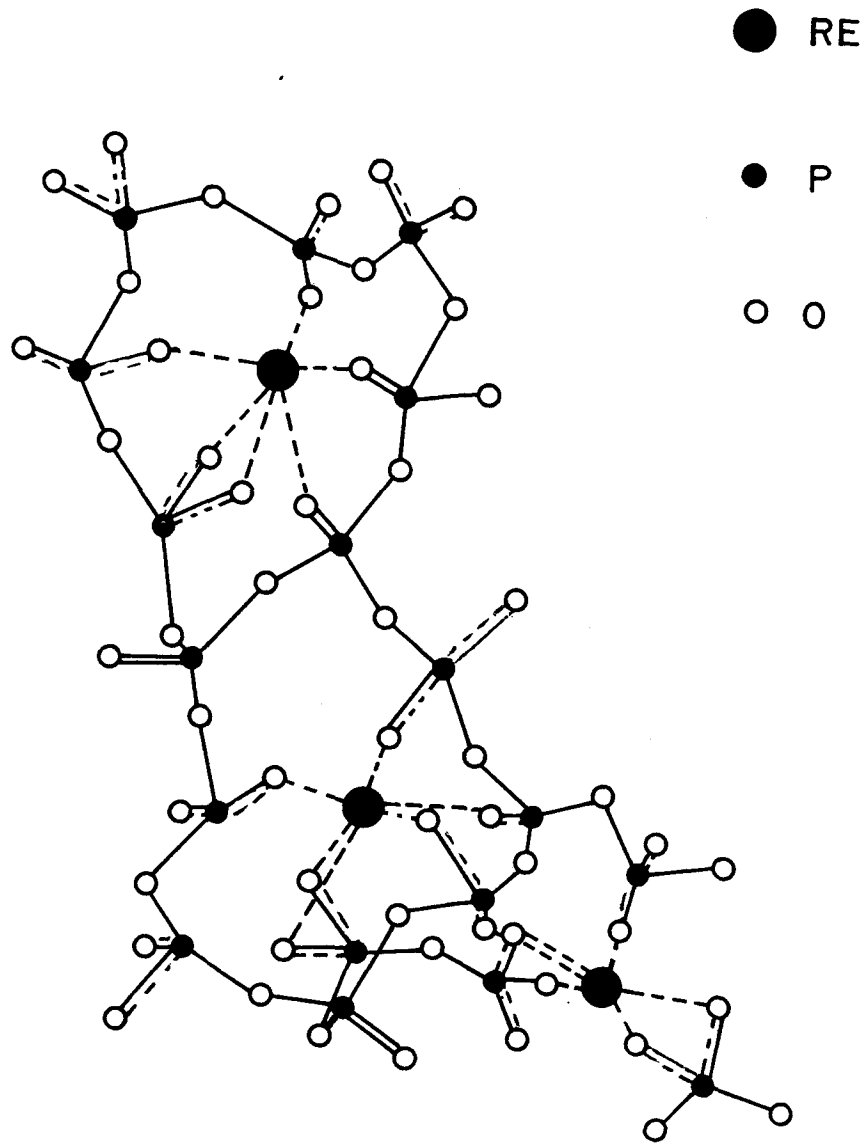
Figure 5.28: Schematic 2-D model of the network of the rare-earth phosphate glass (− − − indicates partial bonds)

Table 5.8: Peak positions in the IR spectra of rare-earth phosphates

Sample	Peaks in IR spectra								
	1	2	3	4	5	6	7	8	9
La-P	476	738	-	931	-	-	1177	1242	-
La-Ce-P	487	733	-	933	-	-	1183	1242	-
La-Pr-P	489	736	-	933	-	-	1183	1247	-
La-Nd-P	484	736	-	933	-	-	1185	1249	-
La-Eu-P	484	733	-	931	-	-	1183	1242	-
La-Tb-P	481	731	-	934	-	-	1192	1245	-
La-Ho-P	474	728	-	926	-	-	1180	1225	-
La-Er-P	476	728	-	931	-	-	1177	1227	-
20SmP	481	-	775	921	-	1059	-	1254	-
La-Dy-P	484	733	778	932	1020	1071	-	1254	1306
Dy-P	496	738	778	926	1015	1069	-	1254	1308

N.B.: Glasses 20SmP, La-Dy-P and Dy-P do not contain aluminium.

Figure 5.29: IR spectra of binary rare-earth glasses
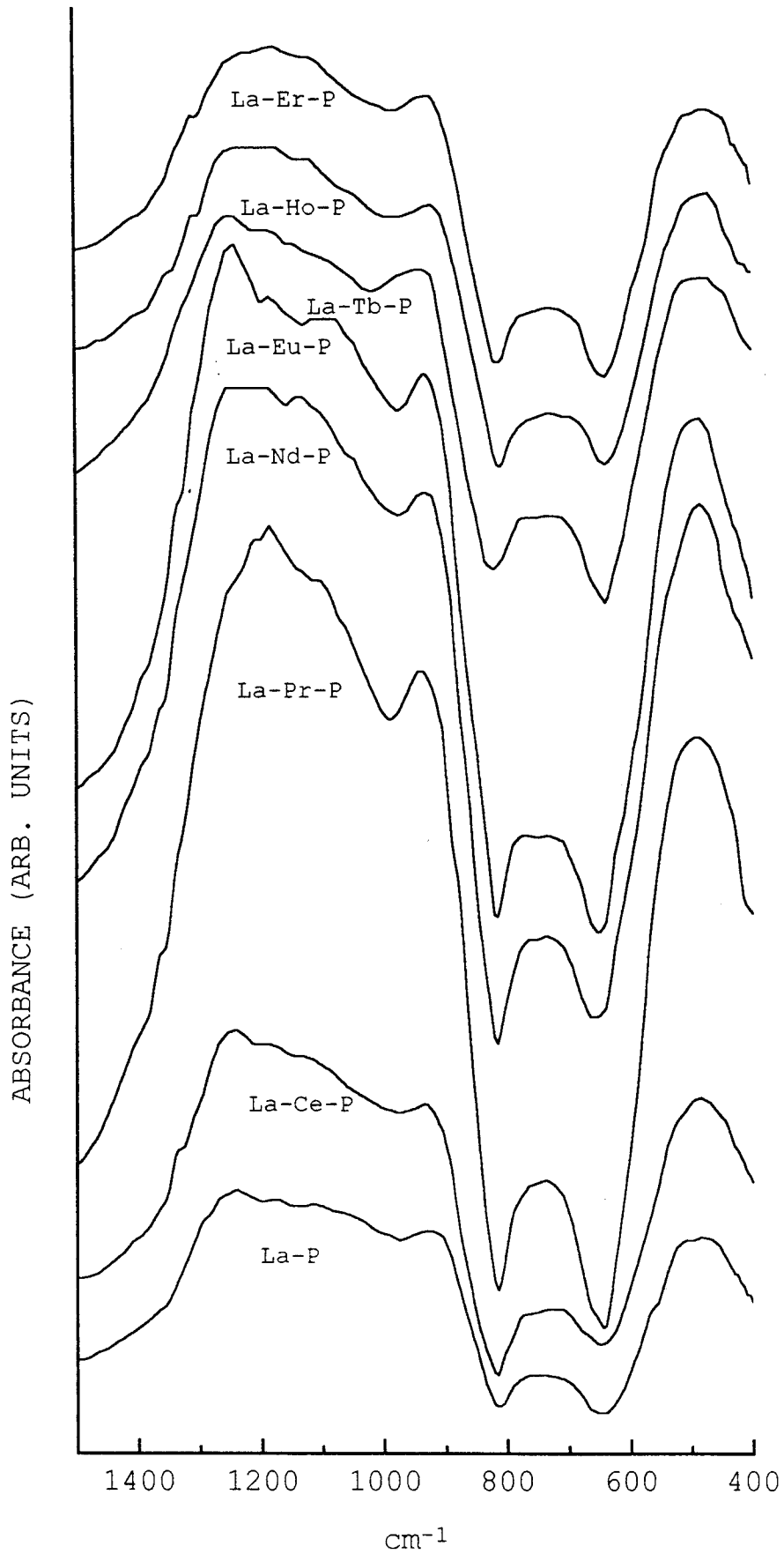
Figure 5.30: IR spectra of rare-earth glasses containing Al_2O_3

Table 5.9: Comparison of IR absorption frequencies with the reported values

Vibrational mode	Frequency range(cm^{-1})		Remarks
	Reported	Observed in this system	
$(PO_4)^{3-}$	500[6] 487, 455[7] 525[3]	476-496	Basic unit is PO$_4$ tetrahedron
ν_s P-O-P	690-790[2] 725-760^a[3] 780[7] 770[5]	731-778	Observed in metaphosphates a - generally observed in cyclic metaphosphates due to P-O-P stretching
ν_{as} P-O-P	850-1050[2] 890-930^b[3] 940^c[4] ≈ 900 [5]	921-924	b Presence of pyrophosphate units c Presence of chains
ν_{as} PO$_3$	985[3]	1015, 1020	Not observed in aluminophosphates

128

Table 5.9 contd.

ν_s PO$_2$	1090-1170[2] 1050[3]	1050-1071[e]	e Presence of PO$_2$ groups in chain phosphates e Not observed in aluminophosphates
ν_s PO$_3$	1115[2] 980-1115[7]	1115	Bond is more ionic compared to the groups that give rise to a band at 1177Å^{-1}
ν_s PO$_3$	1195[3]	1177-1192	Chain end groups
ν_s PO$_2$	1240-1310[2] 1280[3] 1260[1]	1225-1254	
P=O	1320[1]	1306-1308	Presence of P-O bonds

References to Table 5.9

1. Mierzejewski, A., Saunders.G.A., Sidek, H.A.A. and Bridge, B.; *J. Non-Cryst. Solids,* **104,** (1988), 323-332

2. Exarhos, G.J., Miller, P.J. and Risen, W.M. Jr.; *J. Chem. Phys.,* **60,** (1974), 4145

3. Montagne, L., Palavit, G., Mairesse, G., Draoui, M., Aomari, K. and Saidi Idrissi, M.; *Phys. Chem. Glasses,* (1997), **38**(1), 15-20

4. Berul, S.I. and Voskresenskaya, N.K. Russ, *J. Inorg. Chem.,* (1968), **13**(2), 218

5. Corbridge, D.E.C. and Lowe, E.J., *J. Chem. Soc.,* (1954), 493.

6. Nakamoto, K., *Infrared spectra of inorganic and coordination compounds.* (Wiley, New York. 1963)

7. Ananthamohan, C., Hogarth, C.A., Theocharis, C.R. and Yeats, D.: *J. Mater. Sci,* (1990), **25,** 3956-3959

1180 cm^{-1} ($\nu_s - PO_3$) reveals that the PO_2 groups are slowly replaced by PO_3 end groups. This is an indication of the fact that the chain length decreases and the network gets further modified. A small amplitude feature at 930 cm^{-1} indicates the presence of pyrophosphate groups.

A maximum at 1254 cm^{-1} shows a downward shift in frequency after addition of Al_2O_3. This is likely to be produced by asymmetric stretching of two non-bridging oxygens on each tetrahedron. Modifier cations tend to occupy sites near the intermediate position between these non-bridging oxygens (Fig.5.28). The frequency mode and the PO_2 bond angle thus get affected due to the interaction between the non-bridging atom and metal ion. Hence the change in modifier content has an effect on the position of this band (at 1254 cm^{-1}).

The band at 1308 cm^{-1} disappears after the addition of Al_2O_3 indicating that the P=O bond is involved in the interaction between Al and P_2O_5 leading to delocalization of the double bond. This suggests that the added Al forms an integral part of a metaphosphate structure [Brow et al. (1994)].

5.5.5   A.C. susceptibility

A.C. susceptibility measurements were made on these samples in the temperature range 80 K to 273 K. The experimental details of these measurements were as described in Chapter 3. Sample sizes were as shown in Table 5.10. A non-zero offset value was observed in the measurements due to the mismatch of coils. This was measured for every sample and subtracted from the measured susceptibility value. Figures 5.31 and 5.32 show the (1/T) dependence of the ratio of susceptibilities at temperature T with the susceptibility at room temperature. The samples having La^{3+}, Ce^{3+} have a weak temperature dependence of a.c. susceptibility. However, the Er^{3+} containing glass showed large values of susceptibility. The other samples show an increase in the susceptibility value with a decrease in temperature although the trend does not follow the Curie law (non-linear). The sample containing Ford et al. (1994) maintain that glasses containing La, Eu, Sm, Gd and Nd have little or no

magnetic moment interactions even though the latter two have strong moments. The reason and origin for the non-Curie behaviour in the glasses studied here is at present not known.

5.5.6 UV/visible absorption properties

The UV/visible spectra of these glasses were measured with the spectrometer whose details have been given in Chapter 3. The frequency range was 200 nm to 1000 nm. The samples were in the form of plates of thickness in the range 0.09 cm to 0.39 cm [Table 5.11]. The optical absorption spectra normalized to the thickness of La-P sample are shown in Figs. 5.33 to 5.36. Absorption bands are well defined for some glasses. In the optical absorption spectrum, absorption bands are well defined. This is often observed in , rare-earth trivalent ions owing to the weak influence of the local field on the $4f$ states [Mcclure et al. (1963)]. Below 300 nm there is a strong increase in the background absorption due to the existence of very dense energy levels in the spectral region [Caspers et al. (1970), Weber et al. (1972)] as well as the intrinsic absorption of the phosphate glass. This limits the resolution of the absorption bands in the UV region.

The energy levels of the rare-earth ions determine the character of the optical absorption spectrum. The absorption band maxima of the glasses are compared in Tables 5.12 to 5.17 with the reported data for rare-earth ions doped in crystals, glasses and aqueous solutions. Optical spectra of rare-earth ions arise mainly from electric and magnetic dipole transitions between the ground and f^n states electronic configuration. Maxima in the spectra reported for these ions correspond to transitions from the ground state to the excited states belonging to the $4f^{10}$ configuration. The similarity between the measured spectral wavelengths and the transitions related to rare-earth ions confirms that the bands observed for these glasses are characteristic of the rare-earth ions. In the spectra shown here. the samples La-P. La-Ce-P. La-Tb-P and La-Eu-P were found to have very high absorption in the and no absorption in the visible. These glasses would be excellent candidates for UV filters as well as band pass filters in the visible. have sharp absorption bands in the visible region together with high

absorption in the UV region.

In the case of semiconducting amorphous chalcogenides, the optical absorption coefficient α, changes rapidly for photon energies comparable to that of the band gap, E_g, giving rise to an absorption edge. It can be shown that, for there glasses, the absorption coefficient $\alpha(\nu)$ follows the following proportionality:

$$\nu\alpha(\nu) \propto (h\nu - E_0)^2 \tag{5.3}$$

where ν is the optical frequency, E_0 is the optical band gap. Thus, the plot of $(\alpha h\nu)^{1/2}$ versus $h\nu$ should be linear and the value of the optical band gap can be calculated. An attempt was made to calculate E_0 of these glasses from the above formalism. The values of E_0 calculated from the plots of $(\alpha h\nu)^{1/2}$ versus $h\nu$ are shown in Table 5.18.

5.6 Conclusions

Metaphosphate glasses having members of the lanthanide series were prepared and characterized using diffraction, optical spectroscopic and magenetic measurement methods. The FSDP in the diffracted intensity functions indicated that the rare-earth atoms act as network modifiers. The total correlation functions obtained from both X-rays and neutrons show that the P atom is surrounded by 4 oxygen atoms at an average distance of 1.55 ± 0.01Å. In this compositional range, the network is mainly made up of Q^2 tetrahedra due to the presence of rare-earth cations as modifiers. The $T(r)$'s obtained from both X-rays and neutrons were used together to calculate the co-ordination number $n_R(O)$ and $n_O(O)$. These were found to be in the range of 6 to 8, and 4 respectively. The second maximum in the X-ray $T(r)$ displays a shift in its position due to the 'lanthanide contraction'. The fits to the second peak in $T(r)$ which gave $n_O(O)$ values of about 4 support the model of a relatively open structure of corner-linked tetrahedral units with the inter-tetrahedral bond angle in the range $143°$ to $148°$. The FTIR studies on these glasses support the findings from diffraction i.e. the presence of PO_4 tetrahedra in the network. A 2-D projection of a 3-D hand-built model of

the structure of the glass has also been presented. The A.C. magnetic susceptibility measurements in the range 82 K to 300 K on these glasses show that there is an increase in the susceptibility value with a decrease in temperature. The UV/Visible absorption measurements in the range 200 nm to 1000 nm show that the absorption spectra is mainly due to the rare-earth atoms present in the glass. All these glasses have been found to be excellent UV absorbers while some of them have the additional property of 90% transmission in the visible.

Table 5.10: Samples used for the a.c. susceptibility measurements

Sample	Length (cm)	Width (cm)	Mass (mg) ± 0.2
La-P	1.5	0.5	101.5
La-Ce-P	1.6	0.4	101
La-Pr-P	1.5	0.5	101.1
La-Nd-P	1.4	0.5	101.2
La-Eu-P	1.5	0.4	101.2
La-Tb-P	1.4	0.4	101.1
La-Ho-P	1.4	0.4	101
La-Er-P	1.5	0.4	101.9
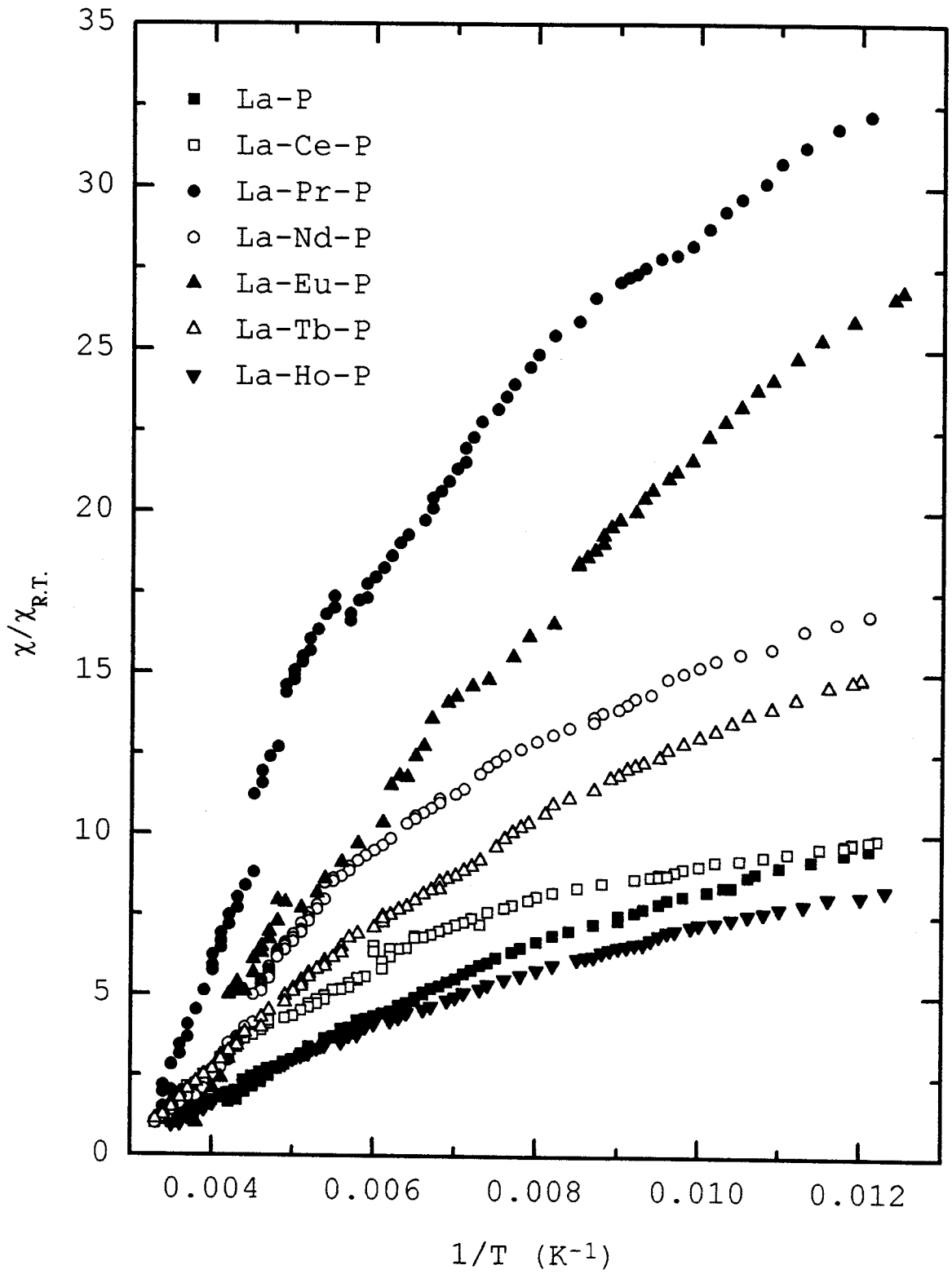
Figure 5.31: Plot of $\chi/\chi_{R.T.}$ versus 1/T of rare-earth phosphate glasses

136
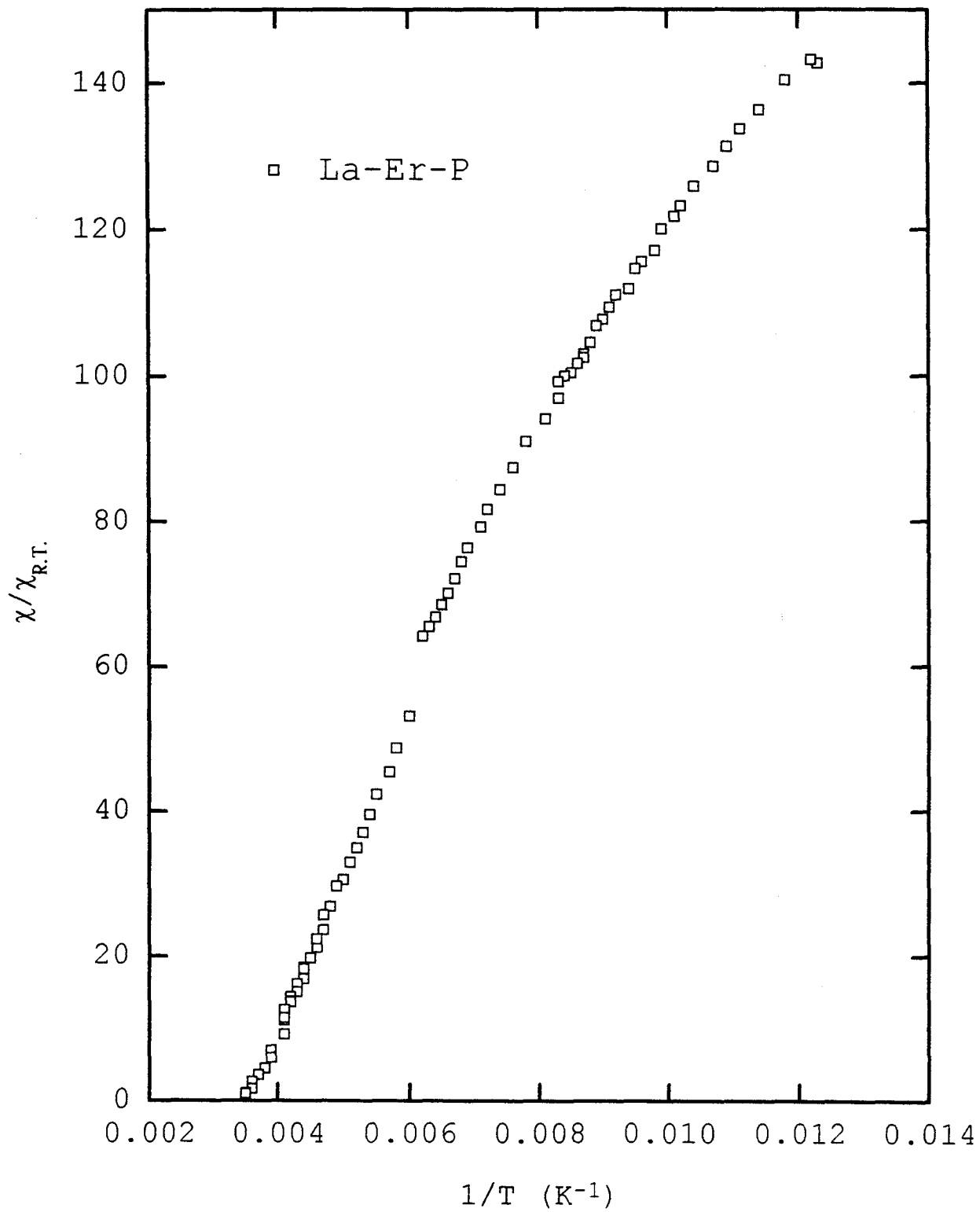
Figure 5.32: Plot of $\chi/\chi_{R.T.}$ versus 1/T of La-Er-P glass

Table 5.11: Thickness of the samples used in UV/visible absorption measurements

Sample	t (cm)
La-P	0.093
La-Ce-P	0.098
La-Pr-P	0.096
La-Nd-P	0.09
La-Eu-P	0.115
La-Tb-P	0.129
La-Ho-P	0.148
La-Er-P	0.187
La-Dy-P	0.397
20SmP	0.263
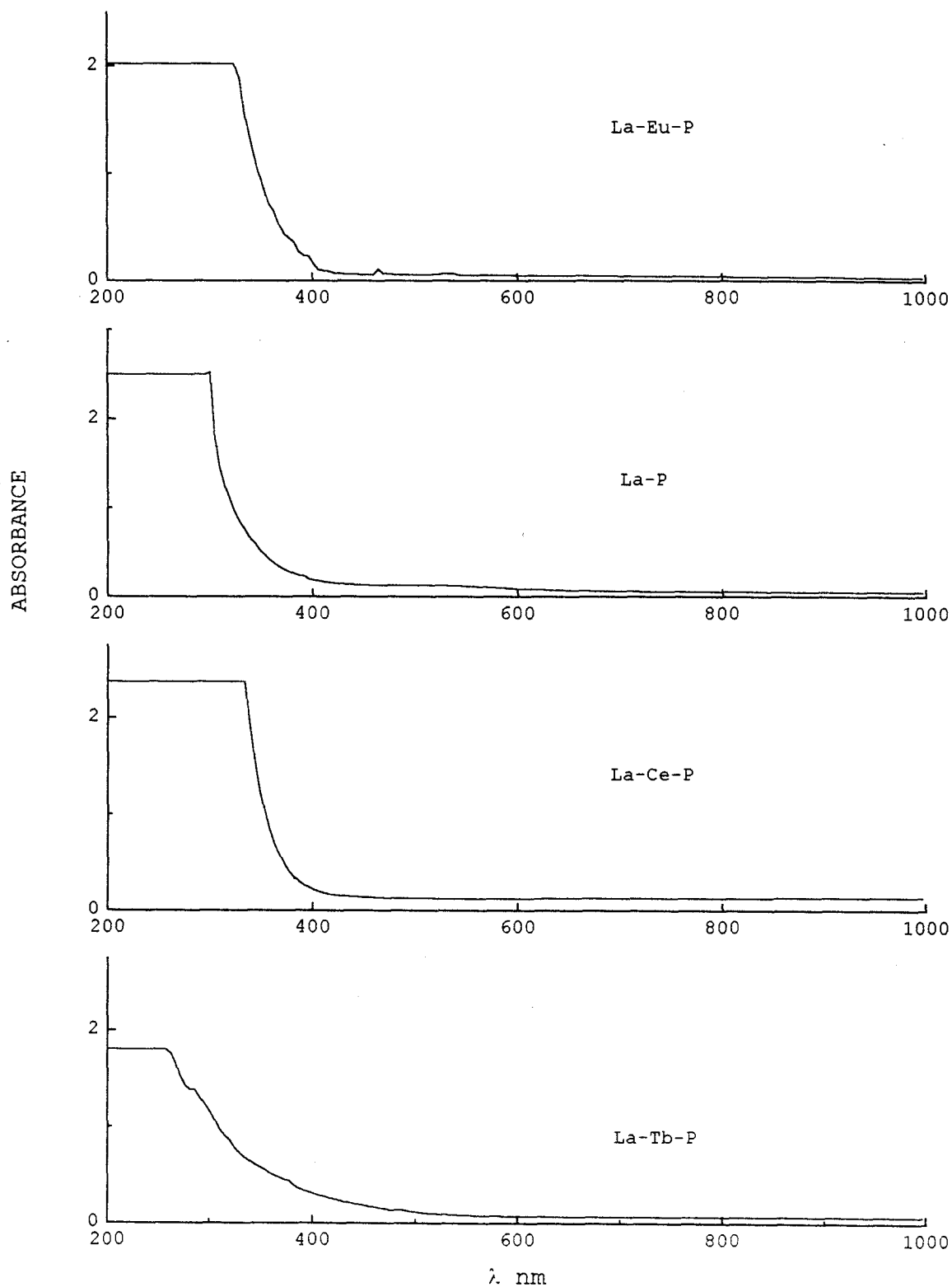
Figure 5.33: UV/Visible absorption spectra of La-P, La-Ce-P, La-Eu-P and La-Tb-P glasses
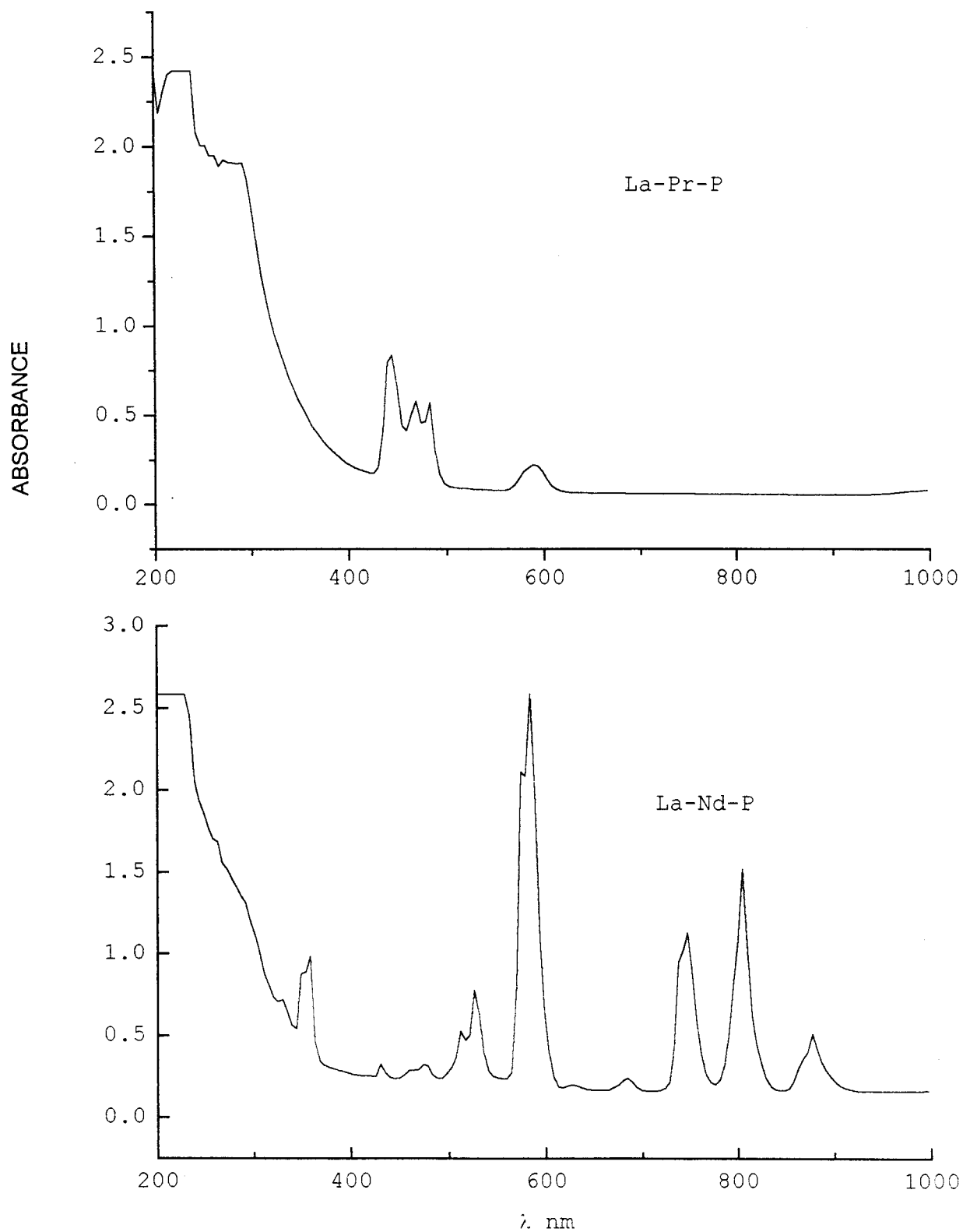
Figure 5.34: UV/Visible absorption spectra of La-Pr-P and La-Nd-P glasses
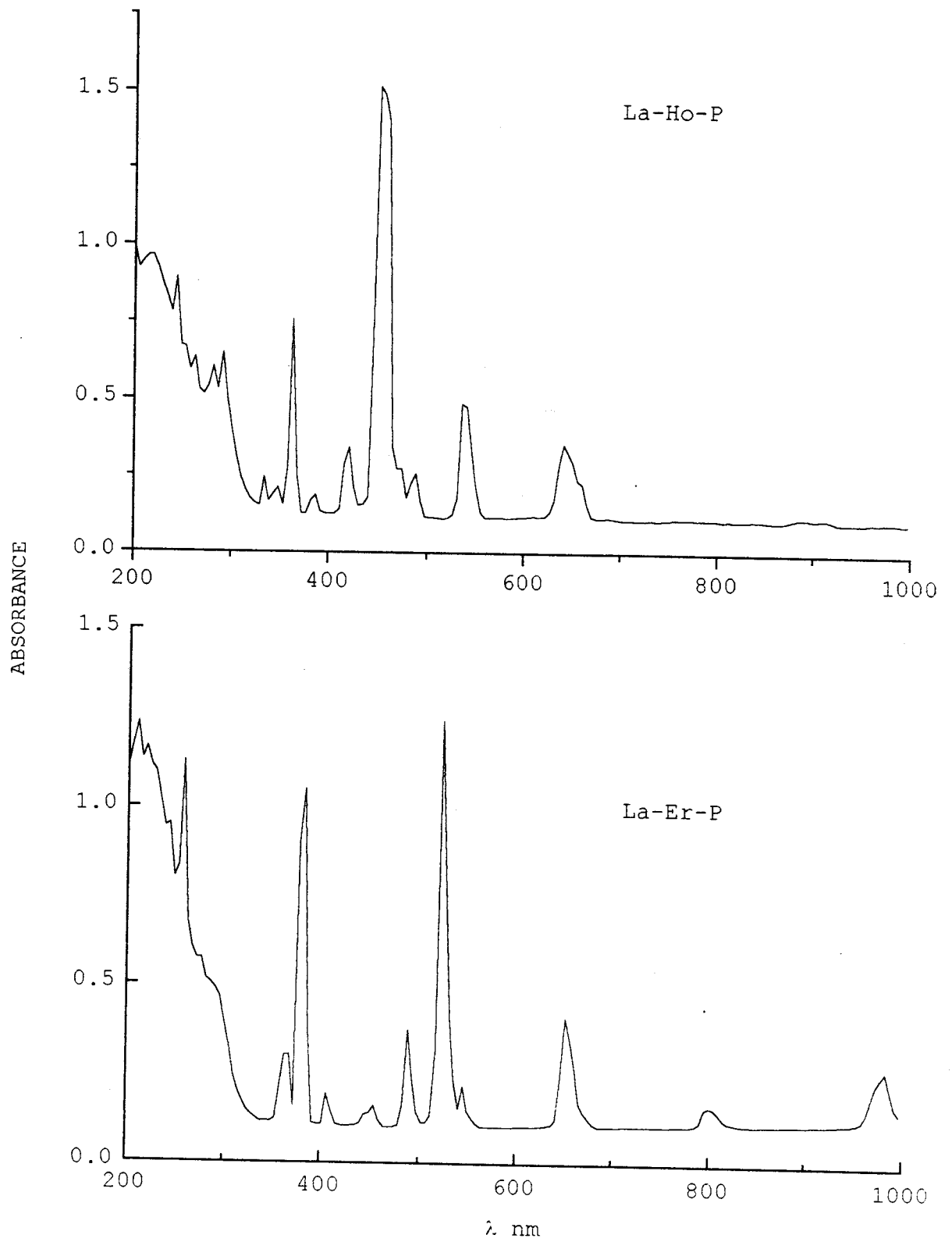
Figure 5.35: UV/Visible absorption spectra of La-Ho-P and La-Er-P glasses
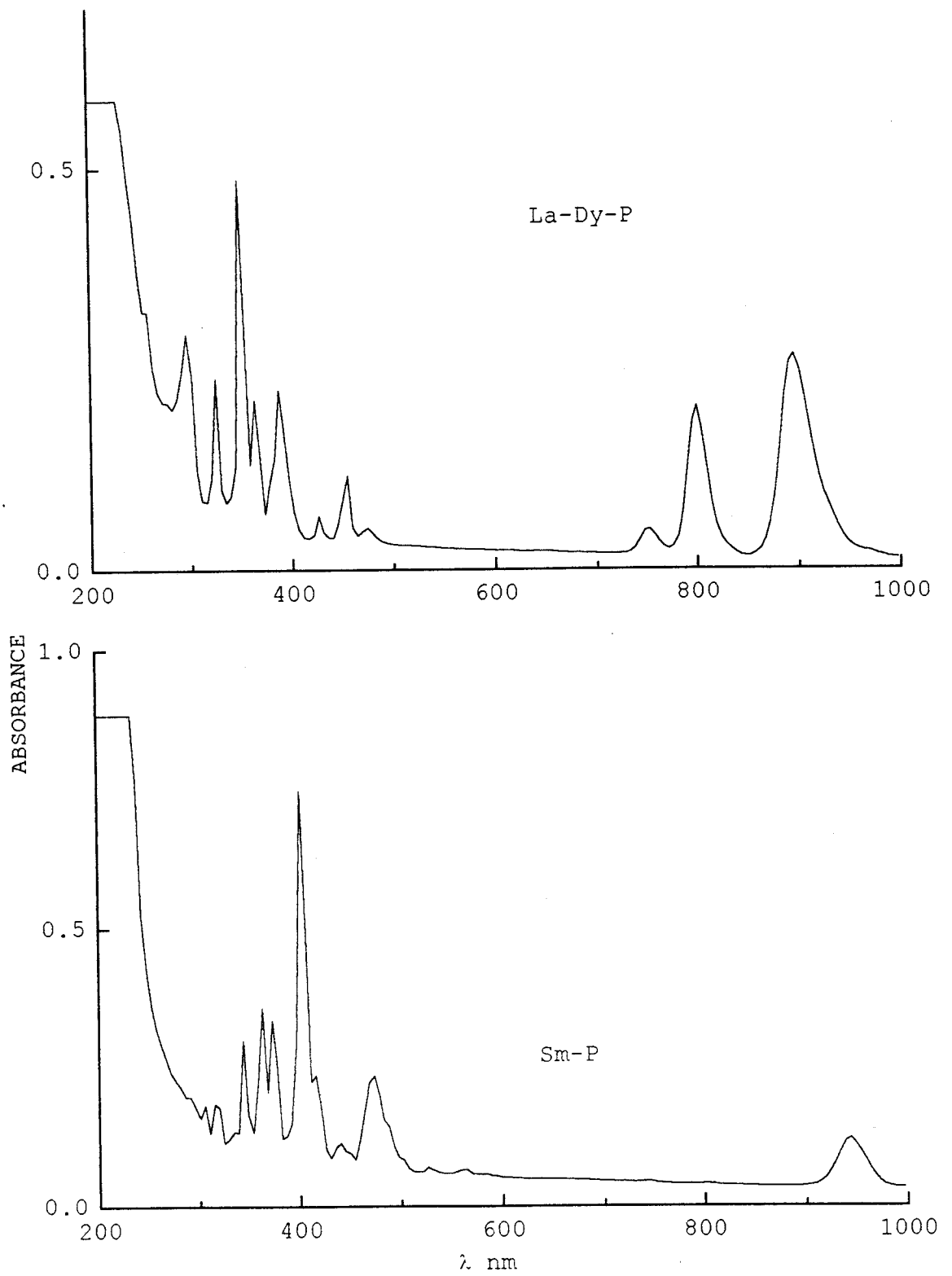
Figure 5.36: UV/Visible absorption spectra of Sm-P and La-Dy-P

142

Table 5.12: Absorption bands of Praseodymium phosphate glass at room temperature compared with the transitions between the $4f$ electron states of Pr^{3+} in lithium borate glasses [Thyagarajan et al. (1997)])

Transition	Observed	Reported
$^3H_4 \rightarrow {}^1D_2$	590.34	587.16
	554.2	
$^3H_4 \rightarrow {}^3P_0$	482.55	481.62
$^3H_4 \rightarrow {}^3P_1$	471.34	467.1
$^3H_4 \rightarrow {}^3P_2$	443.92	441.6

Table 5.13: Absorption bands of Neodymium phosphate glass at room temperature compared with the transitions between the $4f$ electron states of Nd^{3+} in $LaCl_3$ crystal [Rajnak (1965)])

Transition	Observed	Reported
	223.98	
	295.77	
	329.9	
$^4I_{9/2} \rightarrow \, ^4D_{1/2}$	349.8	352.7
$^4I_{9/2} \rightarrow \, ^4D_{3/2}$	359.1	359.3
$^4I_{9/2} \rightarrow \, ^2P_{1/2}$	432.7	433.6
$^4I_{9/2} \rightarrow \, ^2P_{3/2}, \, ^2D3/2$	475.7	476.78
$^4I_{9/2} \rightarrow \, ^2G_{9/2}$	513.7	518.78
$^4I_{9/2} \rightarrow \, ^4G_{7/2}$	527.4	530.05
$^4I_{9/2} \rightarrow \, ^4G_{5/2}$	583.49	588.9
$^4I_{9/2} \rightarrow \, ^2H_{11/2}$	635.2	633.69
$^4I_{9/2} \rightarrow \, ^4F_{9/2}$	681.9	686.4
$^4I_{9/2} \rightarrow \, ^4S_{3/2}$	740.49	747.9
$^4I_{9/2} \rightarrow \, ^4F_{7/2}$	747.35	752.8
$^4I_{9/2} \rightarrow \, ^2H_{9/2}$	805.3	802.3
$^4I_{9/2} \rightarrow \, ^4F_{3/2}$	875	

Table 5.14: Absorption bands of Holmium phosphate glass at room temperature compared with the transitions between the $4f$ electron states of Ho^{3+} in LaF_3 crystal [Caspers et al. (1970)])

Transition	Observed	Reported
$^5I_8 \rightarrow \; ^3K_6, ^3F_4, \; ^3D_2$	334.26	332.5
$^5I_8 \rightarrow \; ^5G_3, \; ^3L_9$	347.97	343.5
$^5I_8 \rightarrow \; ^3H_6, \; ^3H_5$	361.1	360.2
$^5I_8 \rightarrow \; ^5G_4$	385.98	384.7
	419.62	
	453.27	
	475.7	
	489.4	
$^5I_8 \rightarrow \; ^5S_2, \; ^5F_4$	538.49	537.7
$^5I_8 \rightarrow \; ^5F_5$	641.43	641.2

Table 5.15: Absorption bands of Erbium phosphate glass at room temperature compared with the transitions between the $4f$ electron states of Er^{3+} in $LaCl_3$ crystal [Rajnak (1965)])

Transition	Observed	Reported
$^4I_{15/2} \rightarrow {}^3K_{15/2}$	363.55	363.6
$^4I_{15/2} \rightarrow {}^4G_{1/2}$	379.12	380.76
$^4I_{15/2} \rightarrow {}^2H_{9/2}$	408.41	408
$7\ ^4I_{15/2} \rightarrow {}^4F_{5/2}$	455.14	453.18
$^4I_{15/2} \rightarrow {}^4F_{7/2}$	489.4	490.03
$^4I_{15/2} \rightarrow {}^2H_{11/2}$	523.05	524.76
$^4I_{15/2} \rightarrow {}^4S_{3/2}$	547.35	546.72
$^4I_{15/2} \rightarrow {}^4F_{9/2}$	650.77	659
$^4I_{15/2} \rightarrow {}^4I_{9/2}$	800.9	809.6
$^4I_{15/2} \rightarrow {}^4I_{11/2}$	982.86	989

Table 5.16: Absorption bands of Samarium phosphate glass at room temperature compared with the transitions between the $4f$ electron states of Sm^{3+} in aqueous solution [Carnell et al. (1968)])

Transition	Observed	Reported
	305.4	
	316.03	
$^6H_{5/2} \rightarrow {}^4D_{7/2}$	344.5	343.6
$^6H_{5/2} \rightarrow {}^4P_{5/2}, {}^6P_{5/2}$	363.9	361.6
$^6H_{5/2} \rightarrow {}^6P_{7/2}$	373.7	373.8
$^6H_{5/2} \rightarrow {}^6P_{3/2}$	403.8	400.8
$^6H_{5/2} \rightarrow {}^6P_{5/2}, {}^4P_{5/2}$	415.8	415.8
$^6H_{5/2} \rightarrow {}^4G_{9/2}$	439.86	440.5
$^6H_{5/2} \rightarrow {}^4I_{11/2}$	473	473.9
$^6H_{5/2} \rightarrow {}^4F_{3/2}$	529.9	529.4
	944.85	

Table 5.17: Absorption bands of Dysprosium phosphate glass at room temperature compared with the transitions between the $4f$ electron states of Dy^{3+} in aqueous solution [Carnell et al. (1968)])

Transition	Observed	Reported
$^6H_{15/2} \rightarrow {}^4H_{13/2}$	298.13	298.5
$^6H_{15/2} \rightarrow {}^4P_{3/2}$	327.4	324.6
$^6H_{15/2} \rightarrow {}^4P_{7/2}$	352.33	350.2
$^6H_{15/2} \rightarrow {}^4P_{5/2}$	365.42	364.9
$^6H_{15/2} \rightarrow {}^4I_{13/2}$	390.34	387.5
$^6H_{15/2} \rightarrow {}^4G_{11/2}$	426.48	427.3
$^6H_{15/2} \rightarrow {}^4I_{15/2}$	455.14	452.4
$^6H_{15/2} \rightarrow {}^4F_{9/2}$	475.7	473.9
$^6H_{15/2} \rightarrow {}^4F_{3/2}$	749.22	754.7
	799.06	
	893.14	

Table 5.18: Optical band gap of rare-earth phosphate glasses

Sample	E_{opt} eV
La-P	2.77
La-Ce-P	2.96
La-Pr-P	2.66
La-Nd-P	2.78
La-Eu-P	2.85
La-Tb-P	2.26
La-Er-P	3.28

Chapter 6

CONCLUSIONS

In this work, two different types of vitreous systems have been considered. The first was a boro-silicate network to which simulated (i.e. non-radioactive) nuclear waste was added. The second was a phosphate host glass bearing a series of lanthanide rare-earth oxides. A summary of the findings and conclusions on each of these two vitreous systems is presented in this chapter.

6.1 Nuclear-Waste Glasses

In order to study the effect of included waste on the host network, glasses with high concentrations (upto 25 wt%) of simulated nuclear waste were studied together with the basic boro-silicate host glass. The method of the RDF was used for this study. X-ray diffraction patterns recorded on the nuclear-waste glasses were used to identify those systems that were vitreous and that were considered 'acceptable' from leaching studies. The vitreous glasses were examined by neutron diffraction together with the basic glass. These studies revealed that the basic units of the host glass (SiO_4 tetrahedra and BO_3 triangles) remain intact after the addition of waste cations. This conclusion was drawn from the position and the area of the first maximum in the T(r) which is a sum of the Si-O and B-O correlations of the basic units in the host glass. This feature remains unchanged after the addition of waste

oxides. The added waste cations occupy interstices of the network thereby modifying it in the medium-order range (2 Å to 10 Å). A detailed study of the other features in the total correlation function is difficult on account of the large number of overlapping component correlations arising from the multicomponent nature of the samples. Some of these may be resolved using high resolution diffraction data collected to high values of Q_{max}. The Reverse Monte Carlo method may also be employed in the separation of some of these component functions. The question of the bonding of the waste to the host network has not been addressed in this work. However, the possibility of a weak ionic link between the oxygen atoms of the network and the waste cations cannot be excluded. Thus, surface leaching by aqueous solvents might occur under suitable conditions. From this study, a model of the microscopic structure of glass was built by constraining the inter-tetrahedral bond angles to the range 135° to 170° as well as the Si-O-B angular range to 140° to 170°.

Radiation effects due to the radioactivity of the actual waste are likely to damage the structure and have not been considered in this work. Irradiation with high energy gamma-rays and other ionizing particles could be used in understanding the change in the network that would occur after several years of radiation damage caused by the waste cations in the glass. Many applications of these oxides which were considered as waste oxides a decade ago have been proposed [Physics Education (1988)]. The gamma radiation from this waste may be used to irradiate vegetables, grains, other foods and for sterilization of various medical and pharmaceutical products. Gamma rays from this waste have also been used to convert the chemical structure of thin plastic sheets to 'Omniderm' to substitute for human skin. The latter can be used for improved recovery of ruptured or burnt skin. Vitrification of this waste for such applications would thus permit the manufacture of mobile radiation sources for the above mentioned uses. It may be noted that although these glasses have been found to be mechanically and chemically stable, their storage in geological structures that are considered stable may at some future date be prone to damage by unforeseen earthquake and volcanic activity. Should such events occur, the possibility of these long-lived radioactive species

entering the biosphere cannot be ruled out. Even though the probability of occurence of such calamities is low, it points to the need for more than one method of permanent storage of highly-active long-lived nuclear waste to be considered.

6.2   Rare-earth Phosphate Glasses

Rare-earth phosphate glasses with good mechanical strength, transparency, stability and inertness were prepared. These had the general formula

$$(R_2O_3)_{0.2}(P_2O_5)_{0.8}(Al_2O_3)_{0.05} \quad \text{and} \quad (R_2O_3)_x(P_2O_5)_{1-x}$$
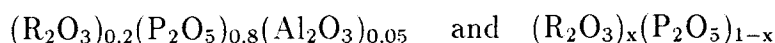
where x = 0.2 and 0.25 and R stands for La, Ce, Pr, Nd, Sm, Eu, Tb, Dy, Er or Ho. In each sample the symbol R represents both La and one other rare-earth from this series. The densities of these glasses were found to increase with increase in atomic number. This was attributed to the fact that there is a change in the mass of the sample with very little change in the its specific volume. The vitreous nature of the samples was confirmed with preliminary X-ray diffraction. Compositional analyses of the samples using chemical methods and Neutron Activation Analysis showed that there was a small (4 to 10%) discrepancy in composition between that which was expected from the starting mixtures and found from the analyses.

The XRD measurements using MoK_α radiation showed the basic unit of this glass to be a PO_4 tetrahedron with $n_P(O)$ of 4 ± 0.07 and a P-O bond distance of 1.55 ± 0.01 Å. The compositional dependence of the intensity function $i(Q)$ was monitored from the variation in the peak height of the FSDP for the Sm containing glasses. The decrease in the intensity of this feature with increase in Sm concentration was attributed to this cation's role as a network modifier. The effect known as the 'lanthanide contraction' was observed in the correlation functions through the downward shift in position of the second maximum with increasing atomic number of the rare-earth atom. This shift was caused by the R-O correlation which was one of the constituents of the second maximum in $T(r)$.

The scattering length dependence of FSDP from $i(Q)$ obtained using ND measurements confirmed the network modifying role of the rare-earth cations. The total correlation function $T(r)$ of each glass yielded an $n_P(O)$ coordination number of 4.01 ± 0.06 and an $r(P-O)$ distance of 1.55 ± 0.01 Å. The second maximum yielded the $n_O(O)$, $n_R(O)$ coordination numbers in the ranges 3.8 to 4.3 and 7 to 8 respectively. The respective $r(O-O)$, $r(R-O)$ distances were 2.53 Å and in the range 2.44 Å to 2.26 Å. The total correlation functions obtained using both XRD and ND were combined to calculate the $n_R(O)$ and $n_O(O)$ coordination numbers as both these functions had different weights. The numbers so obtained agree well with those obtained from Gaussian fits to the features in T(r) within 15%.

The separation of higher order component correlations such as P-P, R-P etc. was not possible through the combination of X-ray and neutron diffraction data. Also, the particular value of Q_{max} used in these diffraction measurements did not permit the further separation of component correlation functions. Thus the X-ray and neutron diffraction data both support a model of this glass in which the network is predominantly made up of tetrahedral PO_4 units with two corners being shared (Q^2 units) and an inter-tetrahedral angle in the range 143° to 148°. The rare-earth cations form oxygen polyhedra and occupy 'holes' or spaces in the network. These cations are likely to be partially ionically linked to their oxygen neighbours.

Techniques such as EXAFS, Energy Dispersive X-ray Diffraction or measurements with high values of maximum momentum transfer ($Q \approx 30$ Å^{-1}) would all be useful in the separation of R-O and O-O correlations which was not possible in the measurements described here. Anomalous scattering experiments on some of these samples with three different incident wavelengths could be used to extract the correlations R-R, R-X and X-X where R is a rare-earth and X is a non-rare-earth atom. Resonance scattering of X-rays using wavelengths on either sides of the L_{III} absorption edges of rare-earth atoms would have a variation of the atomic scattering factor which could be of much value in separation of partial correlations. Computer modelling techniques such as molecular dynamics and Monte Carlo are needed in the further elucidation of these structures.

IR results showed that the glasses doped with different rare-earths have similar structures in which the basic unit is a PO_4 tetrahedron. These data also indicated that added aluminium plays role of a network modifier in a similar way to that of rare-earth ions and also helps in making this system stable and inert as evidenced by its excellent resistance to atomospheric moisture.

UV/Visible absorption measurements on these glasses found that all of them are good UV absorbers. Four samples namely, La-P, La-Ce-P, La-Tb-P and La-Eu-P had high UV absorption with almost no absorption in the visible range. The absorption peaks in the spectra when compared with the reported data were found to originate from the transitions from the ground state to the excited states belonging to the $4f^{10}$ configuration. More detailed analyses of the spectra are required and would help in understanding the immediate structural environment of the rare-earth ion in the matrix and thus the lasing properties of some of these glasses. Those members of the series having no absorption in the visible are potentially very good candidates for use as optical fibres. All members could be used as good UV filters.

The a.c. susceptibility measurements in the range 82 K to 300 K indicated that the glasses are paramagnetic in this range. Their behaviour at temperatures lower than 82 K would be of use in understanding the possible interaction between these rare-earth cations. More detailed measurements of their magnetic properties as a function of temperatures lower than 77 K are needed as also further analyses to explain the non-linear behaviour of susceptibility in the temperature range measured here.

X-ray and neutron diffraction techniques play a vital role in the determination of glass structure and are unique in the type of information they obtain. However, it is important to understand their limitations and consider these during the interpretation of the results. The need for many different techniques in the examination of the structures of disordered materials is thus not only desirable but also necessary. It has been shown in this work that despite five different methods which probe the structure, only some general findings may be

had with regard to long-range structures. Computer modelling techniques such as molecular dynamics are important in this respect in that they augment experimental findings and permit the extraction of component correlations. However, in some cases these methods may not be true representations of bulk structures as they deal with only a relatively small number of atoms compared to real number densities. Considering the complexity of the structures of disordered materials and the intrinsic limitations of the various techniques that are applied in examining these structures, it is appropriate to quote the words of JOHN GROTE [*Exploratio Philosophica*, II, 229] -

"Advance in knowledge is essentially distinction, not aggregation. Each new particular of knowledge is not an addition to, but a newly observed part of, a previously conceived whole."

References

[1] Alben, R. and Boutron P. (1975), *Science*, **187**, p.430

[2] Bault K.A., Dalton J.T., Hall A.R., Hough A. and Marples J.A.C. (1978) Chemistry Division, AERE (R-9188), Harwell, Oxfordshire

[3] Beall, G.H. (1996) Proceedings of the XVII International congress on Glass (Vol. 1), China Ceram. Soc., p.174

[4] Bhatia A.B. and Thornton D.E. (1970), *Phys. Rev. B*, **2**, p.3004

[5] Bionducci M., Bellissent R., Messa M.P., Piccalugga G., Pinna G. and Bettinelli M. (1995)*J. Non-Cryst. Solids*, **192-193**, P. 36

[6] Blech I.A and Averbach B.L. (1965) *Phys. Rev.*, **137**, p.A1113

[7] Bowron D.T., Newport R.J., Rainford B.D., Saunders G.A. and Senin H.B. (1995), *Phys. Rev. B.* **51**(9), p.5739

[8] Bowron D.T., Saunders G. A.. Newport R.J., Rainford B.D. and Senin H.B. (1996), *Phys. Rev. B*, **53**(9), p.5268

[9] Brow R.K.. Tallant D.R.. Hudgens J.J.. Martin S.W. and Irwin A.D. (1994). *J. Non-Cryst. Solids*, **177**, p.221

[10] Brow R.K. (1996). *J. Non-Cryst. Solids*, **194**, p.267

[11] Brown Jr. G.E., Waychunas G.A., Ponader C.W., Jackson W.E. and McKeown D.A. (1986), *J. Phys.*, (Paris) **47**, C-8, p.661

[12] Cargill, G.S. (1970), *J. Appl. Phys.*, **41**, p.12

[13] Carnell W.T., Fields P.R. and Rajnak K. (1968) *J. Chem. Phys.*, **49**(10), p. 4424

[14] Caspers, H.H. and Rast, H.E. (1970), *J. chem. Phys.*, **53**, p.3208

[15] Cocking, S.J. and Heard, C.R.T. (1965), U.K.A.E.A. Rept. AERE, p.5016

[16] Compton A.H. and Allison S.K. (1935), *X-rays in Theory and Experiment*, Van Nostrand Rainhold, New York

[17] Corbridge, D.E.C. and Lowe, E.J. (1954), *J. Chem. Soc.*, p.493

[18] Covell D.F. (1959), *Anal. Chem.*, **31**(11), p.1785

[19] Cromer D.T. (1965), *Acta Cryst.*, **18**, p.17

[20] Cromer, D.T. and Mann, J.B. (1968), *Acta Cryst.*, **A24**, p.321

[21] Crowder C.E., Otaigbe J.U., Barger M.A., Sammler R.L., Monahan B.C. and Quinn C.J.; (1997) *J. Non-Cryst. Solids*, **210**, p. 209

[22] Cruickshank D.W.J.; (1964) *Acta Crystallographica*, **17**, p.677

[23] Cruickshank D.W.J.; (1964) *Acta Crystallographica*, **17**, p. 679

[24] Day D.E. and Rindone G.E.; (1962), *J. Am. Ceram. Soc.*, **45**, p.487

[25] Durville F.M., Behrens E.G. and Powell R.C.; (1986), *Phys. Rev. B*, **34**, p.4213

[26] Ebert W.L., Hoburg R.F. and Bates J.K.; (1991), *Phys. Chem.Glasses*, Vol.32.4, p.133

[27] Efimov A.M.; (1997), *J. Non-Cryst. Solids*, **209**, p.209

[28] Elliot S.R.; (1992), *J. Phys; Condens. Matter*, **4**, p.7661

[29] Enderby, J.E.; (1968), *Physics of Simple Liquids*, Eds. Temperley, H.N.V., Rowlinson, J.S. and Rushbrooke, G.S. (North-Holland, Amsterdam), Chap. 14

[30] Exarhos, G.J., Miller, P.J. and Risen, W.M. Jr.; (1974),*J. Chem. Phys.*, **60**, p.4145

[31] Finney, J.L. and Wallace, J.;(1981), *J. Non-Cryst. Soilds*, **43**, p.165

[32] Ford P.J., Graham C.D., Saunders G.A. and Senin H.B.; (1994), *J. Mater. Sci. Lett.* , **13**, p.697

[33] Galeener, F.L. and J.C. Mikkelsen, Jr.; (1979), *Solid State Communications*, **30**, p.505

[34] Gaskell P.H.; (1985), *J. Phys.* **46**, C-8, p.3

[35] Goldschmidt, V.M.; (1926), *Skrifter Norske Videnskaps Akad (Oslo). I. Math-naturwiss. Kl. No. 8*, p.7

[36] Greaves, G.N., Gurman, S.J., Gladde, L.F., Spences, C.A., Cox, P., Boatner, B.C., Boatner, L.A. and Jenkinfs, R.N.; (1988), *Phil. Mag. B*, **58**(3), p.271

[37] Greaves G.N.; (1990), Glass Science and Technology, Vol. 4A, ed. D.R. Uhlmann and N.J. Kreidl, Academic Press, London, p.1

[38] Hoppe U., Walter G. and Stachel, D.; (1992), *Phys. Chem. Glasses*, **33**(6), p.216

[39] Hoppe U.; (1996), *J. Non-Cryst. Solids*, **195**, p.138

[40] Hoppe U., Kranold R., Stachel D., Barz A. and Hannon A.C.; (1998), *J. Non-Cryst. Solids*, **232-234**, p.44

[41] Hosemann R., Hentschel M.P., Schmeisser U. and Bruckner R.; (1986), *J. Non-Cryst. Soilds*, **83**, p.223

[42] Hosokawa S., Matsupka T. and Tamura K.; (1991), *J. Phys. C*, **3**, p.4443

[43] Hosono H., Kawamura S. and Abe Y.; (1985), *J. Mater. Sci. Lett.*, **4**, p.244

158

[44] Van Hove L.; (1954), *Phys. Rev.*, **95**, p.249

[45] Jahagirdar P.B., (1992) Private communication

[46] Jiang Y., Zhang J., Xu W. Ma Z., Ying X., Mao H., Mao S. and Li J.; (1986), *J. Non-Cryst. Solids*, **80**, p.623

[47] Johnson P.A.V, Wright A.C. and Sinclair R.N.; (1979), Harwell Report MPD/NBS/113, AERE, Harwell, Oxfordshire.

[48] Jones, G.O.;(1956), *Glass*, Methuen, London, p.119

[49] Knott, P.; (1989), *Glasstech. Ber*, **62**, p.29

[50] Kreidl N.J. and Weyl W.A.; (1941), *J. Amer. Ceram. Soc.* , **24**, p.372

[51] Krogh-Moe J.; (1956), *Acta Cryst.*, **9**, p.951

[52] Krupke W.F., Shinn M.D., Kirchoff T.A., Finch C.B. and Boatner L.A.; (1987), *Appl. Phys. Lett*, **51**, p.2186

[53] Lee, S.W. and J. H. Lee; (1995), *Phys. Chem. Glasses*, **36**(3), p.127

[54] Leadbetter, A.J. and Wright A.C.; (1972), *J. Non-Cryst. Solids*, **7**, p.23

[55] Lorch, E.A.; (1969) *J. Phys.*, **C2**, p.229

[56] Martin S.W.; (1991), *Eur. J. Solid State Inorg. Chem.*, **28**, p.163

[57] Marion J.E.; (1991), *J. Solid State Inorg. Chem.* , **28**, p.271

[58] Matsubara, E., Tamura T., Waseda Y., Zhang T., Inoue A. and Masumoto T.; (1992), *J. Non-Cryst. Solids*, **150**, p.380

[59] McClure, D.S. and Kiss, Z.; (1963), *J. chem. Phys.*, **39**, p.3251

[60] Mcgreevy R.L. and Pustazatai L.; (1988), *Molecular Simulation*, **1**, p.359

[61] McVay G.L and Buckwalter C.Q.; (1980), *Nucl. Tech.*, **51**, p.123

[62] Mierzejewski, A., Saunders G.A., Sidek H.A.A. and Bridge B.; (1988), *J. Non-Cryst. Solids*, **104**, p.323

[63] Milberg M.E.; (1958), *J. Appl. Phys.*, **29**, p.64

[64] Milberg M.E. and C.R. Peters; (1969), *Phys. Chem. Glasses*, p.46

[65] Momiuchi M.; (1986), *J. Phys. Soc. Jpn.*, **55**, p.200

[66] Mountjoy G., Anderson R., Bowron D.T. and Newport R.J.; (1998), *J. Non-Cryst. Solids*, **232-234**, p.227

[67] Mozzi R.L. and Warren B.E.; (1969), *J. Appl. Cryst.*, **2**, p.164

[68] Musinu A., Piccaluga G., Pinna G., Narducci D. and Pizzini S; (1989), *J. Non-Cryst. Solids*, **111**, p.221

[69] Musinu A., Piccaluga G. and Pinna G.; (1990), *J. Non-Cryst. Solids*, **122**, p.52

[70] Norman N.; (1957), *Acta Cryst.*, **10**, p.370

[71] Paalman, N.H. and Pings, C.J.; (1962), *J. Appl. Phys.*; **33**, p.2635

[72] Payne S.A., Elder M.L., Wilke G.D. and Weber M.J.; (1992), *Ceram. Trans.*, **28**, p.253

[73] Pederson L.R., M.T.Thomas and G.L.Mcvay; (1981), *J.Vac.Sci.Technol.*, 18(3) p. 732

[74] Peters P.M. and Houde-Walter S.N.; (1997), *Appl. Phys. Lett.*, **70**(5), p. 541

[75] Phillips, J.C.; (1979), *J. Non-Cryst. Solids*, **34**, p.153

[76] Phillips, J.C.; (1982), *Solid State Physics*: Ehrenreich H., Seitz F., Turnbull D.(Eds.), New York: Academic Press, **37**, p. 93

[77] News and Views, *Physics Education*, January-March (1988)

[78] Placzek, G.; (1952), *Phys. Rev.*, **86**, p.377

[79] Quinn C.J., Dicknson J.E. and Beall G.H.; (1992) *Proceedings of the XVI International Congress on Glass* (Vol. 4), pp 79-84, Spanish Society of Ceramics and Glass

[80] Rajnak K.; (1965), *J. Chem. Phys.*, **43**(3), p. 847

[81] Ravaine, D. (1985), *Glass... Current Issues*, Wright A.F. and Dupuy, J. (Eds) Dordrecht: Martinus Nijhoff, pp 435

[82] Rawson, H.; (1967), *Inoraganic glass forming system*, Academic press, London

[83] Rawson H.; (1980 check) Glass Science and Technology, Properties and Applications of Glass (Vol. 3) Elsevier

[84] Sales B.C. and Boatner L.A.; (1984), *Science*, **226**, p. 45

[85] Sales B.C., Abraham M.M., Bates J.B. and Boatener L.A.; (1985), *J. Non-Cryst. Solids*, **71**, p. 103

[86] Sales B.C., Ramsey R.S., Bates J.B. and Boatner L.A.; (1986), *J. Non-Cryst. Solids*, **87**, p. 137

[87] Sammler R.L., Otaigbe J.U., Lapham, M.L., Bradley N.L., Monahan B.C. and Quinn C.J.; (1996), *J. Rheol.*, **40**, p.285

[88] Shafi N Abd El and S. Ibrahim; (1998), *Bull. Mater. Sci*, **21**(2), p. 167

[89] Shaw C.M. and Shelby J.E.; (1988), *J. Am. Ceram. Soc.*, **71**, p.252

[90] Sinclair R.N., Desa J.A.E. and Wright A.C.; (1983) *J. Am. Ceram. Soc*, **66**(1), p.72

[91] Smets B.M.J. and Lommen T.P.A.; (1981), *Phys. Chem. Glasses*, **2**, p.158

[92] Snitzer E.; (1961), *Phys. Rev. Lett.*, **7**, p.444

[93] Soper, A.K. and Egelstaff P.A.; (1980), *Nucl. Instrum. Meth*, p.415

[94] Stanworth, J.E.; (1946), *J. Soc. Glass Technol.*, **30** p.54-64 T

[95] Stanworth, J.E.; (1948 a), *J. Soc. Glass Technol.*, **32** p.154-172 T

[96] Stanworth, J.E.; (1948 b), *J. Soc. Glass Technol.*, **32** 366-372 T

[97] Stanworth, J.E.; (1952), *J. Soc. Glass Technol.*, **36** 217-241

[98] Sun, K.H.; (1947), *J. Am. Ceram. Soc.*, **30**, p.277

[99] Sun K. and Risen W.M.; (1988), *Solid St. Commun.*, **60**, 9, p 697

[100] Swenson J., Borjesson L. and Howells W.S.; (1995), *Phys. Rev. B*, **52** (13), p. 9310

[101] Takahashi K. (1962), *Advances in Glass Technology Part I*, p. 367, Plenum Press, New York

[102] Templeton D.H. and Dauben C. H.; (1954), *J. Am. Chem. Soc.*, **76**, p.5237

[103] Thijsse B. J.; (1984), *J. Appl. Cryst.*, **17**, p.61

[104] Thyagarajan K., Sooraj Hussain N., Annapurna K., Aruna V., Rajamohan Reddy K. and Buddhudu S.; (1997), *Phys. Chem. Glasses*, **38**(4), p.223

[105] Tick P.A.; (1984), *Phys. Chem. Glasses*, **25**, p.149

[106] Toratani H., Meissner H.E., Izumitani T. and Stokowski S.E.; (1987), *J. Non-Cryst. Solids*, **97/96**, p.701

[107] Turnbull D. and Cohen M.H.;(1958), *J. Chem. Phys.*, **29**, p.1049

[108] Turnbull D. and Cohen M.H.;(1960), *Modern Aspects of the Vitreous State*, Vol. 1, (Mackenzie J.D. ed.), p. 38 Butterworths, London.

[109] Turnbull D. and Cohen M.H.; (1961), *Nature*, **189**, p.131

[110] Van Wazer J.R.; (1958) *Phosphorus and its compounds*, Vol 1, Interscience, New York, p. 717

[111] Vaswani G.A. and Jahagirdar, P.B.; (1986), "Formation and Characterization of Borosilicate Glass for Immobilizing Highly Radioactive Waste", 14th International Congress on Glass.

[112] Vineyard G.H.; (1954), *Phys. Rev.*, **96**, p.93

[113] Wagner C.N.J.; (1978),*J. Non.cryst. Solids*, **31**, p.40

[114] Walter G., Kranold R., Stachel D. and Gotz W.; (1990), *Phys. Chem. Glasses*, **31**(5), p.188

[115] Warren B.E., Krutter H. and Morningstar O.; (1936), J. Am. Ceram. Soc., **19**, p.202

[116] Warren B.E.; (1941), *J. Am. Ceram. Soc.*, **24**, p.256

[117] Weber M.J. and Matsinger B.H.; (1972), *J. chem. Phys.*, **57**, p.562

[118] Weber M.J.; (1990), J. Non-Cryst. Solids, **123**, p.208

[119] Westman A.E.R.; (1960), *Modern aspects of the vitreous state* Vol. 1, Mackenzie J.D. (Ed.), Butterworth, London, p. 63

[120] Wright A.C.; (1974),*Advances in Stru. Res.*, p.1

[121] Wright A.C. and Leadbetter A.J.; (1976). *Phys. Chem. Glasses.* **17** (5). p.122

[122] Wright A.C. and Sinclair R.N.; (1978). *The Physics of* SiO_2 *and its Interfaces*, Ed. Pantilides S.T. (Pergammon, New York)

[123] Wright A.C., Etherington G., Erwin-Desa J.A. and Sinclair R. N.; (1982). *J. Phys. (Paris).* **43**, C-9, p.31.

[124] Wright A.C., Hannon A.C., Sinclair R.N., Johnson W.C. and Atzman M.; (1984) *J. Phys. F.* , **14**, L20

[125] Wright A.C., Hulme R.A., Grimley D.I., Sinclair R.N., Martin S.W., Price D.L. and Galeener F.L.; (1991), *J. Non-Cryst. Solids*, **129**, p. 213

[126] Yarnel J.L., Katz M.J., Wenzel R.G. and Koenig S.H.; (1973) *Phys. Rev.*, A7, p.2130

[127] Yasui I., Hasegawa H. and Imaoka M.; (1983), *Phys. Chem. Glasses* 24, p.65

[128] Yun Y.H. and Bray P.J.; (1978), *J. Non-Cryst. Solids*, **27**, p.363

[129] Zachariasen, W.H.; (1932), *J. Am. Ceram, Soc.* , **54**, p.3841

[130] Zernicke, F. and Prins, J.A.; (1927), *Zeit. of Physik*, **41**(2-3), p.184

Appendix A

Calculation of detector constant for the He^3 detector

The efficiency of the He^3 detector follows an exponential law;

$$\epsilon(k) = 1 - e^{ak/k_0}$$

where a is the detector constant.

a = number of He^3 atoms in the detector × absorption cross-section of He^3

= N × P × t × $\sigma_a(\lambda)$

where,

N = Avogadro number

P = Pressure in the detector = 3 bar of He^3 and 1.5 bar Krypton

t = Thickness = 5.1 cm

$\sigma_a(\lambda)$ = Absorption cross-section at wavelength λ

σ_a (0.783 Å) = 2322.43 barns

σ_a (1.27 Å) = 3766.91 barns

$$a(0.783) = \frac{6.023 \times 10^{23}}{22413} \times [3 \times 0.98692 \ \text{atm}] \times 5.1 \times 2322.43 \times 10^{-24} \text{cm} = 0.937$$

Similarly, $a(1.27$ Å$) = 1.53$

Appendix B

Parameters used in data analyses of Rare-earth Phosphate glasses

	La-P	La-Ce-P	La-Pr-P	La-Nd-P	Vanadium rod
σ_c (barns)	4.24	4.084	4.086	4.027	0.018
σ_{inc} (barns)	0.071	0.037	0.036	0.319	5.08
σ_T (barns)	4.57	4.268	4.415	5.332	7.31
A_w	27.181	25.606	27.563	27.327	50.942
μ cm^{-1}	0.278	0.271	0.29	0.387	0.527
δ	0.1031	0.0855	0.1074	0.1429	0.1537
ρ^0 (c.u./Å^3)	0.0609	0.0636	0.0657	0.0727	0.0722

Appendix C

Parameters used in data analyses of Nuclear Waste glasses

	WTR22	WTR62	WTR30	WTR35	WTR46
σ_c (barns)	4.305	4.25	4.272	4.296	3.511
σ_{inc} (barns)	0.251	0.304	0.276	0.25	0.2639
σ_T (barns)	34.391	33.725	32.172	30.777	47.2446
A_w	29.163	29.338	29.863	30.334	23.005
μ cm^{-1}	2.589	2.138	2.338	2.295	0.527
δ	0.5	0.5	0.5	0.5	—
ρ^0 (c.u./Å^3)	0.0753	0.0634	0.0727	0.0746	0.0722

Appendix D

Published Conference Presentations

1. 'Structure of Nuclear Waste Glasses', A.G. Shikerkar, G.R. Bhat. P.S.R. Krishna. J.A.E. Desa: (1994) Glass and Optical Materials Division, *94 Fall Meeting*, Ohio.

2. "Structures of Nuclear Waste and Borosilicate Glass by Neutron Diffraction", A.G. Shikerkar, G.R. Bhat, J.A.E. Desa, P.S.R. Krishna; (1995), *Solid State Physics* (India), **38 C**, p. 235

3. "Structures of Radioactive Waste Glasses", A.G. Shikerkar. J.A.E. Desa, G.R. Bhat and P.S.R. Krishna; (1997) *The Physics of Disordered Materials*, Proceedings of the International Conference. M.P. Saxena, N.S. Saxena, Deepika Bhandari ed(s), NISCOM. New Delhi, India. p.36

4. "Structural Investigation of Rare-Earth Phosphate Glasses by X-ray and Neutron Diffraction" A.G. Shikerkar. J.A.E. Desa. P.S.R. Krishna. R. Chitra, G.R. Bhat. (1998), *IUMRS - International Conference in Asia 98*, Bangalore. India.